Summer 8-15-2016

Green's Function Application for Pairing Correlations and the Optical Potential

Dong Ding
Washington University in St. Louis

WASHINGTON UNIVERSITY IN ST.LOUIS

Department of Physics

Dissertation Examination Committee:

Willem H. Dickhoff, Chairperson

Robert J. Charity

Kater W. Murch

Demetrios G. Sarantites

Lee G. Sobotka

Green's Function Application for Pairing Correlations and the Optical Potential

by

Dong Ding

A dissertation presented to the
Graduate School of Arts and Sciences
of Washington University in
partial fulfillment of the
requirements of the degree
of Doctor of Philosophy

August 2016

Saint Louis, Missouri

Contents

List of Figures

List of Tables

ABSTRACT OF THE DISSERTATION

Green's function application for pairing correlations and the optical potential

by

Dong Ding

Doctor of Philosophy in Physics

Washington University in St. Louis, August 2016

Professor Willem H. Dickhoff, Chairperson

Pairing in asymmetric nuclear matter has been studied incorporating the effect of finite total momentum. We employ the generalized Cooper eigenvalue equation, which can be used to demonstrate the pairing instability and also generates reasonable pairing gaps compared to the traditional Bardeen-Cooper-Schrieffer (BCS) gap equation. From phase space arguments and the resulting strength of the pairing gap, we learn that the Larkin-Ovchinnikov-Fulde-Ferrell phase with a finite total momentum is favored over the conventional phase in asymmetric nuclear matter, but not in symmetric nuclear matter. To address open questions in neutron star cooling, neutron matter pairing gaps of the ${}^1S_0$ and the ${}^3P_2 - {}^3F_2$ channels in a wide range of densities have been calculated using three different realistic interactions. Instead of the mean-field BCS procedure, we incorporate the influence of short- and long-range correlations in calculating the pairing gaps. Short-range correlations are treated to include the fragmentation of single-particle states, suppressing the gaps substantially. Long-range correlations dress the pairing interaction via density and spin modes, and provide a smaller correction. The results provide input for neutron-star cooling scenarios and are

parametrized in a user friendly way. The results are of particular relevance in view of the recent observational data on Cassiopeia A. To study the nucleon-nucleus scattering problem in an *ab-initio* way, the optical potential in the momentum vector basis beyond the mean-field has been calculated employing the $\mathcal{T} \times \rho$ folding as the first step of the self-consistent Green's function method. The deuteron pole structure of $\mathcal{T}-$ matrix has been properly avoided using the spectral functions from the dispersive optical model. A comparison of the resulting real and imaginary part of the self-energy at 100 MeV with the corresponding dispersive-optical-model potentials shows reasonable agreement.

Acknowledgments

I would first like to express my sincere gratitude to my advisor Prof. Wim Dickhoff for the continuous support and guidance for my Ph.D study and related research. I would like to thank him for the patience and for the opportunity to learn from his immense knowledge. His insightful physical intuition helped me during the time of research and writing of this thesis.

Besides my advisor, I would also like to thank the rest of my thesis committee: Prof. Lee Sobotka, Prof. Kater Murch, Prof. Robert Charity, and Prof. Demetrios Sarantites for their insightful comments and encouragement.

Thank you also to our collaborators from Europe, Arnau Rios and Artur Polls for the useful discussions, their knowledge, and important contributions they have made to the project.

Thanks to Helber Dussan for his contributions in developing the vector basis procedure, the $\mathcal{T}-$matrix code, and for numerous discussions about the rotational symmetry analysis and all the assistance with numerical procedures. Also thanks to Sam Witte for exploring the pairing code and his thesis for neutron star cooling. Additionally, thanks to Mack Atkinson for the help with clarifying some details of the DOM and calculations of the DOM spectral densities. I would also like to thank Hossein Mahzoon whose thesis has been the key model for the present one.

Special thanks go to my family for the support for my research from my mother and father and my life in general. Thanks also to my fiancée Hanxi Zhou for the years of waiting and encouragement, which has provided tremendous help.

I recognize support from the U.S. National Science Foundation under grants PHY-0968941 and PHY-1304242.

Chapter 1

Introduction

The many-body problem literally implies a problem that involves many items, many people, many molecules, many electrons or many nucleons, etc. More specifically for quantum physics, it involves a system composed of many indistinguishable particles and more importantly the interactions between the particles are not negligible. "In fact the many-body problem may be defined as the study of the effects of interaction between bodies on the behaviour of a many-body system."–Richard D. Mattuck, 1976 [1].

When we narrow down to the nuclear many-body problem, the systems that we are going to study are infinite nuclear/neutron matter and finite nuclei including many neutrons and protons but no electrons. It is worth mentioning that in the infinite nuclear matter case, the Coulomb interaction is ignored as its medium correlation has infinite length. Neutrons and protons are considered as point particles and the fundamental building blocks. It is certainly not a good approximation for someone who wants to study the bare interaction between them especially when the six valence quarks hidden inside are included in the description. We adopt existing models for the bare interaction like AV18 [2], CDBonn[3] and N3LO[4]. These interactions accurately describe nucleon-nucleon (NN) scattering data up to the pion

production threshold and the properties of the deuteron.

What kinds of collective phenomena may happen for nuclear two species systems? Looking into the history, a rather similar system for reference is the many-electron system in condensed matter physics. The experimental discovery of superconductivity more than one hundred years ago [5] was later theoretically understood to be the consequence of pairing of electrons by Bardeen–Cooper–Schrieffer (BCS) [6]. Medium effects from the positive ion background overcome the repulsive Coulomb interaction between a pair of electrons resulting in an effective attractive interaction and therefore the valence electrons can behave as bound pair states. The boson like pair can travel through the medium without friction. Another related phenomenon caused by boson-boson interactions is the superfluidity also discovered first in condensed matter physics for the Helium-4 liquid about 80 years ago [7]. Superfluidity due to the pairing of fermionic ^{3}He atoms was discovered in 1972 [8]. Thinking in terms of pairing phenomena, by increasing the pairing strength or diluting the system, Cooper pairs may undergo a phase transition known as Bose-Einstein condensation. This was first predicted by Bose and Einstein in 1920s for bosons [9] and later observed by experimentalists in 1995 [10]. This time the theorists had priority by 70 years. More ideas emerged as in the case that a Cooper pair carries a finite total momentum. The Larkin-Ovchinnikov [11]-Fulde-Ferrell [12](LOFF) phase is proposed around 1965 contrary to the usual assumption that pairs have zero total momentum. Note that a very similar phase exists in high-density quark-systems known as the CFL-phase [13].

Every phenomenon discussed above for condensed matter systems has its counterpart in some nuclear system [14, 15, 16, 17, 18, 19], especially because the bare nucleon-nucleon (NN) interaction has several attractive channels. Natural binding of one neutron and one proton leads to a stable deuteron. The idea of implementing the LOFF phase and Bose-Einstein condensation in nuclear physics represent relatively new topics[20, 16, 17, 18, 19]. However,

the underlying complicated scenario may be a good excuse for not discovering those phenomena for nuclear systems in the first place. Nuclear systems have two species of particles both involved in pairing with much more sophisticated bare interactions. The energy scale is so much higher that although the mean-field BCS theory already provides a good description for most cases of pairing in condensed matter physics, this is not the case for nuclear physics. Higher-order corrections are necessary both for nuclear matter and nuclei, for example due to short-range correlations (SRC) and long-range correlations (LRC) [21]. Nevertheless, simple pairing descriptions of open-shell systems are phenomenologically successful for like nucleons coupled to zero total angular momentum [22].

The strong suppression of the gap for the neutron-proton ${}^3S_1 - {}^3D_1$ partial wave channel in nuclei signals the necessity of going beyond mean-field BCS methods [14, 23]. Electron knock-out experiments also indicate that approximately 35% of the single-particle (sp) strength lies beyond the quasi-particle peaks [24, 25, 26]. SRC account for one third of this sp strength depletion by emptying the nuclear Fermi Sea and promote high momentum strength [27, 28, 29]. Another 20% of the sp fragmentation in the nuclei is induced by LRC via the coupling of sp states to low-lying resonances and collective modes [30]. For the pairing case in neutron matter, the presence of LRC mainly modify the effective interaction through density and spin collective modes [31]. The free NN forces between paired particles will therefore be modified by LRC. The overall influence on the pairing gap is screening or anti-screening depending on the pairing channel and the system under study like finite nuclei or infinite nuclear matter [32].

Another excuse for the nuclear physicist was the lack of a good experimental testing ground until neutron stars [33, 34] were discovered. The outer crust of the neutron star is composed of neutron-rich nuclei immersed in a degenerate electron fluid. At higher density, the neutrons condense to superfluid ${}^1S_0$ pairs and coexist with delocalized neutrons, electrons and nuclei

in the inner crust. The core regime where almost all the protons live has even higher density, and the neutrons may form a superfluid of condensed ${}^3P_2 - {}^3F_2$ pairs and the protons may become superconducting in the ${}^1S_0$ channel [35]. The observables for testing the description include the luminosity and therefore the effective temperature of the neutron star [36] and also pulsar glitching [33, 37, 38] associated with the abnormal behavior of the magnetic flux induced mainly by neutron superfluidity. The cooling curve of a neutron star can be filled gradually with more observations, while theoretical modeling the curves requires the knowledge of the pairing profile, not only the ${}^1S_0$ channel but also the ${}^3P_2 - {}^3F_2$ channel. The cooling of neutron stars is mainly a result of neutrino emission [39]. When the temperature is near the critical temperature for the associated superfluid, neutrinos emitted by pair breaking and formation (PBF) processes dominate the neutrino emissivities [40]. The rapid cooling of neutron stars at an early stage is ascribed to the neutron ${}^1S_0$ channel superfluid, and recently observations of rapid cooling in Cassiopeia A have been interpreted as evidence of the onset of pairing in the ${}^3P_2 - {}^3F_2$ channel [36]. Precise calculations of gap profiles based on solid nuclear physics input are important for pinning down the cooling curve and therefore a more precise neutron star description of pairing, in the sense that all the physics should be incorporated including SRC and LRC.

Exactly solving the many-body problem is not possible once the number of particles exceeds "two" as already proved by mathematicians [1]. Among these many formulations, the Green's function method using the propagator language was the most important tool in the formal development of many-body theory [30]. A fully dressed *sp* propagator contains all the information of the time evolution of *sp* states including medium effects. A very similar interpretation can be applied for two-particle (*tp*) propagators corresponding to *tp* states, which is the basis for understanding pairing. Think of a proton traveling through a neutron star, the exact information contains a combination of many time-dependent incidents of scattering or binding between the proton and the other particles connected by two- or more-

body interactions. The procedure should depend on the initial momentum of the proton and also the thermal state of the background. A mean-field treatment like the Hartree-Fock (HF) calculation considers the medium as an overall field without details of each incident's particular time dependence, therefore a certain amount of information is lost. Only higher order terms in the interaction can reveal more physics, like the infinite ladder diagrams that treat SRC induced by the repulsive hard-core nucleon-nucleon potential, and the bubble diagrams corresponding to LRC caused by the screening effects in the medium. Because of the complexity of treating higher-order diagrams, only in the last thirty years, the Green's function method has been applied to many-body problems as a calculational tool beyond its mean-field implementation [30].

Going beyond the mean-field for nucleon-nucleus scattering problem is also a necessity. The optical potential that describes elastic (and inelastic) *sp* properties of the nucleus can be constructed by two different approaches. One of the ways is the phenomenological approach that parameterizes the self-energy based on experimental data. The dispersive optical model (DOM) [41] starts from mean-field HF like interactions, incorporates higher-order physics by introducing an energy-dependent imaginary term and its dispersion correction for the real part. More physics can be included with more parameters, for example nonlocality, which has been proved to be important for the correct description of the charge density of ^{40}Ca [42]. The other way is a purely *ab-initio* calculation that starts from bare NN interactions, and builds the self-energy from the mapping of the Feynman-like diagrams [30]. A self-consistent calculation may then compensate for the inaccuracy of the initial inputs yielding a more precise description. In order to go beyond the mean-field approximation, the so-called $\mathcal{T} \times \rho$ method has been in the literature for decades [43, 44]. It incorporates higher-order ladder diagrams in the $\mathcal{T}-$matrix of free NN scattering which is energy dependent and has a deuteron pole originating from the natural binding of the proton and neutron. The density of the nucleus ρ is usually employed in the folding procedure to obtain the

optical potential. The existing $\mathcal{T} \times \rho$ method, however, treats the deuteron pole in a very artificial way for example by fixing the energy at the beam energy corresponding to NN scattering [43]. Considering the $\mathcal{T}-$matrix has a strong energy dependence, the deuteron pole should be treated more carefully or avoided all together. Also, a better description of the density beyond mean-field should generate more consistent results and the DOM density matrix can be a good candidate as a comparison between the DOM and the microscopic self-energy can be made to provide insight into the underlying physics.

The content of the thesis is arranged as follows. In chapter 2, we present the calculation of pairing gaps in asymmetric nuclear matter employing the generalized Cooper eigenvalue equation. The pairing instability is then discussed and reasonable pairing results are generated for the ${}^1S_0$ and ${}^3S_1 - {}^3D_1$ channels and compared to BCS calculations. The LOFF phase, with finite total momentum pairing, is favored over the conventional phase for asymmetric nuclear matter, as we conclude from phase space arguments and pairing gap results.

In chapter 3, we derive the BCS gap equation and discuss the way of solving this nonlinear equation. The gap profiles for nuclear matter are then generated for the comparison in chapter 2. To go beyond the mean-field BCS procedure, we discuss the importance of SRC and LRC and detail a way of incorporating these correlations in the calculation of the pairing gaps. SRC are treated to include the fragmentation of single-particle states, suppressing the gaps substantially. LRC dress the pairing interaction via density and spin modes, and provide a smaller correction. The gaps for neutron matter ${}^1S_0$ and ${}^3P_2 - {}^3F_2$ channels are generated, which provide input for neutron-star cooling scenarios.

In chapter 4, we explore the nucleon-nucleus scattering problem in an *ab-initio* way. The optical potential in the momentum vector basis beyond the mean-field has been calculated employing the $\mathcal{T} \times \rho$ folding as the first step of the self-consistent Green's function method. The deuteron pole structure of $\mathcal{T}-$ matrix has been properly avoided using the spectral

functions from the dispersive optical model. A comparison of the resulting real and imaginary part of the self-energy at 100 MeV with the corresponding dispersive-optical-model potentials shows reasonable agreement.

Finally, in chapter 5, conclusions and an outlook are presented for possible future improvement of the projects.

Chapter 2

Pairing with finite total momentum

2.1 Introduction

Pairing is an important feature of nuclear physics [35], relevant for the study of open-shell nuclei and neutron stars. It originates from the attractive components of the bare nucleon-nucleon interaction, trimmed significantly by short-range correlations (SRC) [21] and long-range correlations (LRC), and dominates the ingredients of neutron-star cooling [36] and pulsar glitching [33, 37, 38]. A similar but rather realistic playground for pairing is finite nuclei, where mean-field Bardeen–Cooper–Schrieffer (BCS) theory fails to explain the suppression of neutron-proton (np) pairing in heavy nuclei [14]. When the isospin-asymmetry is considered, which is induced by the weak interaction and commonly seen in stellar systems and exotic nuclei, isoscalar np pairing is disrupted because of the mismatch in the np Fermi surfaces [15]. Other applications emerge as Fermionic BCS superfluids undergo a transition to the Bose-Einstein condensate (BEC) state when the pairing strength increases or the system is diluted [17]. The BCS-BEC cross-over happens both for isospin asymmetric systems [17, 18, 19] and isospin symmetric system [45]. In the phase separation language, a

sequence of unconventional phases may emerge with increasing isospin asymmetry. For instance, the Larkin-Ovchinnikov [11]-Fulde-Ferrell [12](LOFF) phase where the Cooper pairs carry finite total momentum [17, 16] may occur.

To go beyond BCS theory, a more sophisticated treatment including SRC and LRC is presented in Chapter 3. In the current chapter, we seek a simpler way to study the effect of finite total momentum pairing in asymmetric nuclear matter. The content is arranged in the following way. The two-particle (tp) propagator and the corresponding Dyson equation is introduced. From this point, an eigenvalue equation is derived which contains the total-momentum and the isospin asymmetry factor as parameters. Solving the eigenvalue equation represents a generalization of the Cooper problem and reveals possibly the pairing instability. Employing the phase space argument, the influence of finite total momentum and isospin asymmetry on pairing is discussed.

2.2 Methods

The methods we use here are mainly adopted from the Ref. [21]. Some related details can be found in Chs. 9 and 15.

2.2.1 Two-particle propagator

In general, a 4-time two-particle (tp) propagator (see Eq.(2.1)) in different arrangements leads to N, $N \pm 1$, or $N \pm 2$ systems. In the case of pairing, a 2-time tp propagator tracks pairs of particles which are simultaneously added or removed from the ground state, connecting $N \pm 2$ systems in contrast to the single-particle (sp) propagator, which connects the ground

state with $N \pm 1$ systems. The corresponding 2-time tp propagator is given by

$$\begin{aligned} G_{pphh}(\alpha,\alpha';\beta,\beta';t_1-t_2) &\equiv \lim_{t_1'\to t_1}\lim_{t_2'\to t_2} G(\alpha t_1,\alpha' t_1',\beta t_2,\beta' t_2') \\ &= \lim_{t_1'\to t_1}\lim_{t_2'\to t_2} -\frac{i}{\hbar}\langle\Psi_0^N|\mathcal{T}[a_{\alpha' H}(t_1')a_{\alpha H}(t_1)a^\dagger_{\beta H}(t_2)a^\dagger_{\beta' H}(t_2')]|\Psi_0^N\rangle. \\ &= -\frac{i}{\hbar}\langle\Psi_0^N|\mathcal{T}[a_{\alpha' H}(t_1)a_{\alpha H}(t_1)a^\dagger_{\beta H}(t_2)a^\dagger_{\beta' H}(t_2)]|\Psi_0^N\rangle. \end{aligned} \tag{2.1}$$

The removal and addition operators are indicated by a_H and $a_H^\dagger$, and the subscript H refers to the Heisenberg picture. The time-ordering operation $\mathcal{T}$ controls particle-particle (pp) or hole-hole (hh) propagation. The state $|\Psi_0^N\rangle$ is the exact N-particle ground state. This full propagator is nearly impossible to calculate numerically incorporating all physics. Performing the perturbation expansion with infinite summations is required in the nuclear matter system in order to extract useful information. The standard procedure [21] is usually valid as in the sp case without the pairing instability as we are going to discuss in a later section. A common perturbation treatment is as follows. First, express the Heisenberg removal (addition) operators in terms of the interaction picture removal (addition) operators by using

$$a_{H\alpha}(t) = \hat{\mathcal{U}}(0,t)a_{I\alpha}(t)\hat{\mathcal{U}}(t,0), \tag{2.2}$$

which will introduce the time evolution operator $\hat{\mathcal{U}}(t_1,t_2)$. Secondly, insert the iterative expression of $\hat{\mathcal{U}}(t_1,t_2)$ as shown in Eq.(2.4). Last and most involved, apply Wick's theorem to remove disconnected configurations and replace $|\Psi_0^N\rangle$ by the noninteracting ground state $|\Phi_0^N\rangle$ with the lowest sp levels filled according to the Pauli principle, where $|\Psi_0^N\rangle =$

$\hat{\mathcal{U}}(0,\pm\infty)|\Phi_0^N\rangle$, resulting in (see Ref. [21])

$$\begin{aligned} G_{pphh}(\alpha,\alpha';\beta,\beta';t_1-t_2) = -\frac{i}{\hbar}\sum_{m=0}^{\infty}\left(\frac{-i}{\hbar}\right)^m \frac{1}{m!}\int dt_1\int dt_2 ... \int dt_m \\ \times \langle\Phi_0^N|\mathcal{T}[\hat{H}_1(t_1)\hat{H}_1(t_2)...\hat{H}_1(t_m)a_{\alpha'}(t_1)a_\alpha(t_1)a_\beta^\dagger(t_2)a_{\beta'}^\dagger(t_2)]|\Phi_0^N\rangle_{connected}, \end{aligned} \tag{2.3}$$

where $\hat{H}_1$ is the interaction picture Hamiltonian and the interaction picture labeling-I is omitted for the rest of the chapter. The time evolution operator in the interaction picture was used here

$$\hat{\mathcal{U}}(t,t_0) = \sum_{n=0}^{\infty}\left(\frac{-i}{\hbar}\right)^n \frac{1}{n!}\int_{t_0}^{t} dt_1\int_{t_0}^{t_1} dt_2 ... \int_{t_0}^{t_{n-1}} dt_n \mathcal{T}[\hat{H}_1(t_1)\hat{H}_1(t_2)...\hat{H}_1(t_n)]. \tag{2.4}$$

In zeroth order, one obtains the noninteracting *pphh* propagator in terms of *sp* propagators, which in the mean field approximation can be further simplified to diagonal *sp* propagators. Therefore, the noninteracting *pphh* propagator can be expressed as:

$$\begin{aligned} G_{pphh}^{(0)}(\alpha,\alpha';\beta,\beta';t_1-t_2) =& -\frac{i}{\hbar}\langle\Phi_0^N|\mathcal{T}[a_{\alpha'}(t_1)a_\alpha(t_1)a_\beta^\dagger(t_2)a_{\beta'}^\dagger(t_2)]|\Phi_0^N\rangle \\ =& i\hbar[G^{(0)}(\alpha,\beta;t_1-t_2)G^{(0)}(\alpha',\beta';t_1-t_2) \\ & - G^{(0)}(\alpha,\beta';t_1-t_2)G^{(0)}(\alpha',\beta;t_1-t_2)] \\ =& i\hbar[\delta_{\alpha,\beta}\delta_{\alpha',\beta'} - \delta_{\alpha,\beta'}\delta_{\alpha',\beta}]G^{(0)}(\alpha;t_1-t_2)G^{(0)}(\alpha';t_1-t_2), \end{aligned} \tag{2.5}$$

where the *sp* propagator reads:

$$G^{(0)}(\alpha,\beta;t_1-t_2) = -\frac{i}{\hbar}\langle\Phi_0^N|\mathcal{T}[a_\alpha(t_1)a_\beta^\dagger(t_2)]|\Phi_0^N\rangle, \tag{2.6}$$

which can easily be evaluated.

Performing the Fourier transform (FT) of Eq.(2.5) to the energy formulation yields:

$$G^{(0)}_{pphh}(\alpha,\alpha';\beta,\beta';E) = [\delta_{\alpha,\beta}\delta_{\alpha',\beta'} - \delta_{\alpha,\beta'}\delta_{\alpha',\beta}]\left\{\frac{\theta(\alpha-F)\theta(\alpha'-F)}{E-\epsilon_\alpha-\epsilon_{\alpha'}+i\eta} - \frac{\theta(F-\alpha)\theta(F-\alpha')}{E-\epsilon_\alpha-\epsilon_{\alpha'}-i\eta}\right\}, \tag{2.7}$$

where step functions θ limit states to above or below the Fermi energy indicated by F. An additional simplification is to drop the hh propagation based on phase space arguments, although it can be added back with ease.

In the first order terms, the contribution to G_{pphh} in the time formulation can be written as

$$\begin{aligned} G^{(1)}_{pphh}(\alpha,\alpha';\beta,\beta';t_1-t_2) &= \left(-\frac{i}{\hbar}\right)^2 \int dt \frac{1}{4}\sum_{\gamma\gamma'\delta\delta'}\langle\gamma\gamma'|V|\delta\delta'\rangle \\ &\times \langle\Phi_0^N|\mathcal{T}[a^\dagger_\gamma(t)a^\dagger_{\gamma'}(t)a_{\delta'}(t)a_\delta(t)a_{\alpha'}(t_1)a_\alpha(t_1)a^\dagger_\beta(t_2)a^\dagger_{\beta'}(t_2)]|\Phi_0^N\rangle \\ &\Rightarrow (i\hbar)^2\int dt \sum_{\gamma\gamma'\delta\delta'}\langle\gamma\gamma'|V|\delta\delta'\rangle \\ &\times G^{(0)}(\alpha,\gamma;t_1-t)G^{(0)}(\alpha',\gamma';t_1-t)G^{(0)}(\delta,\beta;t-t_2)G^{(0)}(\delta',\beta';t-t_2), \end{aligned} \tag{2.8}$$

leaving out self-energy insertions. The FT of the above equation generates the energy formulation of $G^{(1)}_{pphh}$ as follows:

$$G^{(1)}_{pphh}(\alpha,\alpha';\beta,\beta';E) = G^{(0)}_{pphh}(\alpha,\alpha';E)\frac{1}{2}\sum_{\gamma\gamma'}\langle\alpha\alpha'|V|\gamma\gamma'\rangle G^{(0)}_{pphh}(\gamma,\gamma';\beta,\beta';E). \tag{2.9}$$

In general, one can derive

$$G^{(n)}_{pphh}(\alpha,\alpha';\beta,\beta';E) = G^{(0)}_{pphh}(\alpha,\alpha';E)\frac{1}{2}\sum_{\gamma\gamma'}\langle\alpha\alpha'|V|\gamma\gamma'\rangle G^{(n-1)}_{pphh}(\gamma,\gamma';\beta,\beta';E). \tag{2.10}$$

Summing the iterative equation [2.10] to all order, it is possible to write down the corre-

sponding Dyson equation as follows:

$$G_{pp}(\alpha,\alpha';\beta,\beta';E) = G^{(0)}_{pp}(\alpha,\alpha';\beta,\beta';E) + G^{(0)}_{pp}(\alpha,\alpha';E)\frac{1}{2}\sum_{\gamma\gamma'}\langle\alpha\alpha'|V|\gamma\gamma'\rangle G_{pp}(\gamma,\gamma';\beta,\beta';E) \tag{2.11}$$

Considering the bound states of two particles, $G_{pphh}(\alpha,\alpha';\beta,\beta';E)$ takes the form of a Lehmann representation [46] by inserting a complete basis of the $N\pm 2$ systems. Both the bound states as well as the continuum states are included in the following expression

$$\begin{aligned} G_{pphh}(\alpha,\alpha';\beta,\beta';E) = &\sum_m \frac{\langle\Psi_0^N|a_{\alpha'}a_\alpha|\Psi_m^{N+2}\rangle\langle\Psi_m^{N+2}|a^\dagger_\beta a^\dagger_{\beta'}|\Psi_0^N\rangle}{E-(E_m^{N+2}-E_0^N)+i\eta} \\ &+\int_{\epsilon_T^+}^{\infty} d\hat{E}_\mu^{N+2}\frac{\langle\Psi_0^N|a_{\alpha'}a_\alpha|\Psi_\mu^{N+2}\rangle\langle\Psi_\mu^{N+2}|a^\dagger_\beta a^\dagger_{\beta'}|\Psi_0^N\rangle}{E-\hat{E}_\mu^{N+2}+i\eta} \\ &-\sum_n \frac{\langle\Psi_0^N|a^\dagger_\beta a^\dagger_{\beta'}|\Psi_n^{N-2}\rangle\langle\Psi_n^{N-2}|a_{\alpha'}a_\alpha|\Psi_0^N\rangle}{E-(E_0^N-E_n^{N-2})-i\eta} \\ &-\int_{-\infty}^{\epsilon_T^-} d\hat{E}_\nu^{N-2}\frac{\langle\Psi_0^N|a^\dagger_\beta a^\dagger_{\beta'}|\Psi_\nu^{N-2}\rangle\langle\Psi_\nu^{N-2}|a_{\alpha'}a_\alpha|\Psi_0^N\rangle}{E-\hat{E}_\nu^{N-2}-i\eta}, \end{aligned} \tag{2.12}$$

where the relative excitation energies are $\hat{E}_\mu^{N+2} = E_\mu^{N+2} - E_0^N$ and $\hat{E}_\nu^{N-2} = E_0^N - E_\nu^{N-2}$. In principle, the correlation amplitudes in the numerators and the energy denominators contain all the information of a particular system linked by pair addition to or removal from the ground state. In the case of pairing, we only need to know a portion of the amplitudes in the momentum representation related to the ground-state transitions to the $N\pm 2$ systems instead of calculating the full *tp* propagator.

2.2.2 Eigenvalue equation

In the limit of the free two-particle system, the noninteracting tp propagator as shown below

$$G^{(0)}_{pphh}(\alpha,\alpha';\beta,\beta';E) = [\delta_{\alpha,\beta}\delta_{\alpha',\beta'} - \delta_{\alpha,\beta'}\delta_{\alpha',\beta}] \left\{ \frac{\theta(\alpha-F)\theta(\alpha'-F)}{E-\epsilon_\alpha-\epsilon_{\alpha'}+i\eta} - \frac{\theta(F-\alpha)\theta(F-\alpha')}{E-\epsilon_\alpha-\epsilon_{\alpha'}-i\eta} \right\} \tag{2.13}$$

is further simplified to

$$G^{(0)}_{pp}(\alpha,\alpha';\beta,\beta';E) = [\delta_{\alpha,\beta}\delta_{\alpha',\beta'} - \delta_{\alpha,\beta'}\delta_{\alpha',\beta}] \left\{ \frac{1}{E-\epsilon_\alpha-\epsilon_{\alpha'}+i\eta} \right\}, \tag{2.14}$$

and the $N = 0$ states are therefore vacuum states. In the momentum representation, the $N = 2$ states depend on the total momentum $\boldsymbol{K}$, the relative momentum $\boldsymbol{k}$ and the intrinsic quantum numbers defined as follows:

$$\begin{aligned} \boldsymbol{K} &= \boldsymbol{k}_\alpha + \boldsymbol{k}_{\alpha'} = \boldsymbol{k}_\beta + \boldsymbol{k}_{\beta'}, \\ \boldsymbol{k} &= \frac{1}{2}(\boldsymbol{k}_\alpha - \boldsymbol{k}_{\alpha'}), \\ \boldsymbol{k}' &= \frac{1}{2}(\boldsymbol{k}_\beta - \boldsymbol{k}_{\beta'}). \end{aligned} \tag{2.15}$$

Explicitly, $|\Psi_0^{N=2}\rangle = |\boldsymbol{K}n\rangle$. With the chosen basis, the correlation amplitudes in the numerator of Eq.(2.12) can be written as

$$\langle 0|a_{\boldsymbol{k}_{\alpha'}m_{\alpha'}}a_{\boldsymbol{k}_\alpha m_\alpha}|\boldsymbol{K}n\rangle = \phi_n(\boldsymbol{K},\boldsymbol{k};m_\alpha m_{\alpha'}). \tag{2.16}$$

The noninteracting pp propagator in Eq.(2.11) reads

$$G_{pp}^{(0)}(\boldsymbol{K},\boldsymbol{k};E)=\frac{1}{E-\epsilon(\frac{1}{2}\boldsymbol{K}+\boldsymbol{k})-\epsilon(\frac{1}{2}\boldsymbol{K}-\boldsymbol{k})+i\eta}, \tag{2.17}$$

where the ϵ denotes single particle energy, while the E represents the total energy of the two particles. Now substitute the Lehmann representation of G_{pp}, namely the first two lines of Eq.(2.12), into the Dyson equation (2.11), taking the energy limit to a particular bound state on the left- and right-hand sides together with a weighting factor $lim_{E\to E_n}(E-E_n)$. The only term that survives must have a denominator $E-E_n$ and a corresponding numerator $\phi_n(\boldsymbol{K},\boldsymbol{k};m_\alpha,m_{\alpha'})$. With this procedure, the Dyson equation (2.11) transforms to an eigenvalue equation as follows:

$$\begin{aligned}&\left(\frac{\hbar^2\boldsymbol{K}^2}{4m}+\frac{\hbar^2\boldsymbol{k}^2}{m}\right)\phi_n(\boldsymbol{K},\boldsymbol{k};m_\alpha,m_{\alpha'})+\\&\frac{1}{2}\sum_{m_\gamma m_{\gamma'}}\int\frac{d^3q}{(2\pi)^3}\langle\boldsymbol{k}m_\alpha m_{\alpha'}|V(\boldsymbol{K})|\boldsymbol{q}m_\gamma m_{\gamma'}\rangle\phi_n(\boldsymbol{K},\boldsymbol{q};m_\gamma m_{\gamma'})=\tilde{E}_{n\boldsymbol{K}}\phi_n(\boldsymbol{K},\boldsymbol{k};m_\alpha,m_{\alpha'}),\end{aligned} \tag{2.18}$$

where the $\tilde{E}_{n\boldsymbol{K}}$ is the eigenvalue associated with the bound state. The relative momentum $\boldsymbol{q}$ reads

$$\boldsymbol{q}=\frac{1}{2}(\boldsymbol{k}_\gamma-\boldsymbol{k}_{\gamma'}). \tag{2.19}$$

The idea of getting rid of $\boldsymbol{K}$ is appropriate and valid for the case of two free particles. By inspecting Eq.(2.18), one may conclude that since the interaction V does not depend on $\boldsymbol{K}$, the effect of finite total momentum is shifting the energy $\tilde{E}_{n\boldsymbol{K}}$ by a constant amount $\frac{\hbar^2\boldsymbol{K}^2}{4m}$. We denote the energy of the possible bound state by E_n. Therefore, one can take $\boldsymbol{K}=0$ and solving the eigenvalue equation in the center-of-mass for the tp system. With

that simplification, the eigenvalue equation yields

$$\frac{\hbar^2 \boldsymbol{k}^2}{m}\phi_n(\boldsymbol{k}; m_\alpha, m_{\alpha'}) + \frac{1}{2}\sum_{m_\gamma m_{\gamma'}} \int \frac{d^3q}{(2\pi)^3}\langle \boldsymbol{k} m_\alpha m_{\alpha'}|V|\boldsymbol{q} m_\gamma m_{\gamma'}\rangle \phi_n(\boldsymbol{q}; m_\gamma m_{\gamma'}) \\ = E_n \phi_n(\boldsymbol{k}; m_\alpha, m_{\alpha'}). \tag{2.20}$$

2.2.3 Partial wave decomposition

Equation (2.20) in the vector $\boldsymbol{k}$ basis is solvable with brute force, which will be discussed at the end of the chapter. In general, if the interaction is a rotational invariant object, the total angular momentum will be a good quantum number. In the case of a two nucleon system, the total isospin can also be a good quantum number. The symmetry allows for projecting the vector basis to the partial wave basis. The *sp* momentum states can be expressed as

$$|\boldsymbol{k}\rangle = \sum_{LM_L} |kLM_L\rangle\langle LM_L|\hat{\boldsymbol{k}}\rangle = \sum_{LM_L} |kLM_L\rangle Y^*_{LM_L}(\hat{\boldsymbol{k}}), \tag{2.21}$$

where the spherical harmonic $Y^*_{LM_L}(\hat{\boldsymbol{k}})$ has the symmetry

$$Y^*_{LM_L}(-\hat{\boldsymbol{k}}) = (-1)^L Y^*_{LM_L}(\hat{\boldsymbol{k}}). \tag{2.22}$$

For two-particle *tp* states, the individual spin s and the isospin t couple to the total spin S and the total isospin T; then, the orbital momentum L and the total spin S couple to the

total angular momentum J as follows:

$$\begin{aligned}|\boldsymbol{k}_1 m_{s_1} m_{t_1}, \boldsymbol{k}_2 m_{s_2} m_{t_2}\rangle &= \frac{1}{\sqrt{2}} \sum_{SM_S TM_T LM_L} (\tfrac{1}{2} m_{s_1} \tfrac{1}{2} m_{s_2}|SM_S)(\tfrac{1}{2} m_{t_1} \tfrac{1}{2} m_{t_2}|TM_T) Y^*_{LM_L}(\hat{\boldsymbol{k}}) \\ &\times [1-(-1)^{L+S+T}]|\boldsymbol{K} k L M_L S M_S T M_T) \\ &= \frac{1}{\sqrt{2}} \sum_{SM_S TM_T LM_L JM_J} (\tfrac{1}{2} m_{s_1} \tfrac{1}{2} m_{s_2}|SM_S)(\tfrac{1}{2} m_{t_1} \tfrac{1}{2} m_{t_2}|TM_T) Y^*_{LM_L}(\hat{\boldsymbol{k}}) \\ &\times (LM_L SM_S|JM_J)[1-(-1)^{L+S+T}]|\boldsymbol{K} k L S J M_J T M_T).\end{aligned} \tag{2.23}$$

The Pauli principle is fulfilled by the factor $[1-(-1)^{L+S+T}]$, which indicates $L+S+T$ is locked to be odd for two-fermion systems. For example, ${}^1S_0$ and ${}^3S_1 - {}^3D_1$ for S-wave nucleon-nucleon channels.

2.2.4 Cooper problem and pairing instability

The above derivation generates a partial-wave basis version of Eq.(2.20) when propagation of mean-field particles above the Fermi energy in the medium characterized by a Fermi momentum k_F is considered:

$$\frac{\hbar^2 k^2}{m}\phi_n(kLSJT) + \frac{\theta(k-k_F)}{2}\sum_{L'}\int \frac{dqq^2}{(2\pi)^3}\langle kL|V^{JST}|qL'\rangle\phi_n(qL'SJT) = E_n\phi_n(kLSJT). \tag{2.24}$$

Numerically solving the above equation by matrix diagonalization yields a real discrete eigenvalue below twice the Fermi energy if the interaction is sufficiently attractive, which indicates a pp bound state below the continuum energy spectrum starting above twice the Fermi energy. The depth of this bound state depends on the strength of the attractive interaction. If we consider hh propagation only, the step function $\theta(k_F-k)$ in the second term of Eq.(2.26)

limits the phase space to inside the Fermi sphere. One obtains in that case

$$\frac{\hbar^2 k^2}{m}\phi_n(kLSJT) - \frac{\theta(k_F-k)}{2}\sum_{L'}\int\frac{dqq^2}{(2\pi)^3}\langle kL|V^{JST}|qL'\rangle\phi_n(qL'SJT) = E_n\phi_n(kLSJT). \tag{2.25}$$

Similarly and rather illustratively, a real discrete eigenvalue shows up above twice the Fermi energy if the interaction is sufficiently attractive, which indicates a hh bound state above the continuum energy spectrum starting from 2 times $\epsilon(k=0)$ to twice the Fermi energy. It is natural to ask what would happen when the eigenvalue equation is solved containing both pp and hh propagation. A short answer would be: a pairing instability will occur characterized by

$$\begin{aligned}\phi_n(kLSJT) = &\frac{\theta(k-k_F)}{2(E_n-\frac{\hbar^2k^2}{m})}\sum_{L'}\int\frac{dqq^2}{(2\pi)^3}\langle kL|V^{JST}|qL'\rangle\phi_n(qL'SJT)\\ &-\frac{\theta(k_F-k)}{2(E_n-\frac{\hbar^2k^2}{m})}\sum_{L'}\int\frac{dqq^2}{(2\pi)^3}\langle kL|V^{JST}|qL'\rangle\phi_n(qL'SJT).\end{aligned} \tag{2.26}$$

Mathematically, by examining the above equation, one concludes that the denominators $E_n - \frac{\hbar^2k^2}{m}$ will vanish for a particular k corresponding to E_n, and it is true for any value of E_n except for $E_n < 2\epsilon(0)$. This indicates that at least one pair of the eigenvalue solutions will be imaginary when the interaction is sufficiently attractive. To avoid the instability, one can manually modify the sp energy spectrum $\epsilon(k)$ by opening up a gap Δ at the Fermi surface. More precisely, a shift of the value Δ above Fermi surface is introduced as shown in Fig.(2.1).

We illustrate these points for the ${}^3S_1 - {}^3D_1$ channel in nuclear matter. The gap Δ for a specific density corresponding to $k_F = 0.45$ fm^{-1} is chosen to be the minimum value to avoid imaginary solutions. After the minimum gap Δ is introduced by shifting the kinetic energy by a value of Δ above the Fermi surface, the resulting bound-state eigenvalues of Eq.(2.26) are shown in Fig.(2.2). The two bound states behave corresponding to different densities when a sufficiently large gap is opened. Imagining moving the up-boundary namely the

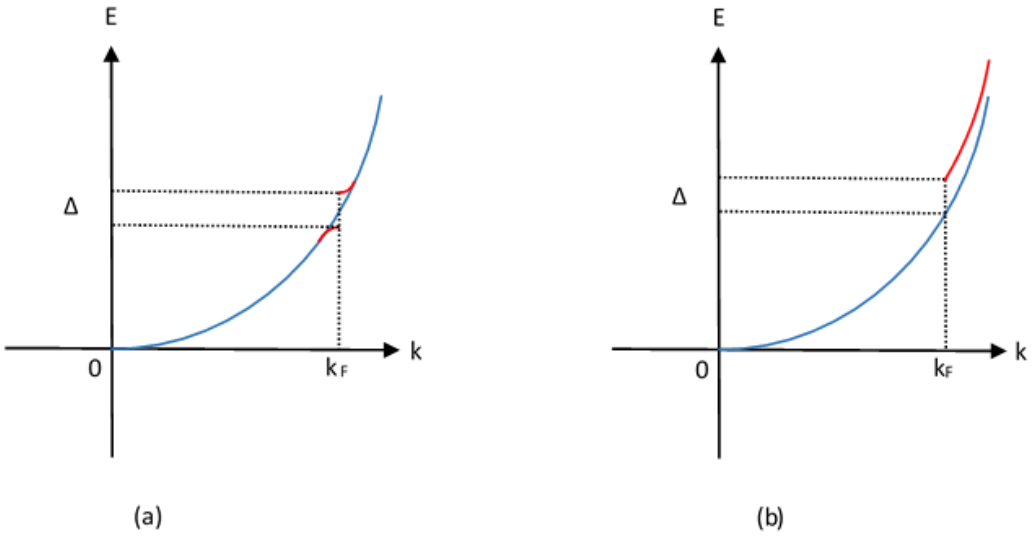

Figure 2.1: Illustration of how the introduction of a gap Δ modifies the single-particle spectrum. Left panel: for the case of BCS, a self-consistent mean-field treatment of the gap function Δ is obtained by solving the gap equation (see chapter 3 for details). Only a small region near Fermi surface is affected. Right panel: a constant shift above the Fermi surface can accomplish a qualitatively similar effect.

Fermi surface $+2\Delta$ up or down by varying the gap, the boundary where the eigenvalues split into two distinct pieces would also move right or left. For example: $\Delta = 10$ MeV would be recorded as the gap for $k_F = 0.45$ fm^{-1} because it is the minimum value when the eigenvalues will become real.

With the above methodology, a wide density range of gaps for $^1S_0$ and $^3S_1 - ^3D_1$ channels have been calculated using the Reid potential [47]. Comparing the results with the BCS calculation discussed in chapter 3. (see Fig.(2.3)) [48], the gaps are at most overestimated

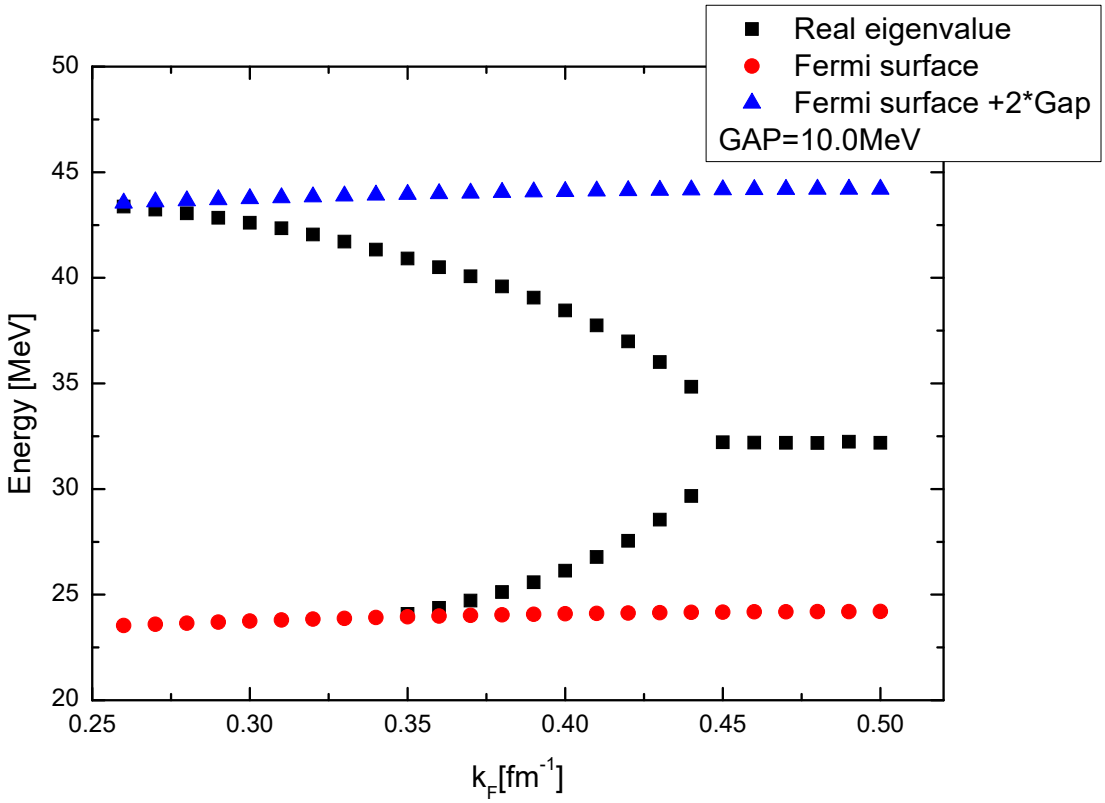

Figure 2.2: The Reid potential is used to calculate the eigenvalues for ${}^3S_1 - {}^3D_1$ channel. Only the real part of the eigenvalues are plotted. For $k_F > 0.45$ fm^{-1}, the two complex conjugated eigenvalues are overlapping with nonzero imaginary part.

by 10% and in some cases very close. This is understandable when it is realized that, to accommodate bound pair states determined by the gap itself, the BCS calculation modifies the energy spectrum only in a range near the Fermi surface while the method discussed here manually provides a shift of a constant Δ. There is even some advantage of the present method as it can reproduce the binding energy of the deuteron correctly in the low-density limit. Considering low-density neutrons and protons, where they can bind to deuterons, the BCS formalism still considers them as being part of a Fermi sea.

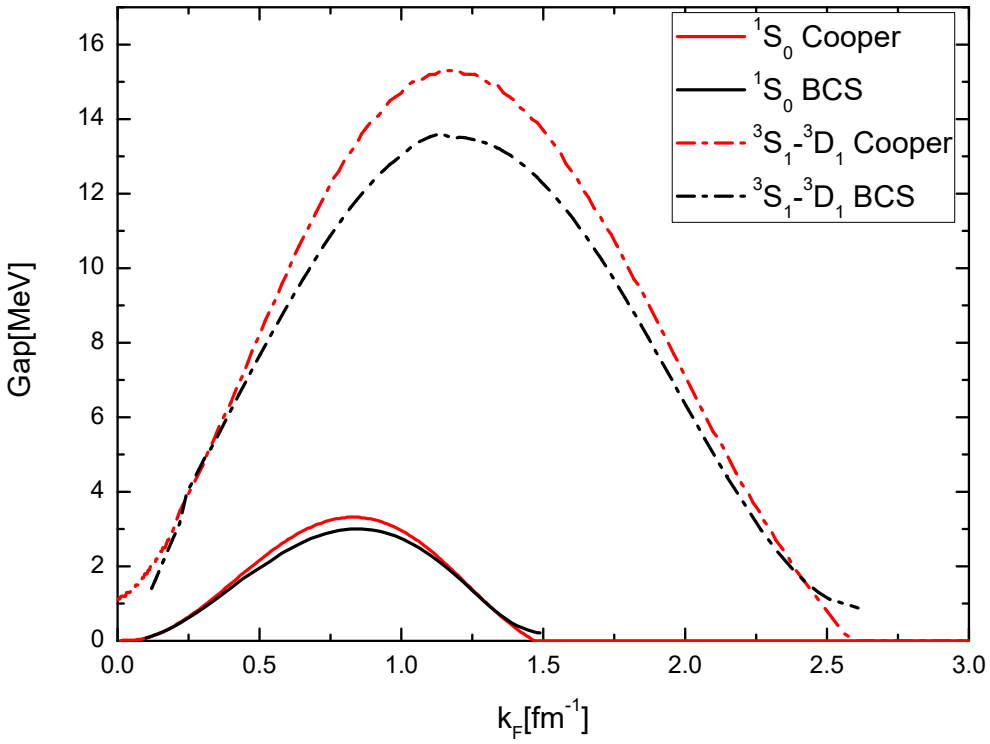

Figure 2.3: The Reid potential is used to calculate ${}^1S_0$ and ${}^3S_1 - {}^3D_1$ gaps with the BCS and the Cooper eigenvalue method including a minimum gap at the Fermi surface to avoid complex eigenvalues.

2.2.5 The total momentum $K \neq 0$ pairing and asymmetric nuclear matter

For symmetric nuclear matter or neutron matter it is appropriate, based on phase space arguments, to focus on the $\boldsymbol{K} = 0$ case for two free particles. Once hh propagation is included, the nonzero total momentum case should be considered. The total momentum $\boldsymbol{K}$ enters the Eq.(2.26) in two places. In the first case, it involves $\epsilon(\frac{1}{2}\boldsymbol{K} + \boldsymbol{k})$ and $\epsilon(\frac{1}{2}\boldsymbol{K} - \boldsymbol{k})$, which can be neglected for the same reason as mentioned before. In the other case the

step function should be modified as $\theta(|\frac{1}{2}\boldsymbol{K}+\boldsymbol{k}|-k_F)\theta(|\frac{1}{2}\boldsymbol{K}-\boldsymbol{k}|-k_F)$ for pp part and $\theta(k_F-|\frac{1}{2}\boldsymbol{K}+\boldsymbol{k}|)\theta(k_F-|\frac{1}{2}\boldsymbol{K}-\boldsymbol{k}|)$ for hh part. For simplification, since then a partial-wave basis can be employed, the angle-average Pauli operators can be introduced

$$\begin{aligned}\bar{Q}_{pp}(K,q)&=\frac{1}{2}\int_{-1}^{1}Q_{pp}(\boldsymbol{K},\boldsymbol{q})\mathrm{d}cos\theta_q,\\ \bar{Q}_{hh}(K,q)&=\frac{1}{2}\int_{-1}^{1}Q_{hh}(\boldsymbol{K},\boldsymbol{q})\mathrm{d}cos\theta_q,\end{aligned}\tag{2.27}$$

where

$$\begin{aligned}Q_{pp}(\boldsymbol{K},\boldsymbol{q})&=\theta(|\frac{1}{2}\boldsymbol{K}+\boldsymbol{k}|-k_F)\theta(|\frac{1}{2}\boldsymbol{K}-\boldsymbol{k}|-k_F)\\ Q_{hh}(\boldsymbol{K},\boldsymbol{q})&=\theta(k_F-|\frac{1}{2}\boldsymbol{K}+\boldsymbol{k}|)\theta(k_F-|\frac{1}{2}\boldsymbol{K}-\boldsymbol{k}|).\end{aligned}\tag{2.28}$$

The angle between $\boldsymbol{K}$ and $\boldsymbol{q}$ is denoted by θ_q. These Pauli operators for a nonzero total momentum will reduce the phase space and therefore reduce the binding of two particles. Numerical calculations to illustrate this feature are shown in Fig.(2.4). As expected, a finite total momentum reduces pairing dramatically for both the ${}^1S_0$ channel and for the ${}^3S_1-{}^3D_1$ channel [49]. Physically, if two particles participate in the same Fermi sea, only the fraction of them near the Fermi surface would be likely to interact with each other and therefore create possible bound states. However, a finite total momentum pair requires, when one of them is on the Fermi surface that the other one is far removed from the Fermi surface (and vice versa), which will certainly suppress the number of particles involved in pairing, in a similar way as in an asymmetric system which will be discussed in the following section.

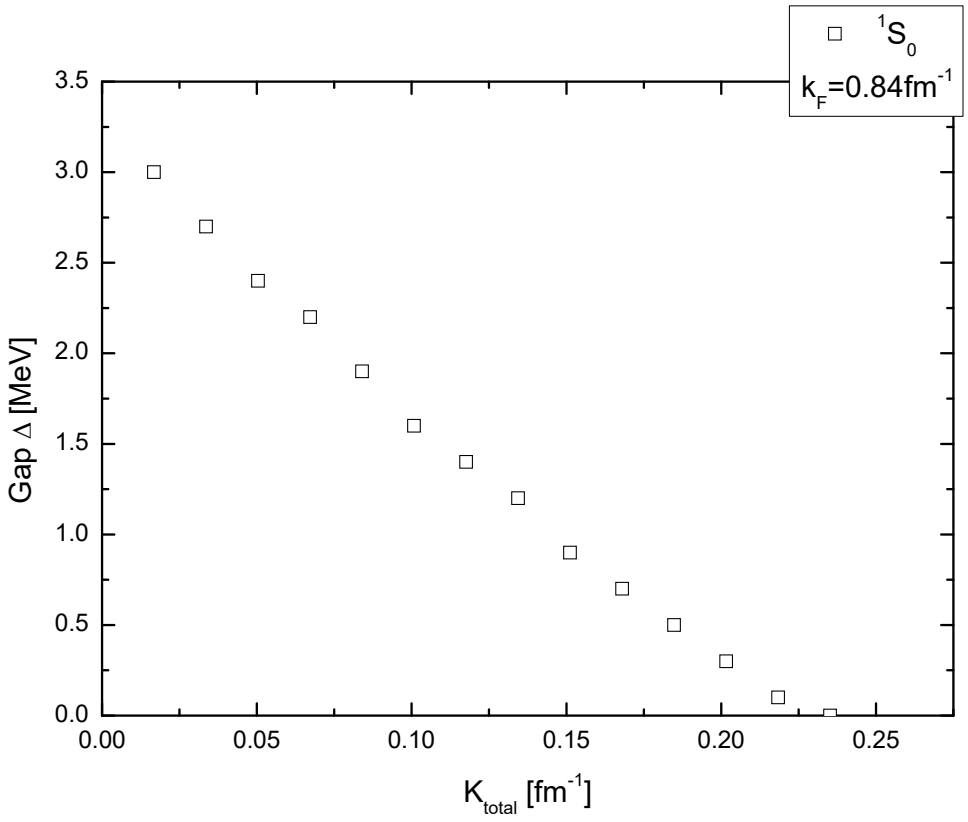

Figure 2.4: The $^1S_0$ channel gaps are calculated at density $k_F = 0.84$ fm^{-1} with increasing total momentum $\boldsymbol{K}$.

The present model can accommodate one additional parameter–the asymmetry parameter. In a two-species system relevant for a neutron star, the neutrons are far more dense than the protons, indicated by a larger Fermi momentum as they are both contained in the same volume. The asymmetry parameter α is defined as

$$\alpha = \frac{\rho_N - \rho_P}{\rho_N + \rho_P}, \tag{2.29}$$

which determines the Fermi momenta of the neutrons and the protons once a particular particle number density is chosen. The interacting phase space for protons and neutrons in

the asymmetric case is controlled by the Pauli operator

$$Q_{pp}^{As} = \theta(|\frac{1}{2}\boldsymbol{K} + \boldsymbol{k}| - k_F^N)\theta(|\frac{1}{2}\boldsymbol{K} - \boldsymbol{k}| - k_F^P). \tag{2.30}$$

It represents less phase space compared to the symmetric case where the total momentum $\boldsymbol{K} = 0$ and the density are fixed. Detailed calculations of the asymmetric Pauli operator are illustrated in table(A.1) of the appendix. The physical picture is the same as the case when the total momentum is nonzero and the system is symmetric. When a particle from one Fermi sea interacts with another one from a different Fermi sea, and their total momentum is set to be zero, they can not both be on their Fermi surface. The influence on the gap Δ therefore is expected to reduce the binding. Note that in the asymmetric system, the Pauli operator is no longer a monotonic function of total momentum $\boldsymbol{K}$, as the phase space is maximized when $K = k_F^N - k_F^P$. This means that a nonzero total momentum actually increases the binding for a fixed asymmetry factor α. This is illustrated in Fig.(2.5), for asymmetric nuclear matter at a density corresponding to $k_F = 0.76$ fm^{-1}. A realistic play ground for the high density np matter is in the crust of a neutron star, where protons consistent only $5 - 10\%$ of the whole baryonic matter, roughly corresponding to an asymmetric factor $\alpha = 0.8 - 0.9$. The large asymmetry results in a relatively small population of the protons therefore a superfluid in the np sector is much less likely compared to the nn sector. Considering the strong np pairing gap, it is still possibly a necessary piece in the physics of neutron-star cooling [39].

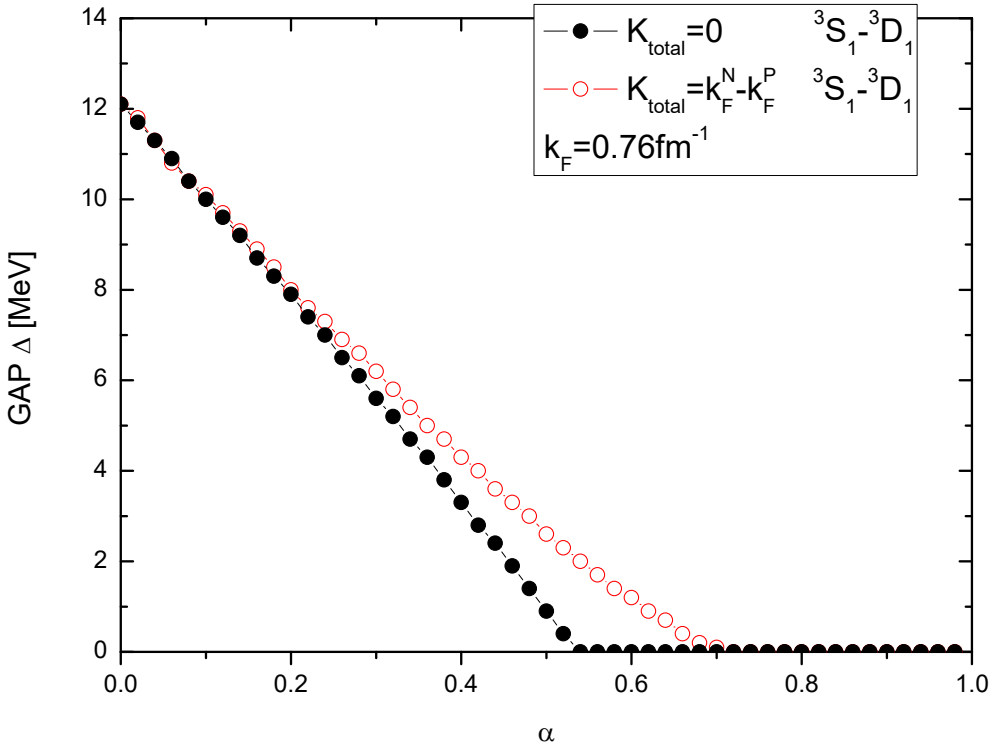

Figure 2.5: The ${}^3S_1 - {}^3D_1$ channel is calculated at density $k_F = 0.76$ fm^{-1} using the Reid potential corresponding to α from 0 to 1. Black circles: $K = 0$; Red circles: $K = k_F^n - k_F^p$.

Additional densities with $k_F = 0.25 - 1.64$ fm^{-1} are calculated in the same way as for Fig.(2.5). The results are put together in Fig.(2.6). When $\alpha = 0$, which also means the optimum $K = k_F^N - k_F^P = 0$, the gap values are the same for $K = 0$ and $K = k_F^N - k_F^P$ for each density. With increasing α, the finite total momentum increases and overall the gaps are reduced. However, the $K = k_F^N - k_F^P$ gaps are always above the $K = 0$ gaps. In the low density regime where $k_F < 0.76$ fm^{-1}, the tail of the gaps extended to the range $\alpha > 0.7$ where neutron stars can exist [35, 36].

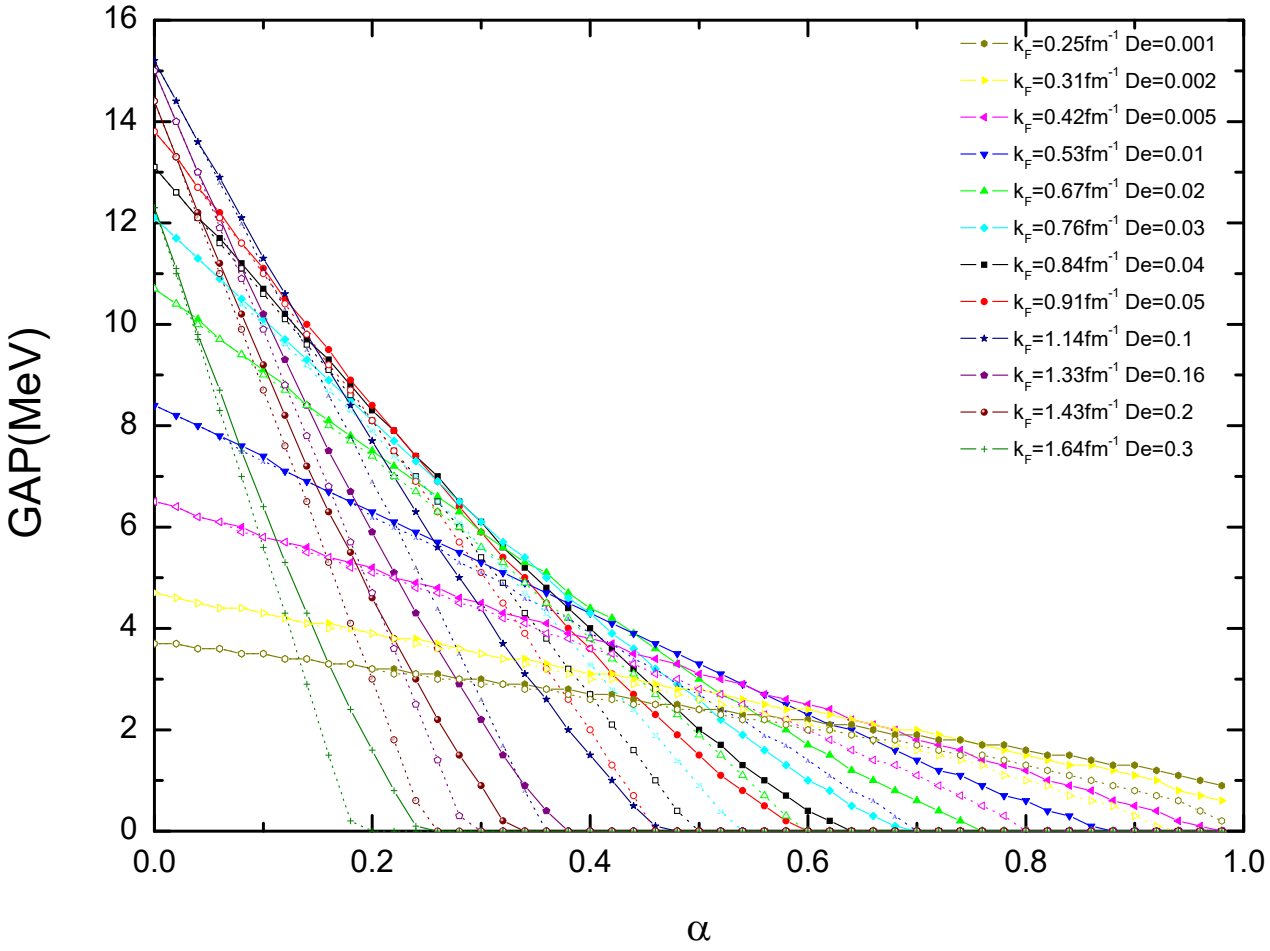

Figure 2.6: Similar to Fig(2.5), the ${}^3S_1 - {}^3D_1$ channel is calculated using the CD-Bonn potential corresponding to α from 0 to 1. The figure contains a lot more densities as indicated by different colors. Dotted line: $K = 0$; solid line: $K = k_F^N - k_F^P$.

2.3 Results and discussion

The method discussed here is rather simple and preliminary compared to the one in Ref. [17] although only small densities are considered there, but it provides insights into the influence on the pairing by the finite total momentum and the asymmetry of the system. In principle,

a systematic treatment of pairing requires thermodynamics under the BCS formalism, as discussed in Ref. [15], where finite temperature gaps are calculated for asymmetric nuclear matter. The phase competition and separation between the unpaired phase, the BCS phase, the BEC phase and the LOFF phase are also controlled by thermodynamics [17, 19, 45]. In order to generate realistic pairing gaps, one should extend the BCS formalism to include the finite total momentum $\boldsymbol{K}$, the isospin asymmetry factor α and the temperature T dependence. Some of these issues are further explored in chapter 3. We conclude that an optimized finite total momentum will enhance pairing for the asymmetric system, although a finite total momentum or asymmetry alone will both suppress pairing. As mentioned before, in neutron stars, protons consistent only $5-10\%$ of the whole baryonic matter in the crust region. The percentage could be even smaller in the core region [39]. This translates to an asymmetric factor $\alpha = 0.8 - 0.9$. Our calculation indicates a surviving pairing gap if an optimized total momentum is chosen. However, correlations like SRC may completely destroy the np sector pairing [50], so we will discuss their treatment in the next chapter.

Chapter 3

Pairing in high-density neutron matter including SRC and LRC

3.1 Introduction

The cooling scenario of a neutron star requires the presence of superfluid pairs in the crust and also in the core region [51, 52]. Especially when the temperature is near the critical temperature for the associated superfluid, neutrinos emitted by pair breaking and formation (PBF) processes dominate the whole neutrino emissivities [40]. Furthermore, the modeling of pulsar glitches also requires the presence of superfluids in the crusts of neutron stars [33, 37, 38]. The moment of inertia of a neutron star is mainly stored in the superfluid vortices which are not free to move [53, 54, 55]. When the solid crust drags the more rapidly rotating interior component, a sudden brake may occur causing the glitch in the observed rotation rate [53]. Therefore, when and where the superfluity is present provides a key for understanding the internal properties of neutron stars or more generally dense matter. More astrophysical observations will certainly consolidate models and the equation of state for high-density

nuclear matter. A good example is the observation of the fast cooling neutron star Cassiopeia A, which has been studied as providing evidence of ${}^3P_2 - {}^3F_2$ channel pairing [36]. Nuclear physicists can provide information on the pairing profile for dense matter by consistent many-body calculations of the pairing gaps employing constraints from the theoretical and experimental knowledge of finite nuclei.

Our systematic treatment of pairing gaps (Δ) starts from the well-known Bardeen–Cooper–Schrieffer (BCS) method, in the sense that the single particle (*sp*) energy spectrum is systematically updated compared to the previous chapter where a constant shift is employed. It works best for weakly correlated systems but requires modification in the case of correlated nuclear systems [21]. The strong suppression of the gap for the neutron-proton (*np*) ${}^3S_1 - {}^3D_1$ channel in nuclei signals the necessity of going beyond mean-field BCS methods [14, 23]. Electron knock-out experiments also indicate that approximately 35% of the *sp* strength lies beyond the quasi-particle peaks [24, 25, 26]. Short-range correlations (SRC) account for one third of this *sp* strength depletion by emptying the nuclear Fermi Sea and promote high momentum strength [27, 28, 29]. An approach employing Z-factors within the BCS scheme has been used to evaluate the influence of SRC for pairing [32, 56]. A universal suppression of pairing gaps has been concluded. However, Z-factors only take into account the *sp* strength reduction on the Fermi surface, while pairing is active in a momentum region close to but not only on the Fermi surface. Detailed information that describes the location of the *sp* strength like the spectral functions is therefore preferred for pairing calculations. To avoid the instability induced by pairing, an above-critical temperature $\mathcal{T}$-matrix resummation is introduced in the construction of the spectral functions [50].

Another 20% of the *sp* fragmentation in the nuclei is induced by long-range-correlations (LRC) via the coupling of *sp* states to low-lying resonances and collective modes [30]. For the pairing case in neutron matter, the presence of LRC mainly modify the effective interaction

through density and spin collective modes. The free NN forces between paired particles will therefore be dressed by LRC. The overall influence on the pairing gap may be different for finite nuclei and infinite nuclear matter [32]. In this chapter, we will concentrate on the effect of LRC on pairing for infinite neutron matter, with the help from a semi-phenomenological implementation of Fermi liquid theory (FLT) [57].

The content of the chapter is arranged as follows. By introducing the Gorkov-equations, the famous BCS gap equation is casually derived in the first section. A typical example of numerical results is presented to illustrate pairing effects for finite temperature. Then we discuss the SRC influence in the next section by a careful treatment of the spectral functions from the $\mathcal{T}$-matrix resummation method which is only valid above the critical temperature. An appropriate extrapolation method is then introduced to generate zero-temperature spectral functions. A comparison with the Z-factor method is discussed. The LRC are included following the proposal of Ref. [31] by an infinite sum of the particle-hole (ph) excitation diagrams. Landau parameters are used to represent the Fermi-liquid properties. The results are presented in the last section.

3.2 BCS method

3.2.1 Condensed ground state

We recall from last chapter that the normal perturbation expansion for identical fermions failed to converge when the Cooper instability occurs, or in other words when the inter-particle interaction is sufficiently attractive. The true ground state no longer represents a noninteracting ground state but a superfluid state with condensed pairs. In order to proceed with a perturbation calculation, the starting point should therefore be modified to include

a superfluid solution. The BCS Hamiltonian, symmetric under time reversal, contains a pairing part [21]:

$$\hat{H} = \hat{H}_0 + \hat{V} = \sum_{\alpha>0} \epsilon_\alpha (a^\dagger_\alpha a_\alpha + a^\dagger_{\bar{\alpha}} a_{\bar{\alpha}}) - g B^\dagger B, \tag{3.1}$$

where $(\alpha, \bar{\alpha})$ are time-reversed states, if momentum space is considered, it means $k_1 = -k_2$ and therefore total momentum zero is assumed in the beginning. We note that extra modification should take place when finite total momentum is a relevant consideration. The $\sum_{\alpha>0}$ refers to a summation over one member of each pair. The pair creation operator $B^\dagger = \sum_{\alpha>0} x_\alpha a^\dagger_\alpha a^\dagger_\alpha$ with normalization condition $\sum_{\alpha>0} |x_\alpha|^2 = 1$ is added. For $\hat{V} = 0$ the *sp* Hamiltonian $\hat{H}_0$ characterize the noninteracting ground state

$$|F\rangle = \prod_{h=1}^{N/2} a^\dagger_h a^\dagger_{\bar{h}} |0\rangle, \tag{3.2}$$

where the orbitals with lowest ϵ are filled. For $\hat{V} < 0$, the total energy for a state $|\Psi^N\rangle$ has a negative contribution, proportional to the occupation of the pair state $B^\dagger$. The balance between the *sp* state and the pair state is no longer controlled by particle number conservation rather by the grand-canonical potential $\hat{\Omega} = \hat{H} - \mu \hat{N}$ in Fock space. The conclusion is then that the Fermi sea $|F\rangle$ is a poor starting point of the perturbation expansion.

3.2.2 The normal and anomalous propagator

With the BCS Hamiltonian or a realistic nuclear Hamiltonian, we introduce the normal *sp* propagator as follows

$$i\hbar G_{11}(\boldsymbol{p}m; t - t') = \langle \Psi_0 | \mathcal{T}[a_{\boldsymbol{p}m_\Omega}(t) a^\dagger_{\boldsymbol{p}m_\Omega}(t')] | \Psi_0 \rangle. \tag{3.3}$$

The counterpart of it reads

$$i\hbar G_{22}(\boldsymbol{p}m;t-t') = \langle\Psi_0|\mathcal{T}[a^\dagger_{-\boldsymbol{p}-m_\Omega}(t)a_{-\boldsymbol{p}-m_\Omega}(t')]|\Psi_0\rangle, \tag{3.4}$$

where $a_{\boldsymbol{p}m_\Omega} = e^{\frac{i}{\hbar}\hat{\Omega}t}a_{\boldsymbol{p}m}e^{-\frac{i}{\hbar}\hat{\Omega}t}$ are in the Heisenberg picture, with $\hat{\Omega} = \hat{H} - \mu\hat{N}$ defining the time evolution. They describe *sp* excitations in the case when the ground state $|\Psi_0\rangle$ is derived from the usual Fermi sea $|F\rangle$. The ground state $|\Psi_0\rangle$ here is much more complicated. It minimizes $\Omega_0 = \langle\Psi_0|\hat{H} - \mu\hat{N}|\Psi_0\rangle$ under the constraint $N = \langle\Psi_0|\hat{N}|\Psi_0\rangle$ and presents a superposition of the $N \pm 2$, $N \pm 4$,... pair states [21]. Consequently, the anomalous propagators defined below are no longer vanishing quantities but must be included according to

$$i\hbar G_{12}(\boldsymbol{p}m;t-t') = \langle\Psi_0|\mathcal{T}[a_{\boldsymbol{p}m_\Omega}(t)a_{-\boldsymbol{p}-m_\Omega}(t')]|\Psi_0\rangle, \tag{3.5}$$

and its counterpart

$$i\hbar G_{21}(\boldsymbol{p}m;t-t') = \langle\Psi_0|\mathcal{T}[a^\dagger_{-\boldsymbol{p}-m_\Omega}(t)a^\dagger_{\boldsymbol{p}m_\Omega}(t')]|\Psi_0\rangle. \tag{3.6}$$

These propagators contain the information of pair states. The usual Fourier Transformation generates the energy representation of the propagators as follows:

$$\begin{aligned}
G_{11}(\boldsymbol{p}m;E) &= \langle\Psi_0|a_{\boldsymbol{p}m}\tfrac{1}{E-\hat{\Omega}+\Omega_0+i\eta}a^\dagger_{\boldsymbol{p}m} + a^\dagger_{\boldsymbol{p}m}\tfrac{1}{E+\hat{\Omega}-\Omega_0-i\eta}a_{\boldsymbol{p}m}|\Psi_0\rangle \\
G_{12}(\boldsymbol{p}m;E) &= \langle\Psi_0|a_{\boldsymbol{p}m}\tfrac{1}{E-\hat{\Omega}+\Omega_0+i\eta}a_{-\boldsymbol{p}-m} + a_{-\boldsymbol{p}-m}\tfrac{1}{E+\hat{\Omega}-\Omega_0-i\eta}a_{\boldsymbol{p}m}|\Psi_0\rangle \\
G_{21}(\boldsymbol{p}m;E) &= \langle\Psi_0|a^\dagger_{-\boldsymbol{p}-m}\tfrac{1}{E-\hat{\Omega}+\Omega_0+i\eta}a^\dagger_{\boldsymbol{p}m} + a^\dagger_{\boldsymbol{p}m}\tfrac{1}{E+\hat{\Omega}-\Omega_0-i\eta}a^\dagger_{-\boldsymbol{p}-m}|\Psi_0\rangle \\
G_{22}(\boldsymbol{p}m;E) &= \langle\Psi_0|a^\dagger_{-\boldsymbol{p}-m}\tfrac{1}{E-\hat{\Omega}+\Omega_0+i\eta}a_{-\boldsymbol{p}-m} + a_{-\boldsymbol{p}-m}\tfrac{1}{E+\hat{\Omega}-\Omega_0-i\eta}a^\dagger_{-\boldsymbol{p}-m}|\Psi_0\rangle
\end{aligned} \tag{3.7}$$

where $\Omega_0 = \langle\Psi_0|\hat{H}-\mu\hat{N}|\Psi_0\rangle$ indicates the minimized energy. Similarly, they fulfill Dyson-like equations named Gorkov equations:

$$\begin{aligned} G_{11}(\boldsymbol{p}m;E) =& G_{11}^{(0)}(\boldsymbol{p}m;E) + G_{11}^{(0)}(\boldsymbol{p}m;E)\Sigma_{11}(\boldsymbol{p}m;E)G_{11}(\boldsymbol{p}m;E) \\ &+ G_{11}^{(0)}(\boldsymbol{p}m;E)\Sigma_{12}(\boldsymbol{p}m;E)G_{21}(\boldsymbol{p}m;E), \\ G_{21}(\boldsymbol{p}m;E) =& G_{22}^{(0)}(\boldsymbol{p}m;E)\Sigma_{21}(\boldsymbol{p}m;E)G_{11}(\boldsymbol{p}m;E) \\ &+ G_{22}^{(0)}(\boldsymbol{p}m;E)\Sigma_{22}(\boldsymbol{p}m;E)G_{21}(\boldsymbol{p}m;E), \end{aligned} \tag{3.8}$$

where the noninteracting normal propagators are given by

$$\begin{aligned} G_{11}^{(0)}(\boldsymbol{p}m;E) &= \frac{\theta(\epsilon_{p\mu})}{E-(\epsilon_{p\mu})+i\eta} + \frac{\theta(-\epsilon_{p\mu})}{E-(\epsilon_{p\mu})-i\eta}, \\ G_{22}^{(0)}(\boldsymbol{p}m;E) &= \frac{\theta(\epsilon_{p\mu})}{E+(\epsilon_{p\mu})+i\eta} + \frac{\theta(-\epsilon_{p\mu})}{E+(\epsilon_{p\mu})-i\eta}. \end{aligned} \tag{3.9}$$

With $\epsilon_{p\mu} = p^2/2m - \mu$. The $\Sigma_{11}(\boldsymbol{p}m;E)$ and $\Sigma_{22}(\boldsymbol{p}m;E)$ terms represent the normal self-energy, while the $\Sigma_{12}(\boldsymbol{p}m;E)$ and the $\Sigma_{21}(\boldsymbol{p}m;E)$ represent the anomalous self-energy. The diagrams representing the first-order anomalous self-energy are shown in Fig.(3.1). Without giving the detailed diagram rules (see Ref. [21]), we write down the expressions for the first order self-energy, which will also be relevant when SRC are introduced:

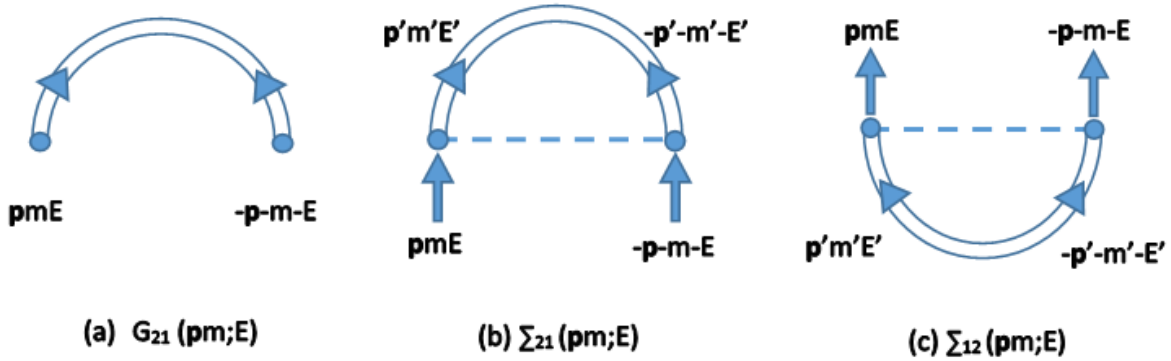

Figure 3.1: Diagrams illustrate (a) the anomalous propagator $G_{21}(\boldsymbol{p}m;E)$, (b) the first-order anomalous self-energy $\Sigma_{21}(\boldsymbol{p}m;E)$, and (c) the first-order anomalous self-energy $\Sigma_{12}(\boldsymbol{p}m;E)$.

$$\Sigma_{21}(\boldsymbol{p}m;E) = (-1)\frac{i}{2\pi}\sum_{\boldsymbol{p}'}\int dE' V(\boldsymbol{p}-\boldsymbol{p}')e^{i\eta E'}G_{21}(\boldsymbol{p}'m;E'),$$
$$\Sigma_{12}(\boldsymbol{p}m;E) = (-1)\frac{i}{2\pi}\sum_{\boldsymbol{p}'}\int dE' V(\boldsymbol{p}-\boldsymbol{p}')e^{i\eta E'}G_{12}(\boldsymbol{p}'m;E'). \tag{3.10}$$

At this stage we employ a schematic interaction represented by V which for neutron matter could lead to ${}^1S_0$ pairing. A more detailed form is given when $P-$wave pairing is considered subsequently.

3.2.3 BCS gap equation

In order to derive the gap equation, we reshuffle the Gorkov equations (3.8) by introducing G_{11}^N and G_{22}^N, which fulfill the following Dyson equation ([21, 50, 58, 59])

$$G_{11}^N(\boldsymbol{p}m;E) = G_{11}^{(0)}(\boldsymbol{p}m;E) + G_{11}^{(0)}(\boldsymbol{p}m;E)\Sigma_{11}(\boldsymbol{p}m;E)G_{11}^N(\boldsymbol{p}m;E),$$
$$G_{22}^N(\boldsymbol{p}m;E) = G_{22}^{(0)}(\boldsymbol{p}m;E) + G_{22}^{(0)}(\boldsymbol{p}m;E)\Sigma_{22}(\boldsymbol{p}m;E)G_{22}^N(\boldsymbol{p}m;E). \tag{3.11}$$

The G_{11}^N and G_{22}^N are the usual normal propagators. They only connect *sp* states influenced by the normal self-energy. The resulting new Gorkov equations now look like [21, 58]

$$G_{11}(\boldsymbol{p}m;E) = G_{11}^N(\boldsymbol{p}m;E) + G_{11}^N(\boldsymbol{p}m;E)\Sigma_{12}(\boldsymbol{p}m;E)G_{21}(\boldsymbol{p}m;E),$$
$$G_{21}(\boldsymbol{p}m;E) = G_{22}^N(\boldsymbol{p}m;E)\Sigma_{21}(\boldsymbol{p}m;E)G_{11}(\boldsymbol{p}m;E). \tag{3.12}$$

Below the critical temperature, the Gorkov formalism couples the full superfluid *sp* propagator G_{11} to its normal component via an anomalous self-energy. The superfluid propagator G_{11} connects not only *sp* states but also allow *sp* excitation from condensed pair states, while the anomalous propagator G_{21} connects only the paired states. Substituting the second line

of Eq.(3.12) into the first-order anomalous self-energy (Eq.(3.10)), we have

$$\begin{aligned}\Sigma_{21}(\boldsymbol{p}m;E) &= (-1)\frac{i}{2\pi}\sum_{\boldsymbol{p}'}\int dE' V(\boldsymbol{p}-\boldsymbol{p}')e^{i\eta E'}G_{21}(\boldsymbol{p}'m;E') \\ &= (-1)\frac{i}{2\pi}\sum_{\boldsymbol{p}'}\int dE' V(\boldsymbol{p}-\boldsymbol{p}')e^{i\eta E'}G^N_{22}(\boldsymbol{p}'m;E')\Sigma_{21}(\boldsymbol{p}'m;E')G_{11}(\boldsymbol{p}'m;E').\end{aligned} \tag{3.13}$$

For lowest order BCS theory, the self-energies are energy independent terms represented as follows

$$\begin{aligned}\Sigma_{11}(\boldsymbol{p}m) &= -\Sigma_{22}(\boldsymbol{p}m) = V_p, \\ \Sigma_{21}(\boldsymbol{p}m) &= \Sigma_{12}(\boldsymbol{p}m) = \Delta_p s_m.\end{aligned} \tag{3.14}$$

Now we introduce a generalized energy denominator to take the place of the two propagators convolution in Eq.(3.13) as shown below:

$$-\frac{1}{2E_p} \equiv -\frac{i}{2\pi}\int dE' e^{i\eta E'}G^N_{22}(\boldsymbol{p}m;E')G_{11}(\boldsymbol{p}m;E'). \tag{3.15}$$

Consequently the BCS gap equation is established, but already written in the partial-wave basis to anticipate applications for neutron matter.

$$\Delta^{JST}_\ell(p) = -\sum_{\ell'}\int_0^\infty \frac{dkk^2}{(2\pi)^3}\langle p|V^{JST}_{\ell\ell'}|k\rangle_A \frac{1}{2E_k}\Delta^{JST}_{\ell'}(k), \tag{3.16}$$

where the subscript A means the interaction is anti-symmetrized. The partial-wave channels could be coupled ($\ell = \ell' \pm 2$) or uncoupled ($\ell = \ell'$) depending on the interaction. The energy spectrum is modified by the gap function $\overline{\Delta}(k)$ as

$$E^2(k) = \chi^2(k) + \overline{\Delta}^2(k). \tag{3.17}$$

In lowest-order, the χ function represents the free *sp* energy spectrum:

$$\chi(k) = \frac{k^2}{2m} - \mu, \tag{3.18}$$

where μ denotes the chemical potential of the system. For an uncoupled channel,

$$\overline{\Delta}(k) = \Delta_\ell^{JST}(k), \tag{3.19}$$

whereas, for the coupled channel case, the averaged gap function $\overline{\Delta}(k)$ is taken to be the mean square root of the gaps for each channel

$$\overline{\Delta}(k) = \sqrt{[\Delta_\ell^{JST}(k)]^2 + [\Delta_{\ell'}^{JST}(k)]^2} \tag{3.20}$$

to avoid dealing with coupling of different angular momentum projections. Applying the relevant formalism at finite temperature involves Matsubara sums (see chapter 24 of the Ref. [21]). We omit the derivation but introduce the temperature dependent gap equation,

$$\Delta_\ell^{JST}(p) = -\sum_{\ell'} \int_0^\infty \frac{\mathrm{d}k k^2}{(2\pi)^3} \langle p|V_{\ell\ell'}^{JST}|k\rangle_A \frac{1}{2E_k} \Delta_{\ell'}^{JST}(k) \tanh(\frac{\beta E_{p'}}{2}), \tag{3.21}$$

and the corresponding energy denominator as follows

$$-\frac{1}{2E_p} \equiv \frac{1}{\beta} \sum_n e^{i\eta\omega_n} G_{22}^N(\boldsymbol{p}m;\omega_n) G_{11}(\boldsymbol{p}m;\omega_n), \tag{3.22}$$

with the corresponding spectral representation of the normal and superfluid propagator reads

$$\begin{aligned} G_{22}^N(\boldsymbol{p}m;\omega_n) &= \int_{-\infty}^{+\infty} \frac{d\omega}{2\pi} \frac{A^N(p;\omega)}{i\omega_n + \omega}, \\ G_{11}(\boldsymbol{p}m;\omega_n) &= \int_{-\infty}^{+\infty} \frac{d\omega}{2\pi} \frac{A^s(p;\omega)}{i\omega_n - \omega}, \end{aligned} \tag{3.23}$$

where the so-called Matsubara energies are

$$\omega_n = \frac{(2n+1)\pi}{\beta}. \tag{3.24}$$

In the mean-field approximation, the energy dependence of the normal spectral function A^N is a delta peak at χ_p, while for the superfluid spectral function A^s, it has a two-delta-peak structure with different weights as indicated in the following equations

$$\begin{aligned} A^N(p;\omega) &= 2\pi\delta(\omega-\chi_p), \\ A^s(p;\omega) &= \left(\frac{E_p+\chi_p}{2E_p}2\pi\delta(\omega-E_p)+\frac{E_p-\chi_p}{2E_p}2\pi\delta(\omega+E_p)\right). \end{aligned} \tag{3.25}$$

With the above preparation, the energy denominator shown in Eq.(3.22) can be evaluated as

$$\begin{aligned} -\frac{1}{2E_p} &\equiv \frac{1}{\beta}\sum_n e^{i\eta\omega_n}G^N_{22}(\boldsymbol{p}m;\omega_n)G_{11}(\boldsymbol{p}m;\omega_n) \\ &= \frac{1}{\beta}\sum_n e^{i\eta\omega_n}\int_{-\infty}^{+\infty}\frac{d\omega}{2\pi}\frac{A^N(p;\omega)}{i\omega_n+\omega}\int_{-\infty}^{+\infty}\frac{d\omega'}{2\pi}\frac{A^s(p;\omega')}{i\omega_n-\omega'} \\ &= \int_{-\infty}^{+\infty}\frac{d\omega}{2\pi}\int_{-\infty}^{+\infty}\frac{d\omega'}{2\pi}A^N(p;\omega)A^s(p;\omega')\frac{1-f(\omega)-f(\omega')}{-\omega-\omega'}, \end{aligned} \tag{3.26}$$

where the $f(\omega)$ is the Fermi-Dirac distribution reads

$$f(\omega) = \frac{1}{1+exp(\frac{\omega-\mu}{T})}. \tag{3.27}$$

Inserting the mean-field spectral functions as indicated by Eq.(3.25) and taking the temperature $T=0$, the left-hand side of Eq.(3.26) will reproduce the result of Eq.(3.17). Beyond mean-field spectral functions will deviate from delta functions significantly, and the complex physics included therein will be discussed in the SRC section.

3.2.4 Solving the gap equation for temperature $T = 0$

The nonlinear gap equation (3.16) can be solved with self-consistent matrix multiplication. A trial function $\Delta(k) = Constant$ can be introduced in the beginning and updated to convergent results as shown in Fig.(3.2), where the bare NN force AV18 [2] is used in the calculation at the density $\rho = 0.36$ fm^{-3} for the partial wave coupled $^3P_2 - ^3F_2$ channel for pure neutron matter. The momentum dependence of the gap function is smooth. Note that it can be negative for a certain momentum range as shown for the coupled channel, the negative part of the red dashed curve after $k_F = 4.0$ fm^{-1} is flipped by taking the absolute value. Once the averaging formula Eq.(3.20) is taken into account, only the magnitude of the gap function will affect the effective energy spectrum and only the value at the Fermi momentum k_F is recorded for the corresponding density.

How the effective energy spectrum behaves including pairing correlations is shown in Fig.(3.3) and Fig.(3.4). We observe that only a small range (on the order of $\Delta = 0.64$ MeV) around Fermi surface is affected by the gap function. This also supports the notion that the BCS superfluidity is a phenomenon limited to a region near the Fermi surface. The magnitude of the gap Δ measures the energy it takes to break a pair and create a *sp* excitation.

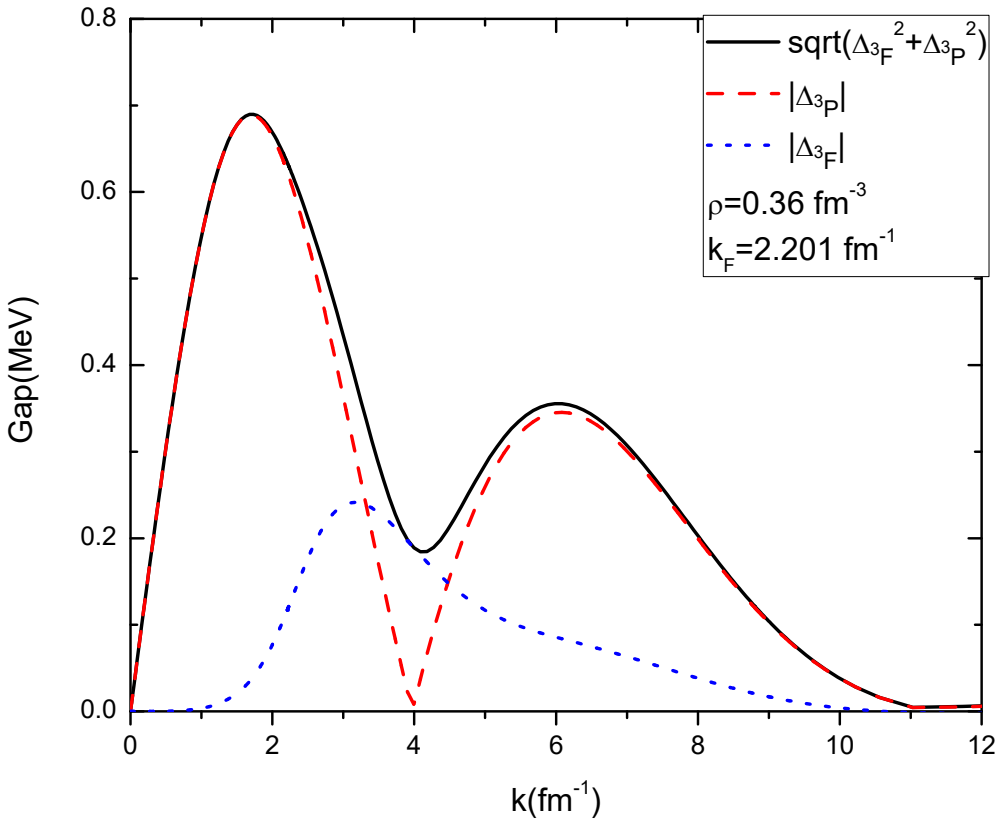

Figure 3.2: The coupled channel ${}^3P_2 - {}^3F_2$ gap function at the density $\rho = 0.36$ fm^{-3} has been calculated using the bare NN interaction AV18. The solid black curve represents the averaged gap function $\overline{\Delta}(k)$, the dashed red line represents the $\Delta_{^3P}$ and the dotted blue line represents the $\Delta_{^3F}$. The gap value $\Delta = 0.64$ MeV at the Fermi momentum $k_F = 2.201$ fm^{-1} will be recorded to represent the averaged gap for $\rho = 0.36$ fm^{-3}.

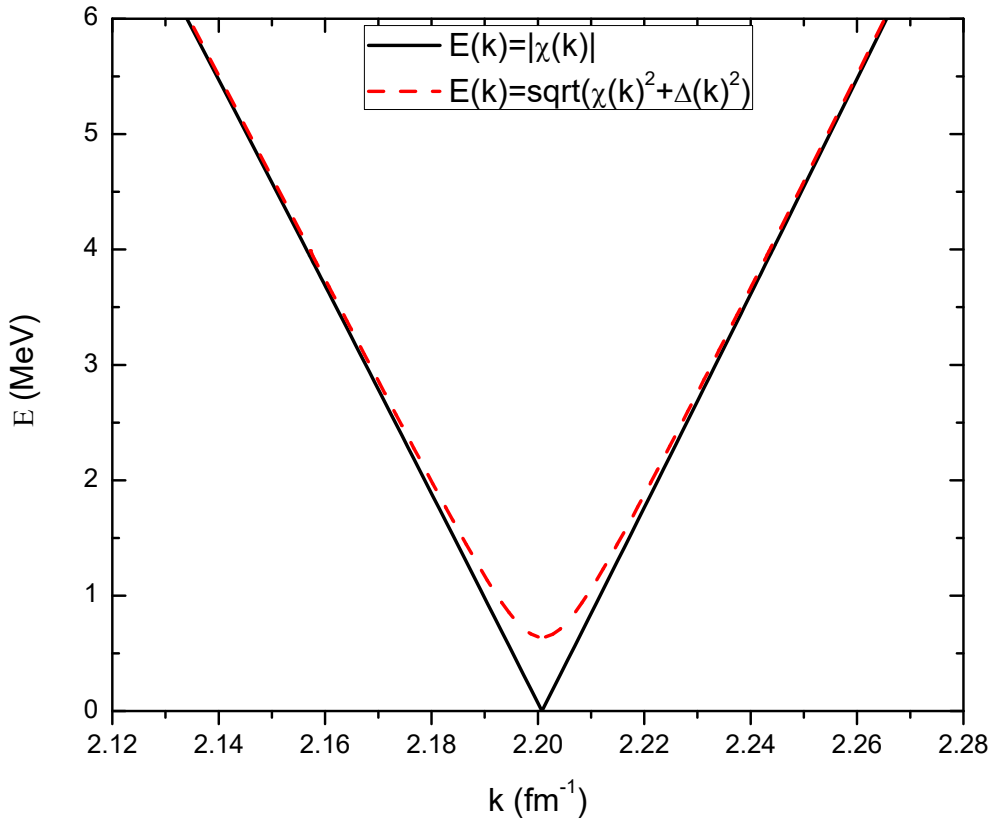

Figure 3.3: The effective energy spectrum as a function of momentum k is calculated for the coupled channel ${}^3P_2 - {}^3F_2$ at density $\rho = 0.36$ fm^{-3} using the bare NN interaction AV18. The solid black curve represents the free energy spectrum $\chi(k) = \epsilon(k) - \mu$, while the dashed red line represents the modified energy spectrum.

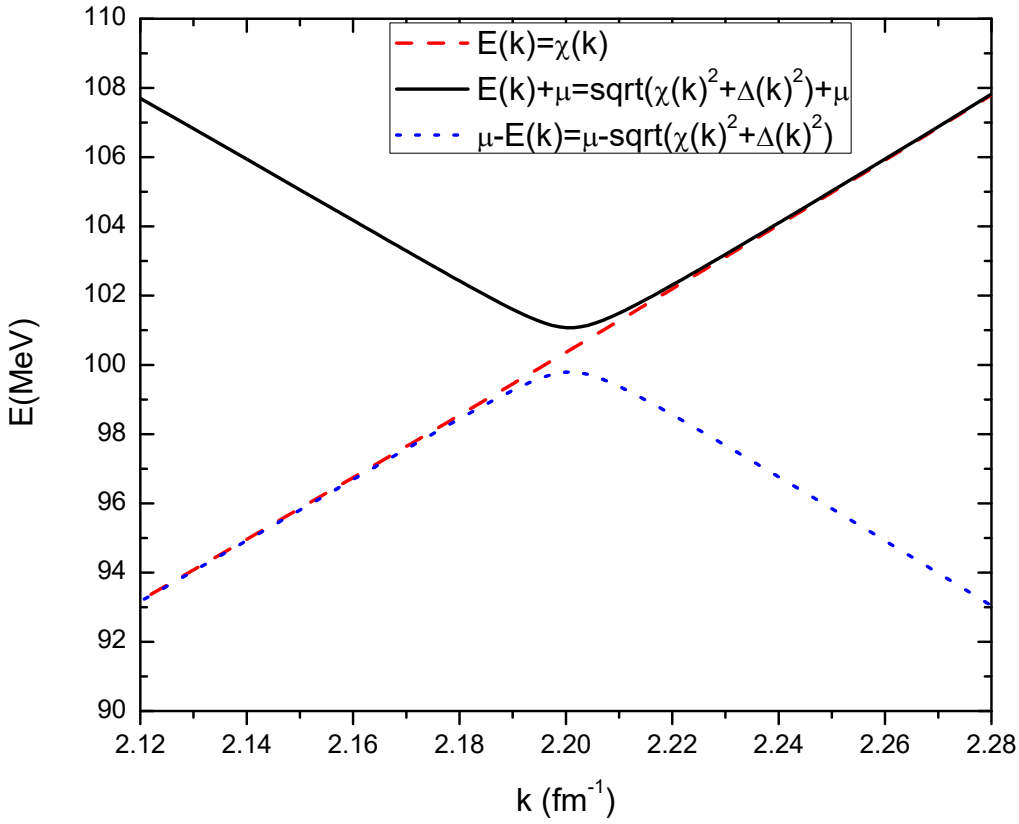

Figure 3.4: The same data sets are used as Fig.(3.3), but plotted differently to give a quantitative sense on how the gap modifies the spectrum compare to the strategy we used in the previous chapter, where a constant shift is introduced.

A full density dependence is calculated using AV18 including the uncoupled ${}^1S_0$ channel and the coupled ${}^3P_2 - {}^3F_2$ channel for isospin $T_I = 1$, the coupled ${}^3S_1 - {}^3D_1$ channel for isospin $T_I = 0$. The results are shown in Fig.(3.5). We note that pairing profiles for different channels are very unique in the lowest order BCS calculation. In the low density region, relevant for neutron matter superfluids in the crust of the neutron star, the ${}^1S_0$ channel has a gap of the order of 3 MeV, while in the high density region, the ${}^3P_2 - {}^3F_2$ channel has a gap in the order of 0.6 MeV also relevant for neutron matter superfluids in the neutron star

crust and also the core region. The ${}^3S_1 - {}^3D_1$ channel has the widest density dependence and a very large gap in the order of 12 MeV, relevant for symmetric nuclear matter and nuclei. It does not cover the free deuteron binding energy at low density and also does not disappear quickly at high density. Nevertheless, all the gaps will be significantly modified and suppressed by SRC especially for the np channel ${}^3S_1 - {}^3D_1$ as already studied in Ref. [50]. We will revisit the profiles when SRC and LRC are incorporated.

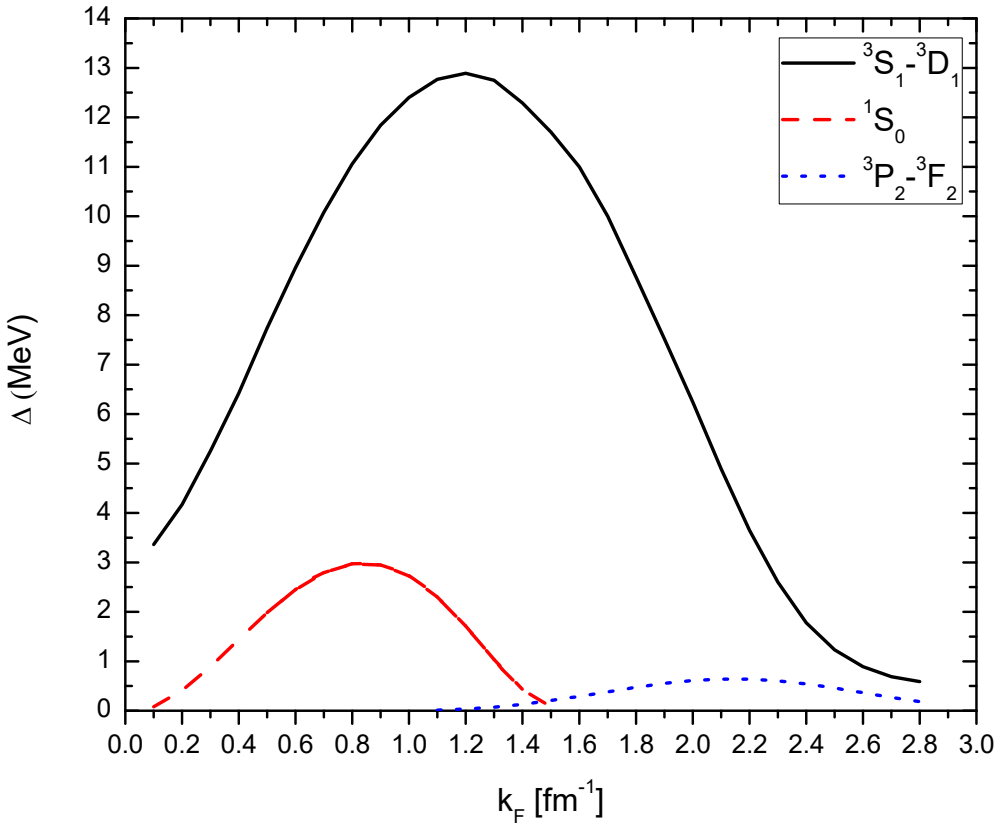

Figure 3.5: A full density dependence of the gaps calculated using the AV18 in the lowest order BCS approach. The solid black curve represents the isospin $T_I = 0$ coupled channel ${}^3S_1 - {}^3D_1$. The dashed red curve represents the isospin $T_I = 1$ uncoupled channel ${}^1S_0$. The dotted blue curve represents the isospin $T_I = 1$ coupled channel ${}^3P_2 - {}^3F_2$.

3.2.5 Solving the gap equation for temperature $T \neq 0$

A similar numerical method is used to solve the gap given in Eq.(3.21). The temperature dependence of the coupled channel ${}^3P_2 - {}^3F_2$ gap at the density $\rho = 0.36$ fm^{-3} is calculated using AV18 as shown in Fig.(3.6). As expected, with the temperature increasing, the gap reduces rapidly as the pairs are melted. The critical temperature when the gap vanishes is in the same order as the gap value at zero temperature, further illustrating that the gap Δ is an evaluation of the strength of the binding.

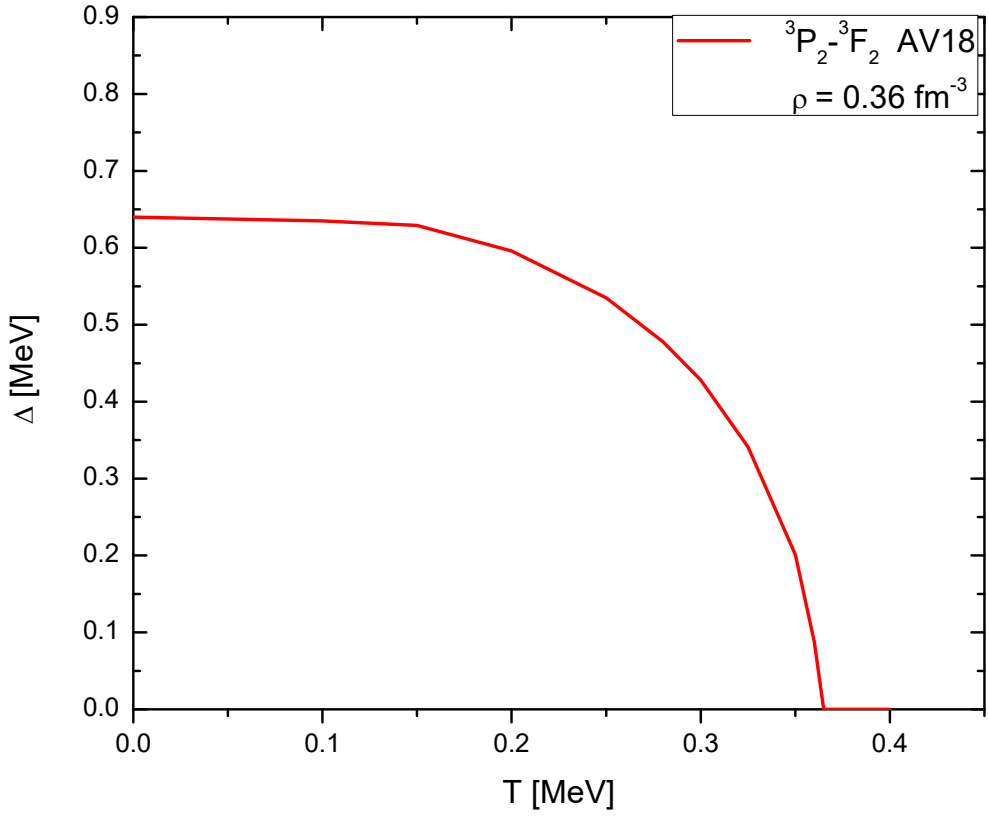

Figure 3.6: The temperature dependence of the gap Δ is calculated for the coupled channel ${}^3P_2 - {}^3F_2$ at density $\rho = 0.36$ fm^{-3} using the bare NN interaction AV18. The gap vanishes at $T = 0.365$ MeV.

3.3 SRC

As mentioned in the previous section, the Gorkov equations can be rearranged by constructing the normal propagator G^N first. This yields the usual normal Dyson equation (see Eq.(3.11)). This is particularly useful for strongly correlated nuclear systems, in which there is already a substantial fragmentation in the normal state *sp* propagator G^N. We note that a similar approach exists for condensed matter systems, particularly in the context of the BCS-BEC crossover [60].

In BCS theory, the interaction term in Eq.(3.21) $\langle p|V_{\ell\ell'}^{JST}|k\rangle$ would simply be a bare NN interaction. However, the effect of the medium is important for the pairing interaction, even at very low densities [61, 62, 63]. We will therefore introduce a description of the screening of V with LRC in Sec. 3.4. In the present section, we concentrate on the modification to the energy denominator, which is characterized by the spectral functions.

3.3.1 Spectral functions

The normal spectral function $A^N(k,\omega)$ is related to the normal component of the self-energy given below

$$A^N(k,\omega) = \frac{-2\mathrm{Im}\Sigma^N(k,\omega)}{[\omega - \frac{k^2}{2m} - \mathrm{Re}\Sigma^N(k,\omega)]^2 + \mathrm{Im}\Sigma^N(k,\omega)^2}. \tag{3.28}$$

It includes information related to *sp* fragmentation in the normal phase [21, 28]. The self-energy has been obtained within a finite temperature $\mathcal{T}$-matrix SCGF approach, discussed in detail in Refs. [64, 65, 66]. At and below the critical temperature, the method is not valid anymore, as evidenced by the appearance of the Thouless pole in the $\mathcal{T}$-matrix [67, 68, 69]. We therefore obtain the normal spectral function at zero temperature by extrapolating finite temperature results down to zero temperature. This is in agreement with the physical

interpretation of A^N as a normal state spectral function. The superfluid spectral function as indicated by Eq.(3.23) can be obtained from the superfluid propagator as

$$A^s(k,\omega) = -2\mathrm{Im}G_{11}(k,\omega), \tag{3.29}$$

where the propagator G_{11} is computed in the superfluid phase. It differs from the normal one by a factor that is proportional to the square of the gap,

$$G_{11}(k,\omega) = G^N_{11}(k,\omega)[1 - G^N_{11}(-k,-\omega)\Delta^2(k,\omega)G_{11}(k,\omega)]. \tag{3.30}$$

Consequently, A^N and A^s only differ from each other close to the Fermi momentum and energy, where pairing effects are more prominent [50, 70].

3.3.2 χ function

A fully self-consistent description of pairing requires an explicit iterative calculation of both A^N and A^s [70]. Here, we take a different approach, an initial step towards a full self-consistent solution that includes all the relevant correlations. First, because the two spectral functions are very similar in a wide energy and momentum domain, we compute the contribution to the effective denominator from the double convolution of normal spectral functions,

$$\frac{1}{2\chi(k)} = \int \frac{d\omega}{2\pi}\frac{d\omega'}{2\pi}A^N(k,\omega)A^N(k,\omega)\frac{1-f(\omega)-f(\omega')}{\omega+\omega'}. \tag{3.31}$$

This will take care of the most of the fragmentation effects on the gap equation. One can indeed generate a superfluid spectral function from the resulting gap [50]. Further calculations of the normal self-energy then in principle require the effect of the gap to be included in the normal propagators [70]. We expect such feedback effects from the superfluid

phase to be small in comparison to the relatively large fragmentation of strength associated with SRC already captured effectively by the χ function in Eq.(3.31).

3.3.3 Zero temperature extrapolation

The normal spectral function at zero temperature $A^N(k,\omega)$ has been computed as an extrapolation of finite temperature self-energies. Numerical results of SCGF ladder approximation self-energies with microscopic NN interactions have been available in the literature for the last decade [71, 65, 66]. The pairing instability, however, precludes a direct calculation within the ladder approximation and normal propagators below the critical pairing temperature T_c [69, 50]. Consequently, for a fixed density, we perform a series of finite temperature calculations to determine the real and imaginary parts of the self-energy, and use these as input for an extrapolation to zero temperature. The fit is further constrained by the macroscopic properties that are computed at $T = 0$, which provide a thermodynamically consistent description of the system. Numerical details are provided in Appendix B. Below, we discuss the properties of the extrapolated self-energies.

The three panels of Fig. 3.7 show the imaginary part of the self-energy as a function of energy, ω, for three characteristic momenta. Panels (a) and (c) show self-energies well below and above the Fermi momentum, respectively, while panel (b) shows the $k = k_F$ case. Results are displayed for the CDBonn interaction at $k_F = 1.33$ fm^{-1} for neutron matter, but equivalent conclusions are found with other NN interactions in this density regime. At large temperatures, there is little (or no) distinction between the hole, $\omega < \mu$, and the particle $\omega > \mu$, parts of ImΣ. As temperature decreases, however, a structure develops close to $\omega \approx \mu$, with ImΣ approaching zero in absolute value. This is the area where temperature plays the most important role, and where the extrapolation procedure is most critical. The momentum and energy dependent polynomial fit, described in Appendix B, captures this

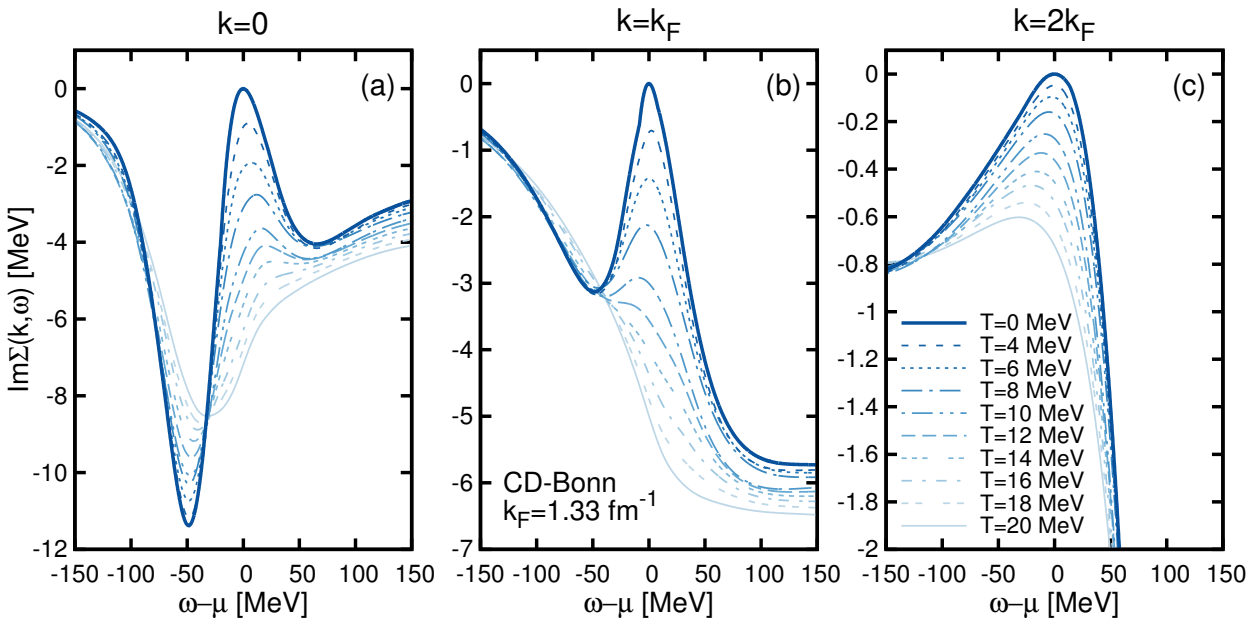

Figure 3.7: Imaginary part of the self-energy around the Fermi energy at $k_F = 1.33$ fm^{-1} for the CDBonn interaction for several temperatures. Panels (a), (b) and (c) correspond to momenta $k = 0$, k_F and $2k_F$, respectively. The $T = 0$ extrapolation is shown in a solid line.

temperature dependence, and provides an extrapolated self-energy which provides consistent results.

From the self-energy, one can obtain other relevant microscopic properties. Panel (a) in Fig.(3.8) shows an example of the temperature extrapolation of the momentum distribution. Again, while this specific example is for the CDBonn interaction at $k_F = 1.33$ fm^{-1}, very similar results are obtained with other forces in a wide density regime. As temperature decreases, one finds the expected behavior for the correlated momentum distribution: the Fermi surface becomes increasingly sharp, and low and high-momentum features build up. As expected, the zero temperature $n(k)$ has a sharp discontinuity across the Fermi surface. The exact shape of the momentum distribution for momenta within a few percent of k_F is sensitive to the extrapolation procedure, particularly to the order of the extrapolating polynomial. However, the implementation of the thermodynamically consistent extrapolation procedure guarantees that, on average, the discontinuity of the Fermi surface is within a few percent of

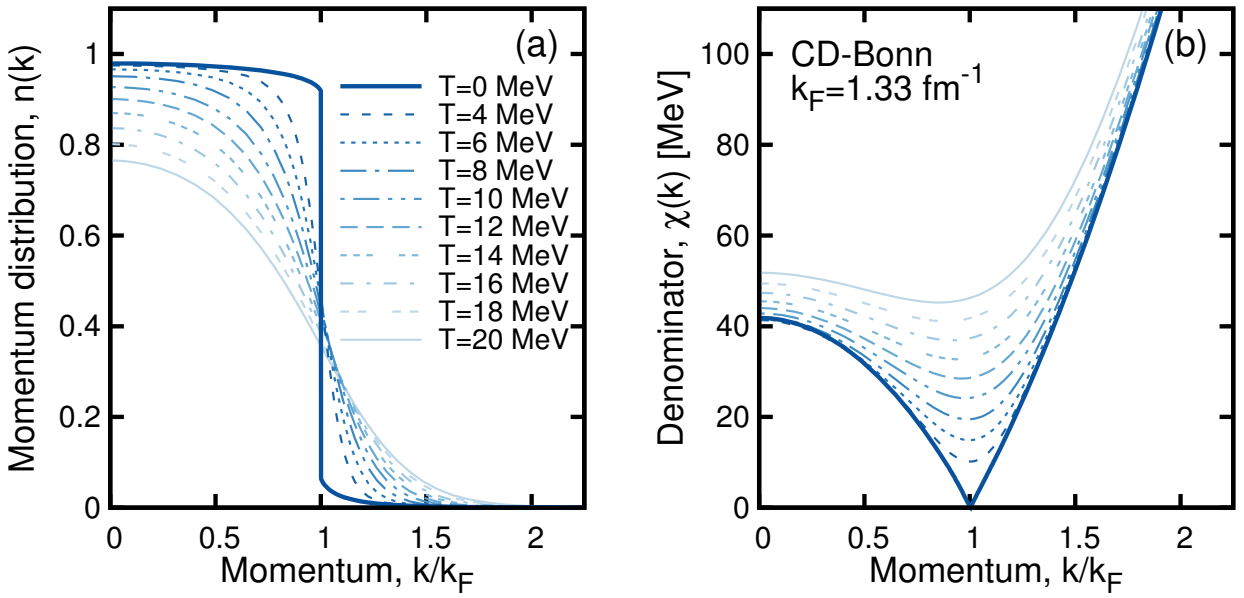

Figure 3.8: Panel (a): momentum distribution at $k_F = 1.33$ fm^{-1} for the CDBonn interaction at different temperatures, including the $T = 0$ extrapolation (solid line). Panel (b): effective *sp* denominator, $\chi(k)$, in the same conditions.

the derivative of the self-energy (i.e. the $\mathcal{Z}$-factor at $k = k_F$). We note that we have corrected the momentum distribution for missing strength effects, as discussed in Appendix B.

3.3.4 Pairing kernel with short range correlations

Pairing calculations require as input the double energy convolution of Eq.(3.31). This is in correspondence to the well-known fact that Cooper pairing appears as a pole in the normal $\mathcal{T}-$matrix in these conditions. The experience gathered in performing the double convolution in SCGF finite temperature calculations is useful in computing the energy denominator [64]. In particular, it is useful to keep track of the quasi-particle energies for each given *sp* momentum, so that the quasi-particle peak is well sampled in the double folding integrals [65].

Pairing calculations, particularly in the $^3P_2 - ^3F_2$ channel, are very sensitive to the Fermi

surface region, and inaccuracies on the double folding are amplified in final gap solutions. In particular, missing strength corrections, analogous to those discussed for $n(k)$ in Appendix B, are essential to compute a continuous energy denominator in regions arbitrarily close to k_F. Panel (b) of Fig.(3.8) shows the energy denominators for a CDBonn calculation at $k_F = 1.33$ fm^{-1} as a function of momenta for a variety of temperatures. Here, as it was the case with $n(k)$, the largest modifications due to temperature occur close to k_F. The low and the high momentum ends of $\chi(k)$ are less sensitive to temperature, and their details are well captured by finite temperature calculations.

The density dependence of the zero-temperature double convolution is displayed in panels (a) to (c) of Fig.(3.9). Each panel represents the results obtained with a different NN interaction: (a) CDBonn [3], (b) Av18 [2] and (c) the Entem-Machleidt N3LO potential [4]. We note that the different NN interactions enter the denominator calculation via the convolution of different extrapolated spectral functions. The spectral functions of these three interactions are relatively dissimilar [28], but the integrated convolution smears out the differences to a certain extent. Consequently, the results obtained for $\chi(k)$ (and its density dependence) are relatively close for all the NN forces.

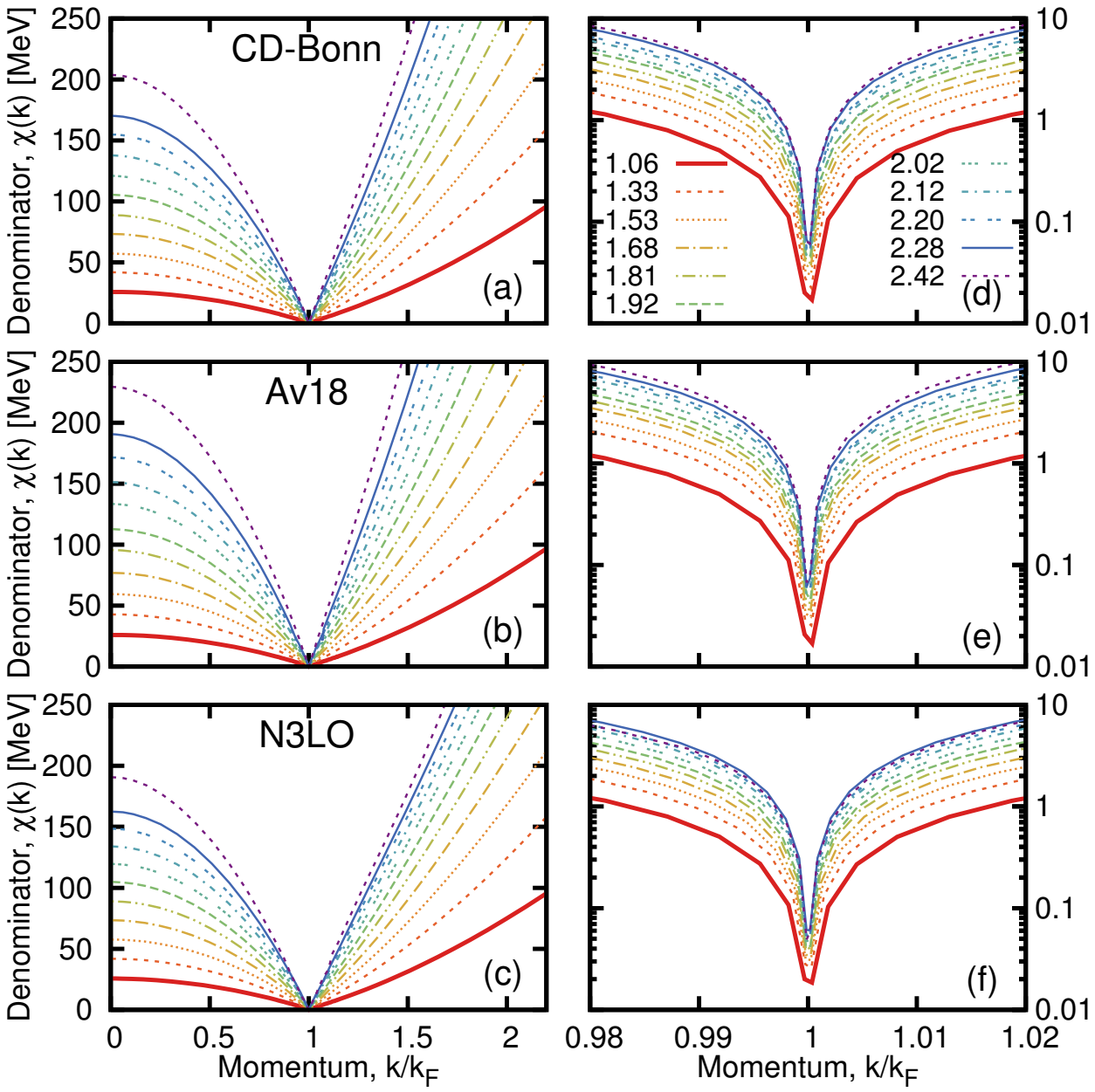

Figure 3.9: Panels (a)-(c): energy denominator at $T = 0$ as a function of momentum for different Fermi momenta, corresponding to the (a) CDBonn, (b) AV18 and (c) N3LO interactions. Panels (d)-(f): the same function, around the Fermi surface, plotted in a logarithmic scale.

In the quasi-particle limit of Eq. (3.17), the denominator reflects the momentum and density dependence of the quasi-particle energy with respect to the chemical potential. We

show the extrapolated zero-temperature quasi-particle denominator in Fig.(3.10), in the same conditions and for the same NN forces as Fig.(3.9). The quasi-particle energies are determined consistently by solving the corresponding implicit equation for the SCGF ladder self-energies,

$$\varepsilon_{\rm qp}(k) = \frac{k^2}{2m} + {\rm Re}\Sigma^N(k, \varepsilon_{\rm qp}(k)), \tag{3.32}$$

and subtracting the chemical potential.

The quasi-particle picture provides an intuitive understanding for the density dependence of the energy denominator. Broadly speaking, the quasi-particle spectrum is more stretched as density increases. Two important conclusions can be drawn from a comparison of Figs.(3.9) and Fig.(3.10). On the one hand, the qualitative density and momentum dependence of the quasi-particle and the double convolution denominators are similar. In particular, both are increasing functions of density. As functions of momenta, the initial decrease below k_F is followed by an increase above the Fermi surface. Furthermore, a linear behavior is found near the Fermi surface in both cases, as expected on general grounds.

On the other hand, there are quantitative differences between both denominators. The double convolution takes into account the fragmentation of quasi-particle states in the normal state. Since strength is removed from the full quasi-particle peak, the denominator becomes larger than the corresponding quasi-particle value. As a matter of fact, the difference between the two results can be parametrized in terms of an effective $\mathcal{Z}-$factor [72, 50],

$$Z^2_{\rm eff}(k) = \frac{E(k)}{\chi(k)}. \tag{3.33}$$

The ratio is displayed, for a subset of relevant densities and three NN forces, in panels (a)-(c) of Fig.(3.11). $Z_{\rm eff}$ is always in the range $\approx 0.8 - 0.9$, and shows a mild momentum dependence, with a minimum close to the Fermi surface. Our results suggest that the

ratio decreases slowly with density. This is in accordance to an intuitive picture, where correlations, measured as a deviation from one in Z_{eff}, become more important at higher densities.

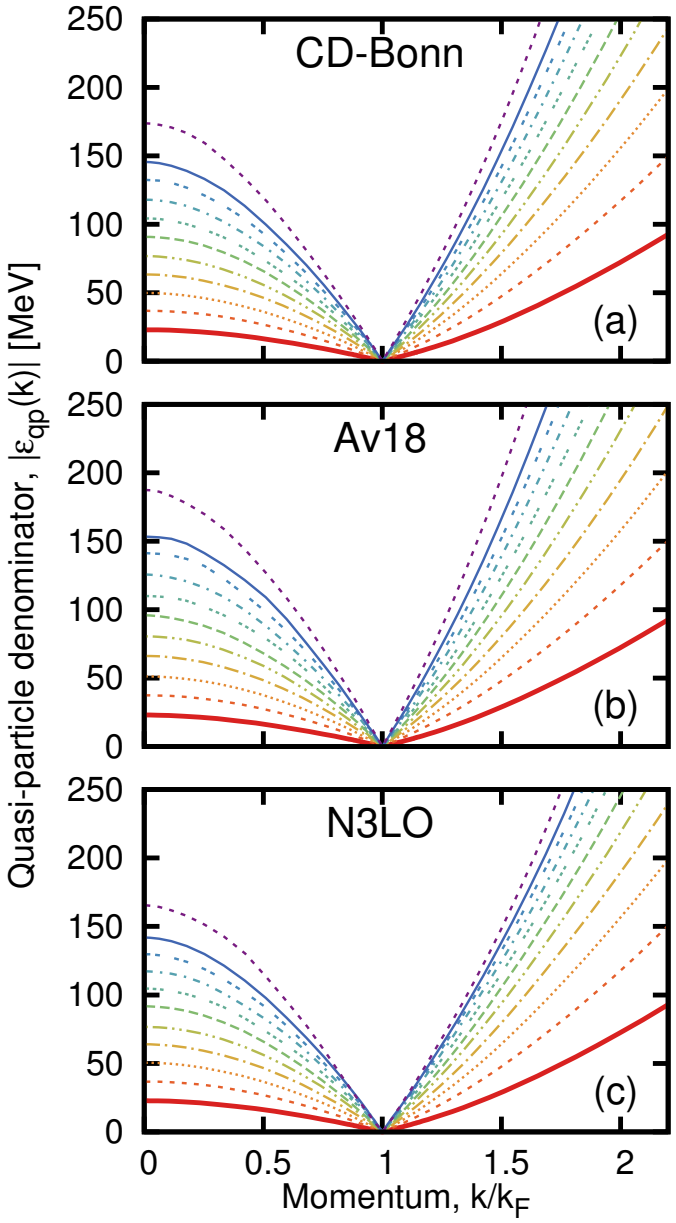

Figure 3.10: Panels (a)-(c): energy denominator at $T = 0$ in the quasi-particle limit as a function of momentum for different Fermi momenta, corresponding to the (a) CDBonn, (b) AV18 and (c) N3LO interactions.

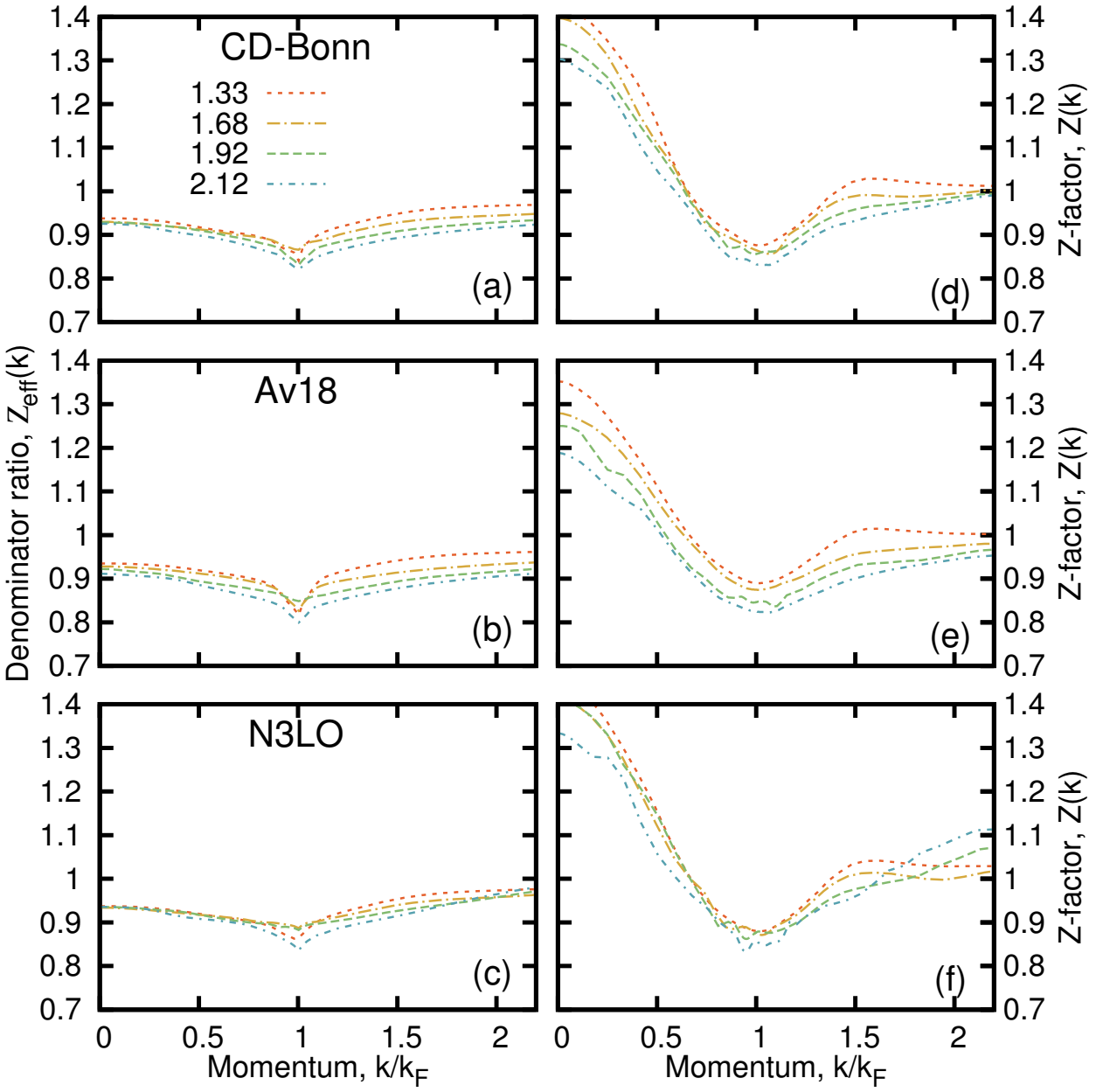

Figure 3.11: Panels (a)-(c): ratio of denominators, Eq. (3.33) at $T = 0$ as a function of momentum for different Fermi momenta. The three panels correspond to the (a) CDBonn, (b) AV18 and (c) N3LO interactions. Panels (d)-(f): the actual Z-factor as a function of momentum in the same conditions.

It is important to stress that the effective denominator ratio, Z_{eff}, is different from the

standard renormalization factor,

$$\mathcal{Z}(k) = \frac{1}{1 - \partial_\omega \mathrm{Re}\Sigma^N(k,\omega)}\bigg|_{\omega=\varepsilon_{\mathrm{qp}}(k)} . \tag{3.34}$$

We show this quantity, computed in the same conditions as Z_{eff}, in panels (d)-(f) of Fig. 3.11. Other than in the vicinity of the Fermi surface, the two renormalization factors provide very different results. $\mathcal{Z}(k)$ is generally well above $Z_{\mathrm{eff}}(k)$. It peaks around $k = 0$ at values of $\approx 1.3 - 1.5$, decreases to a minimum close to k_F and subsequently raises again to ≈ 1 at high momenta. Even though pairing properties are dominated by Fermi surface effects, where both renormalization factors are relatively similar, this comparison shows that a realistic description of the missing strength for pairing purposes cannot be achieved by renormalization-corrected BCS-type approach [62, 56]. In fact, because the removal of strength is underestimated in $\mathcal{Z}(k)$ with respect to Z_{eff}, the corresponding gap is larger in a $Z-$factor corrected BCS approach as compared to a fully correlated description [72]. An additional difficulty is that it is unclear how particle number or density can be properly obtained from this approach.

3.4 LRC

The most important effect of LRC on pairing properties will occur at the level of the effective pairing interaction when neutrons near the Fermi surface exchange possibly collective spin and density modes [57, 61, 73, 74, 75, 52]. Following Refs. [76, 31, 62], we add to the interaction in the generalized gap equation, the corresponding contributions accounting for such fluctuations in a physically motivated way. We adopt the results of Ref. [31], which incorporate an induced interaction that leads to a well-behaved particle-hole interaction (see Fig.(3.12)) that fulfills appropriate stability criteria, not obeyed by interactions that

incorporate only the effect of SRC like *e.g.* $\mathcal{G}$-matrices [77]. The coupling to neutrons that are dressed by the full off-shell effect of SRC as described in the previous section is then governed by the exchange of both a density fluctuation and a spin mode. The collective features of these modes are controlled by self-consistently determined Landau parameters [31]. Their contribution to the pairing interaction requires a recoupling from the particle-hole channel to the particle-particle channel and is therefore different for spin singlet and spin triplet pairing. We note that this is a physically motivated approach to the treatment of LRC that has only been tested in the literature in extensions to BCS theory where SRC are included in terms of renormalization factors [31]. By restricting the effect of LRC to the effective interaction, we can test the effect of both SRC and LRC in pairing properties by turning either correlation effect on or off.

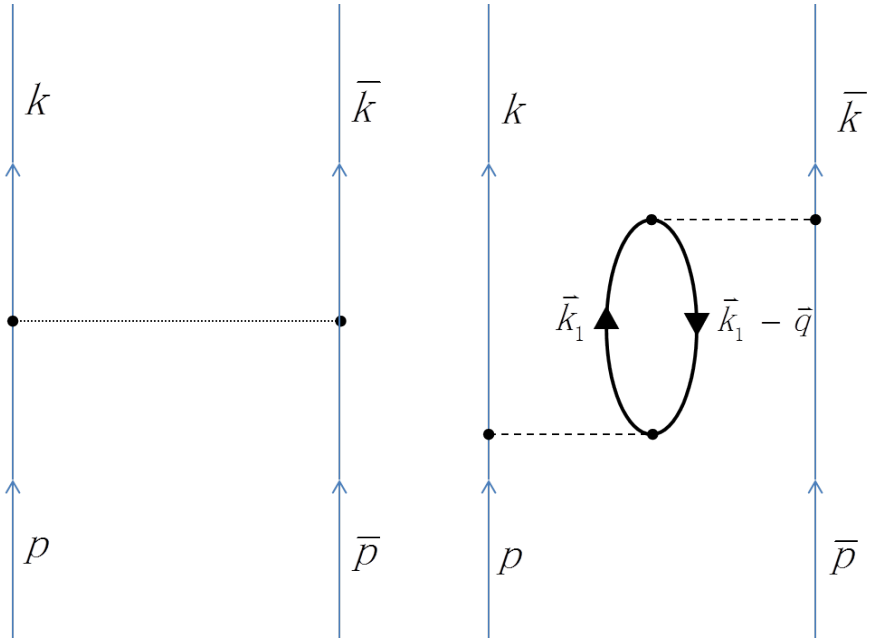

Figure 3.12: Illustration of the exchange of a *ph* excitation (ring) diagram in the right panel compared to the bare interaction in the left panel.

3.4.1 *pp* to *ph* transformation

In general, recoupling of momentum from the *pp* sector to the *ph* sector yields

$$\langle \boldsymbol{p}\bar{\boldsymbol{p}}|V^J|\boldsymbol{k}\bar{\boldsymbol{k}}\rangle = (-1)^J \sum_{J'}(2J'+1)(-1)^{j_p+j_k} \begin{Bmatrix} j_p & j_k & J \\ j_k & j_p & J' \end{Bmatrix} \langle \boldsymbol{p}\boldsymbol{k}|V_{ph}^{J'}|\bar{\boldsymbol{k}}\bar{\boldsymbol{p}}\rangle, \tag{3.35}$$

where momentum quantum numbers are defined as $\boldsymbol{p} = (\vec{p}, \sigma), \bar{\boldsymbol{p}} = (-\vec{p}, -\sigma)$ as shown in Fig.(3.12). Incorporating both spin and isospin generates

$$\langle \boldsymbol{p}\bar{\boldsymbol{p}}|V^{ST}|\boldsymbol{k}\bar{\boldsymbol{k}}\rangle = (-1)^{S+T} \sum_{S'T'}(2S'+1)(2T'+1) \begin{Bmatrix} \frac{1}{2} & \frac{1}{2} & S \\ \frac{1}{2} & \frac{1}{2} & S' \end{Bmatrix} \begin{Bmatrix} \frac{1}{2} & \frac{1}{2} & T \\ \frac{1}{2} & \frac{1}{2} & T' \end{Bmatrix} \langle \boldsymbol{p}\boldsymbol{k}|V_{ph}^{S'T'}|\bar{\boldsymbol{k}}\bar{\boldsymbol{p}}\rangle. \tag{3.36}$$

Working out the above expression for the neutron matter $^1S_0$ channel results in

$$\begin{aligned} \langle \boldsymbol{p}\bar{\boldsymbol{p}}|V_1^{S=0}|\boldsymbol{k}\bar{\boldsymbol{k}}\rangle = \frac{1}{2} \sum_{\boldsymbol{k_1},\boldsymbol{k_1}-\boldsymbol{q}} \sum_{S'} (-1)^{S'}(2S'+1) \langle \boldsymbol{p}\boldsymbol{k}|G_{ph}^{S'}|\boldsymbol{k_1}\boldsymbol{k_1}-\boldsymbol{q}\rangle_A \langle \boldsymbol{k_1}\boldsymbol{k_1}-\boldsymbol{q}|G_{ph}^{S'}|\bar{\boldsymbol{k}}\bar{\boldsymbol{p}}\rangle_A \\ \times \Lambda_0(\boldsymbol{k_1}, \boldsymbol{k_1}-\boldsymbol{q}). \end{aligned} \tag{3.37}$$

where the Lindhard function $\Lambda_0(q)$, averaged around the Fermi surface, represents the bubble diagram in Fig.(3.12). The static Lindhard function, $\Lambda_0(q)$

$$\Lambda_0(q) = \sum_{\hat{\boldsymbol{k}},\hat{\boldsymbol{q}}} \Lambda_0(\boldsymbol{k_1}, \boldsymbol{k_1}-\boldsymbol{q}) = \frac{N(0)}{\mathrm{g}} \frac{1}{2} \left[-1 + \frac{1}{q} \left(1 - \frac{q^2}{4} \right) ln \left| \frac{1-q/2}{1+q/2} \right| \right] \tag{3.38}$$

is employed in Eq. (3.37), with the appropriate density of states $N(0) = \frac{8mk_F}{\hbar^2}$ and degeneracy factor $\mathrm{g} = 2$. We assume as in Ref. [31] that for neutron matter the effective mass in the density of states can be approximated by the bare mass. The static Lindhard function is

iterated to all orders according to

$$\Lambda^S(q) = \frac{\Lambda_0(q)}{1 - \Lambda_0(q)\mathcal{L}^S}\,, \tag{3.39}$$

where $\mathcal{L}^S$ corresponds to the relevant Landau parameter. In the latter calculation, the bubble in Fig.(3.12) will be replaced by the all-order Lindhard function represented by Eq.(3.39). The density mode with total spin 0 in the particle-hole channel is determined by $\mathcal{L}^0$ which is attractive at low density and usually denoted by F_0. The spin mode with total spin 1 is determined by $\mathcal{L}^1$, which is repulsive but has similar magnitude and is often denoted by G_0. Following Eq.(3.37) the interaction that treats LRC for the $^1\mathrm{S}_0$ channel is given by

$$\mathcal{V}_{\mathrm{LRC}}^{S=0} = \tfrac{1}{2}\mathcal{G}_{\mathrm{ph}}^0\mathcal{G}_{\mathrm{ph}}^0\Lambda^{S=0}(q) - \tfrac{3}{2}\mathcal{G}_{\mathrm{ph}}^1\mathcal{G}_{\mathrm{ph}}^1\Lambda^{S=1}(q)\,, \tag{3.40}$$

where $\mathcal{G}_{\mathrm{ph}}^S$ represent the vertices that couple to the spin-S excitation. They can be thought of as particle-hole transformed $\mathcal{G}$-matrix elements averaged around the Fermi energy. As argued in Ref. [31], these vertices are improved by employing the corresponding Landau parameters, as in the original work of Babu and Brown for liquid ^{3}He [78]. Projecting Eq. (3.40) onto $L = 0$, the resulting interaction can then be included into the gap equation for $^1S_0$ pairing for a given density and appropriate values of the Landau parameters.

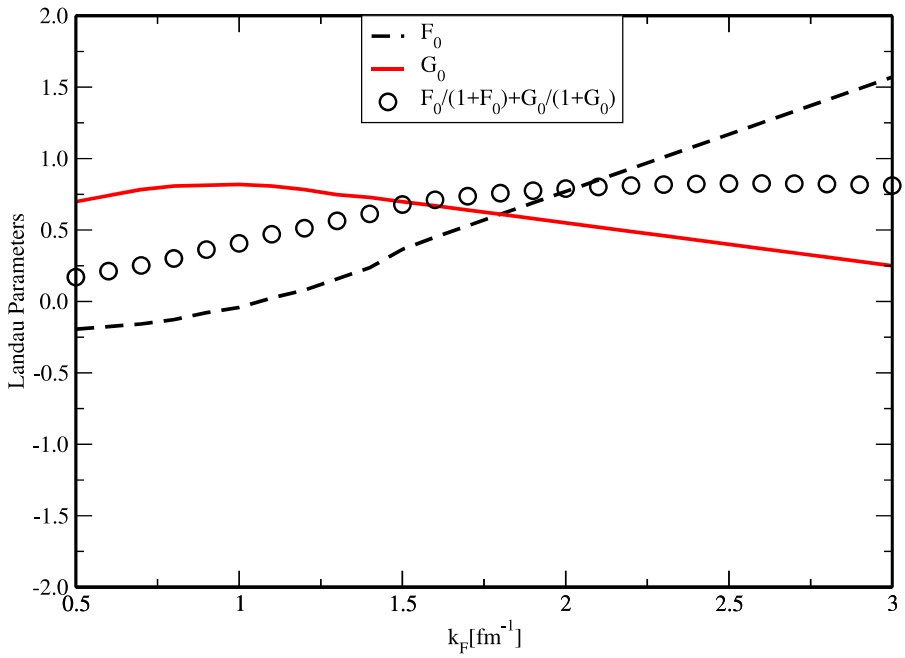

Figure 3.13: Landau parameters F_0 and G_0 extrapolated to $k_F = 3.0$ fm^{-1} employing the results of Ref. [31]. The corresponding value of the forward scattering sum rule is indicated by the open circles.

Both Landau parameters exhibit a modest density dependence in the domain relevant for singlet pairing ($k_F < 1.5$ fm^{-1}). The parameters are adopted from Ref. [31] and are plotted in Fig. 3.13. The first term in Eq. (3.40) is attractive, whereas the second term is repulsive. In the density domain relevant for singlet pairing this repulsion dominates on account of the spin factor leading to an inevitable additional suppression of the gap in this channel. Figure 3.14 illustrates that the additional term, $\mathcal{V}^S_{\rm LRC}$ [panels (c) and (d)], is relatively small compared to the bare interaction [panels (a) and (b)]. For the ^{1}S$_0$ channel, LRC reduce the attraction of the bare Av18 interaction.

The procedure proposed in Ref. [31] is generalized here to the case of the $^3P_2 - ^3F_2$ coupled channel. For the ^{3}PF$_2$ channel which involves spin-1 pairs, the sampling over density and

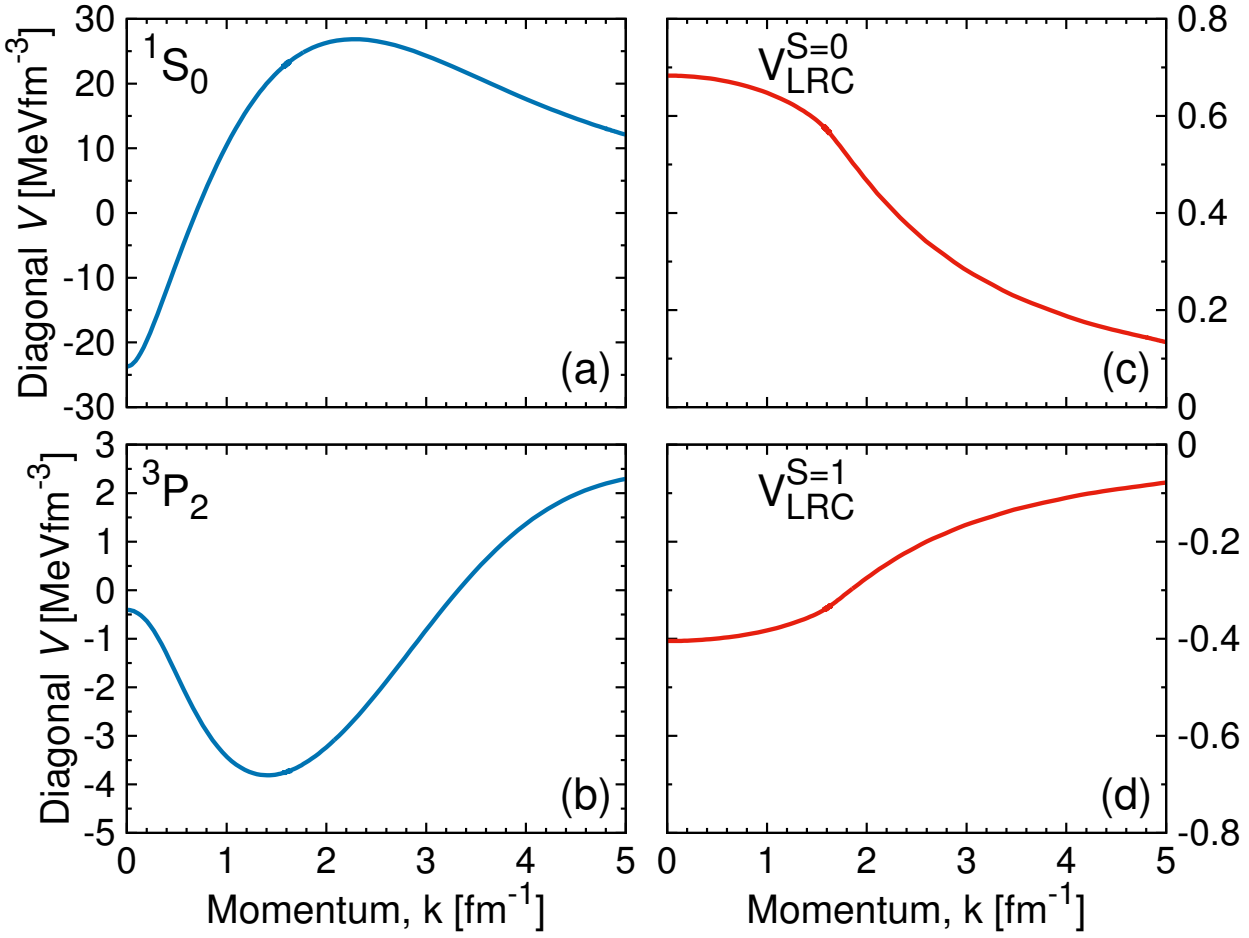

Figure 3.14: Panels (a) and (b): diagonal matrix elements of the Av18 interaction in the (a) $^1S_0$ and (b) $^3P_2$ channels. Panels (c) and (d): diagonal matrix elements of the additional pairing interaction representing the low-energy medium polarization at a density corresponding to $k_F = 1.6$ fm^{-1} in the same channels. The scales are different for each plot.

spin modes becomes:

$$\mathcal{V}_{\rm LRC}^{S=1} = \tfrac{1}{2}\mathcal{G}_{\rm ph}^{0}\mathcal{G}_{\rm ph}^{0}\Lambda^{S=0}(q) + \tfrac{1}{2}\mathcal{G}_{\rm ph}^{1}\mathcal{G}_{\rm ph}^{1}\Lambda^{S=1}(q)\,, \tag{3.41}$$

with both terms yielding attraction. Contrary to the ^{1}S$_0$ channel, this contribution will always lead to antiscreening of the gap, as it represents an attractive interaction. This point is illustrated in panel (d) of Fig. 3.14, which shows the relatively small but nevertheless attractive contribution of the LRC interaction in the $S = 1$. This is to be compared to the bare interaction in the ^{3}P$_2$ channel, shown in panel (b).

The Landau parameters F_0 and G_0 from Ref. [31] are extrapolated to higher densities in a smooth way as shown in Fig. 3.13. We also include the contribution to the forward scattering sum rule of the Landau parameters F_0 and G_0 in Fig. 3.13 indicated by the open circles (see *e.g.* Refs. [77, 79, 80]). While the extrapolated Landau parameters are both positive at higher density, the forward scattering sum rule is nevertheless approximately fulfilled when one allows for a negative contribution of the Landau parameter F_1 (for example of about -0.5 [80]) to the sum rule given by $F_1/(1 + F_1/3)$. The extrapolation introduces some uncertainty in the effect of LRC for triplet pairing at higher density, but it should be emphasized that Eq. (3.41) leads to antiscreening whatever the numerical values or sign of the Landau parameters F_0 and G_0. Moreover, this small correction is motivated by well-explored many-body theory principles.

In future work, we intend to generate the Landau parameters from a consistent evaluation starting from the ladder-summed effective interaction. A proper inclusion of the induced interaction with this starting point is however considerably beyond the scope of the present work. In future, the possibility that the presence of the pion-exchange tensor interaction strongly influences the spin mode should also be investigated (see also Ref. [81]). A proper treatment of retardation implied by the possibility of exchanging low-lying density and spin

modes in principle generates a complex solution of the gap equation which should also be investigated further (see *e.g.* the work of Ref. [82] for a calculation with a dynamic pion-exchange interaction).

3.5 Results

3.5.1 Singlet pairing

Figure (3.15) provides the pairing gaps in the $^1S_0$ channel in neutron matter for four different approximations, computed at the corresponding Fermi surfaces. Results for the CDBonn, Av18 and N3LO NN forces are displayed in panels (a)-(c), respectively. Solid lines represent the standard BCS solution, computed using free *sp* spectra. The BCS+LRC results (empty squares) have been obtained by replacing the bare NN forces in the gap equation, Eq.(3.21), by the dressed effective interactions of Eq.(3.40). SRC results (empty circles) are computed with bare NN forces, but double convolution denominators in the gap equation. Finally, the full circles are obtained from the full denominators and LRC-corrected effective interactions.

The BCS results (solid line) are very similar for all forces, which confirms that phase-shift equivalence is enough to fix the value of the gap in this channel [35]. The BCS gap peaks at about 3 MeV around $k_F = 0.7$-0.8 fm^{-1}, and closes at $k_F \approx 1.5$ fm^{-1}. As mentioned above, LRC in this channel screen part of the attraction of the NN forces. Consequently, BCS+LRC gaps (squares) are generally smaller than BCS results. While the overall Fermi momentum dependence is similar, including a similar closure density, the maximum of Δ decreases to about ≈ 2.5 MeV. It is important to stress that the result is similar for all interactions. In other words, the LRC screening is the same independently of the NN force, including the

very soft N3LO and the very hard Av18 forces.

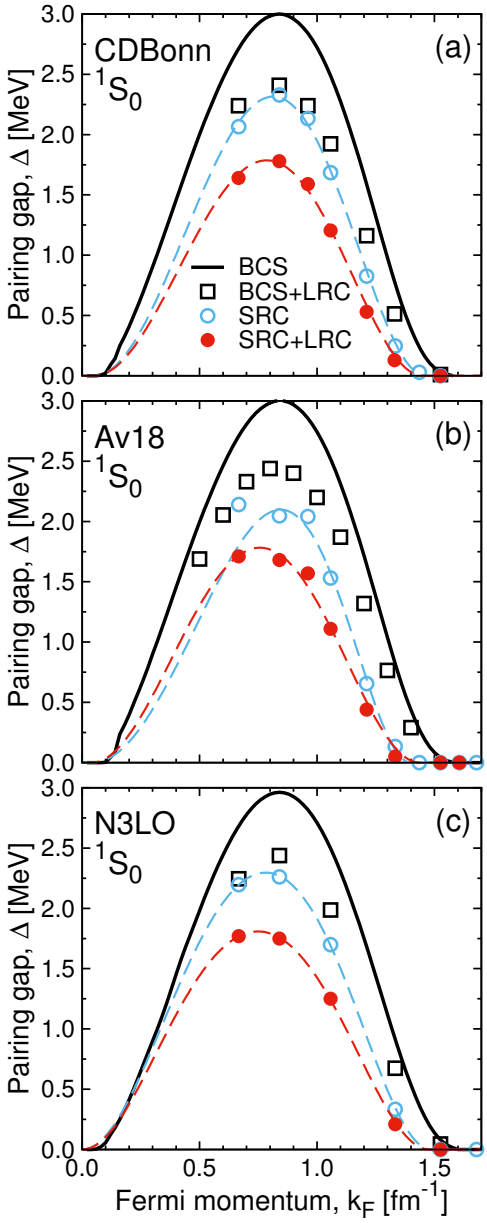

Figure 3.15: Pairing gaps at the Fermi surface as a function of Fermi momentum in the $^1S_0$ channel. The three panels correspond to the (a) CDBonn, (b) Av18 and (c) N3LO interactions. Results for different approximations are presented: BCS (solid lines), SRC (empty circles), LRC(empty squares) and both SRC and LRC included (solid circles). The dashed lines represent the fits provided in Table 3.1.

Including SRC within the Green's function formalism outlined above (empty circles), we find

that the overall gap is reduced, with a maximum that now sits just above 2 MeV, and a similar density dependence. This result is expected: by removing strength from the Fermi surface, the pairing phase space is quenched and the corresponding pairing gap decreases by about 30%. The mild density dependence of $Z_{\rm eff}$ also explains why the BCS and the SRC results have similar density dependences. There is a tendency to have a slightly lower closure density for the SRC results, a feature we shall discuss further when we introduce numerical parametrizations below.

Finally, the complete results including both SRC and LRC are shown in full circles in Fig.(3.15). Screening effects in this channel are repulsive, and as a consequence the corresponding LRC+SRC gaps decrease in size by about 25% with respect to the SRC only data. These gaps peak at values of around 1.8 MeV, for Fermi momenta close to 0.75 fm^{-1}. While the overall density dependence is similar to the previous results, we note a tendency to find an even lower gap closure density.

For a given channel, a convenient parametrization of the density dependence of the gap function is given by:

$$\Delta_L^{JST}(k_F) = \Delta_0 \frac{(k_F - k_0)^2}{(k_F - k_0)^2 + k_1} \frac{(k_F - k_2)^2}{(k_F - k_2)^2 + k_3}\,, \tag{3.42}$$

with Δ_0, k_0, k_1, k_2 and k_3 numerical parameters [83]. In particular, k_0 and k_2 represent the Fermi momenta at which the gap opens and closes, respectively. We note that this parametrization is particularly sharp around the closure points, and that in the singlet channel we supplement the fit with a zero value at zero density. We show in Table 3.1 the values of the parameters obtained for these fits. Further, we note that the dashed lines shown in Fig. 3.15 correspond to the fit functions.

The fit function does reproduce the qualitative shape of the pairing gap. We take k_2, dis-

Table 3.1: Parameters generated by a fit to the calculated gaps for the Av18, CDBonn, and N3LO interactions in the $^1S_0$ channel. For each interaction, the first line contains the results for the inclusion of SRC only, and the second the effect of both SRC and LRC.

Singlet	Δ_0 [MeV]	k_0 [fm^{-1}]	k_1 [fm^{-2}]	k_2 [fm^{-1}]	k_3 [fm^{-2}]
CDBonn SRC	26.59	0.05	1.79	1.46	0.76
CDBonn SRC+P	18.18	0.05	1.39	1.45	0.81
Av18 SRC	32.22	0.04	3.46	1.40	0.43
Av18 SRC+P	14.07	0.04	1.00	1.44	0.78
N3LO SRC	7.77	0.00	0.56	1.49	0.38
N3LO SRC+P	5.85	0.00	0.46	1.48	0.42

played in column 5 of Table 3.1, as a measure of the gap closure density. The confidence interval associated to the fit is within 0.12 fm^{-3} (for the worst fit) from the central value. We note that there is a robust agreement of gap closures, which for all forces and many-body approaches sits between 1.4 and 1.5 fm^{-1}.

This parametrization also allows a simple quantitative estimate of the gap maxima, and their location. For instance, the SRC maximum gap lies between $k_F = 0.78$ (N3LO), 0.81 (CDBonn) and 0.84 fm^{-1} (Av18), at a value between $\Delta^{^1S_0}_{\rm max} = 2.1$ MeV (Av18) and 2.3 MeV (CDBonn and N3LO). Similarly, the SRC+LRC results peak between $k_F = 0.75$ (N3LO), 0.76 (Av18) and 0.79 fm^{-1} (CDBonn) to maximum gaps of the order of $\Delta^{^1S_0}_{\rm max} = 1.8$ MeV for all three NN interactions.

We note that similar gaps have already been obtained in the literature. A comparison with the compilation of Ref. [83] shows that our results are close to the Cao-Lombardo-Schuck (CLS) [31] and Margueron-Sagawa-Hagino (MSH) [84] singlet gaps. MSH is fit to the CLS results, so the agreement between the two is not surprising. Our results include LRC in a way that is similar to CLS, but we note that the SRC physics is considered only at the $\mathcal{Z}-$factor level in a Brueckner–Hartree–Fock calculation, and hence misses hole-hole correlation effects.

All in all, the picture that arises for the singlet gaps provided by the three interactions is *remarkably robust*. The small variation of the results among NN forces provides an insightful constraint on the model dependence of the gap properties. In spite of their different short-range and (less relevant for neutron matter) tensor components, the 3 interactions considered here predict singlet gaps which are very close to each other. More importantly, the many-body effects are very similar in all cases. SRC deplete the gap by about 25 %. When LRC are included on top of SRC, the gap that remains is around 60 % of the original BCS result for all forces. The effect of the correlation-induced gap quench in pairing properties, like the Cooper pair coherence length [85], or neutron star properties [83], go beyond the scope of the present paper and will be studied elsewhere.

The robustness of the singlet gap results with and without correlation effects is one of the major conclusions of this work. We note, however, that this result is not necessarily easily anticipated. The gap itself is a function of both Fermi momentum, k_F, and *sp* momentum, k. So far, we have focused on the values at the Fermi surface, $\Delta_L^{JST}(k = k_F)$, but the momentum dependence provides useful information, too. In particular, as we are about to show, very different momentum dependences can lead to similar gaps at the Fermi surface.

3.5.2 Triplet pairing

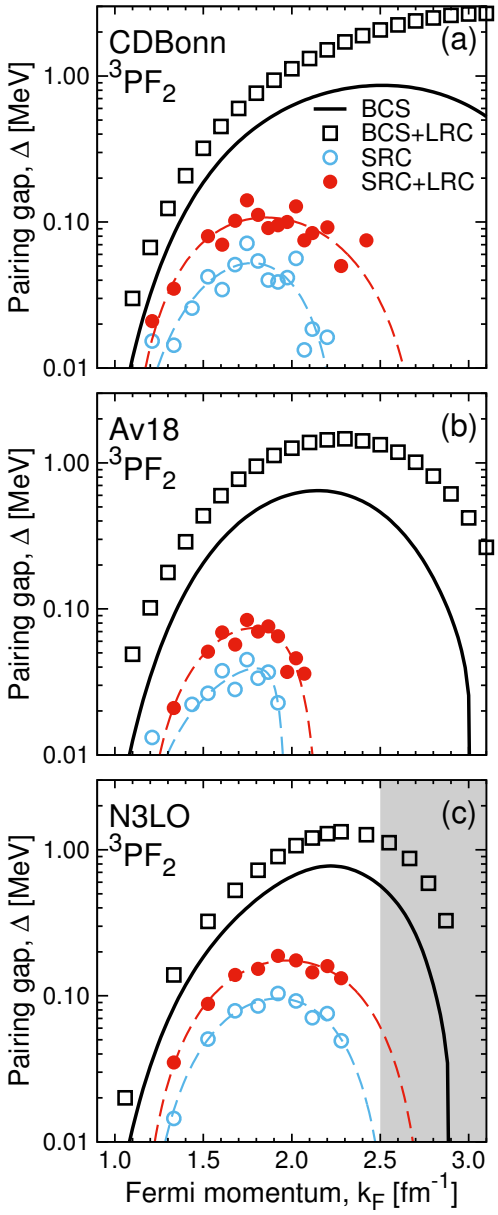

Figure 3.16: The same as Fig.(3.15) for the coupled $^3P_2 - ^3F_2$ channel. The grey band on panel (c) indicates the region in which cut-off effects are relevant for the N3LO force.

Whereas singlet pairing is active at relatively low densities and affects the dynamics of both the core and the crust, triplet pairing, concerning the coupled $^3PF_2$ channel, takes

place within the neutron star core, at Fermi momenta $k_F > 1$ fm^{-1} [83, 36]. Higher Fermi momenta imply that higher relative momenta are explored in the bare (or the effective) interaction. Because phase-shift equivalent interactions are constrained only at low energies and relative momenta, it is not surprising that the corresponding gaps show a larger dependence on the NN force. We show the triplet gaps for 3 NN forces in panels (a)-(c) of Fig.(3.16). We use a logarithmic scale to discriminate better the results of different many-body approximations.

Differences between NN forces are already significant at the BCS level (solid lines). All gaps open at Fermi momenta around $k_F \approx 1.1$ fm^{-1}. Triplet gaps peak around 2-2.5 fm^{-1}. CDBonn provides the largest maximum ($\Delta^{^3PF_2}_{\rm max} = 0.86$ MeV at $k_F \approx 2.5$ fm^{-1}), followed by N3LO ($\Delta^{^3PF_2}_{\rm max} = 0.77$ MeV at 2.2 fm^{-1}) and Av18 ($\Delta^{^3PF_2}_{\rm max} \approx 0.64$ MeV at $k_F = 2.1$ fm^{-1}). In turn, the gap closure happens at larger densities for interactions with larger gaps. For CDBonn, the closure occurs at a very high density, $k_F \approx 3.64$ fm^{-1}, beyond the limit of Fig.(3.16). Av18 and N3LO, instead, provide BCS closure momenta between 2.9 and 3 fm^{-1}.

N3LO results are sensitive to the cut-off regularization of the NN force at large Fermi momenta [86]. The grey band in panel (c) of Fig.(3.16) indicates the region in which regularization effects become observable. It is important to stress that the two similar gap closures for Av18 and N3LO are indicative of two very different physical effects. This can be easily seen in Fig.(3.17), where we show on the left (right) panels density plots for the ^{3}P$_2$ (^{3}D$_2$) matrix elements of the three NN forces. A gap can only appear if attractive matrix elements of $\mathcal{V}$ are available. Consequently, N3LO can only sustain a gap up to about ≈ 3 fm^{-1} because its matrix elements are regularized, and hence tend to zero, beyond this momentum. In contrast, Av18 does have non-zero, rather repulsive matrix elements beyond about ≈ 4 fm^{-1}. It is the appearance of these repulsive matrix elements that forbids pairing above the

closure momentum for Av18. Focusing on the top panels, these also illustrate why CDBonn will sustain gaps up to larger Fermi momenta. The attractive nature of its partial waves matrix elements covers a large relative momentum region.

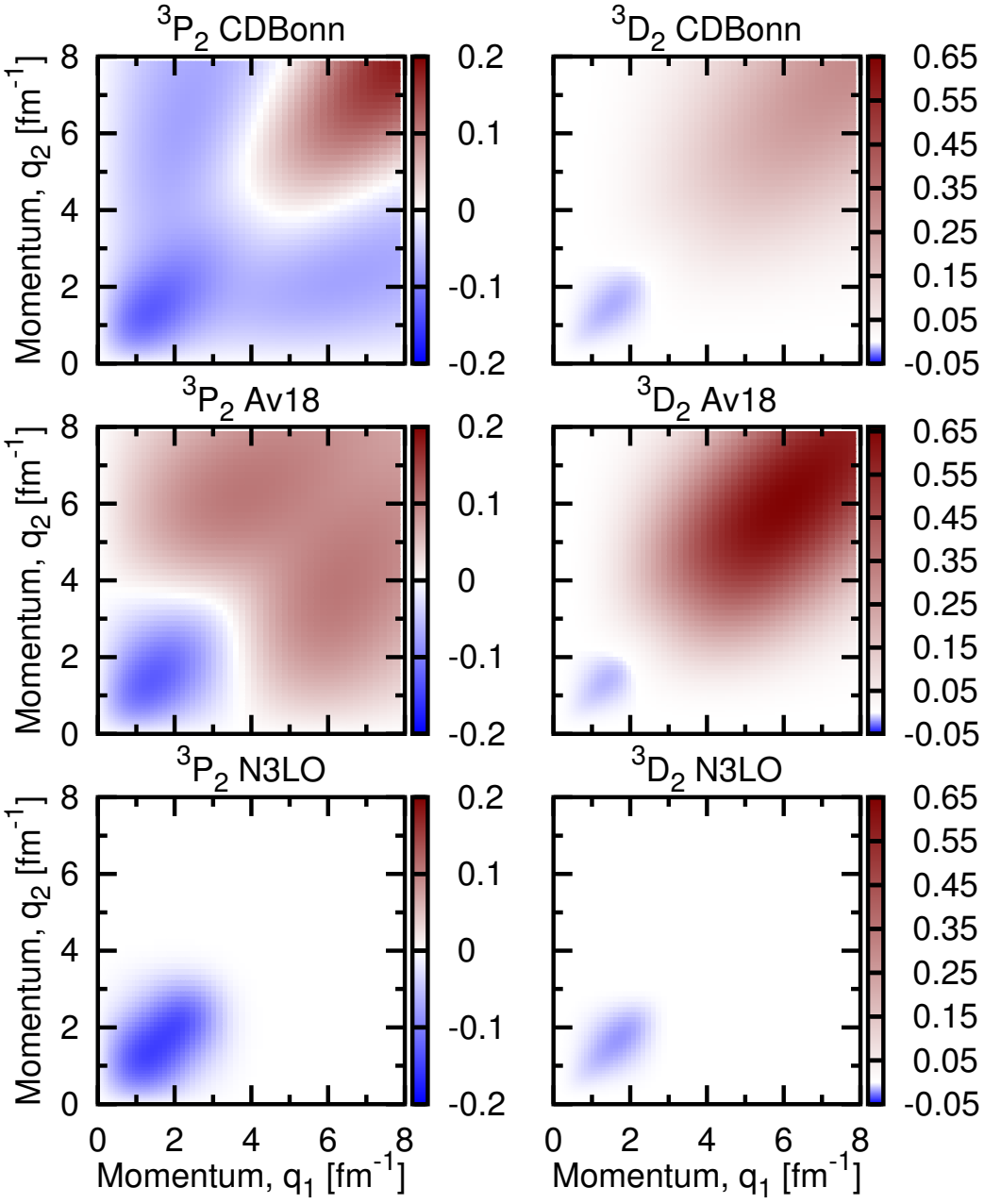

Figure 3.17: Left panels: matrix elements of NN forces in fm for the $^3P_2$ partial wave. Right panels: the same for the $^3D_2$ wave.

In contrast to the singlet case, the inclusion of LRC on top of the BCS result leads to higher gaps. This result is in line with the discussion of Sec. 3.4, because in this channel LRC are attractive and anti-screen the interaction. The effect is rather significant, with the Av18 BCS+LRC gap becoming more than a factor of 2 larger than the original BCS result. The density dependence is also modified by LRC.

When SRC are considered (empty circles), all $^3PF_2$ gaps are strongly suppressed. All the maximum triplet gaps fall below 0.15 MeV: 0.04 MeV for Av18, 0.05 for CDBonn and about 0.1 MeV for N3LO. The density dependence of these gaps is also different than the BCS prediction. The data for the SRC and SRC+LRC is relatively noisy, due to the numerical limitations of the zero temperature extrapolation discussed in Appendix B. Nevertheless, the gross features of the SRC effects are rather clear.

If we take the k_0 parameter of the fits presented in Table 3.2 as an indication of gap opening, triplet gaps start at $k_F \approx 1.1$ fm^{-1} for all forces. The corresponding gap maxima occur at $k_F = 1.77$, 1.79 and 1.92 fm^{-1} for CDBonn, Av18 and N3LO, respectively. This is to be compared to the substantially larger BCS values of $\approx 2 - 2.5$ fm^{-1}. Finally, the gap closure occurs at lower Fermi momenta for the SRC gaps (see column 5 in Table 3.2) than the corresponding BCS. N3LO predicts the larger closure at $k_F \approx 2.8$ fm^{-1}, whereas the lowest is given by Av18 at 2.0 fm^{-1}. All in all, SRC triplet gaps are smaller and exhibit a smaller density range than their corresponding BCS counterparts.

LRC, when considered in addition to SRC (solid circles), do not change the picture qualitatively. In this channel, spin-density fluctuations lead to a more attractive pairing interaction, and hence LRC increase the triplet pairing gap by a small percentage. LRC+SRC start at similar Fermi momenta than their SRC-only counterparts. The maximum gap that is produced, however, is almost twice as large: 0.17 MeV for N3LO, 0.11 for CDBonn and 0.07 MeV for Av18. The corresponding Fermi momentum maxima are similar, $k_F = 1.86$, 1.79

Table 3.2: Parameters generated by a fit to the calculated gaps for the Av18, CDBonn, and N3LO interactions in the $^3PF_2$ channel. For each interaction, the first line contains the results for the inclusion of SRC only, and the second the effect of both SRC and LRC.

Triplet	Δ_0 [MeV]	k_0 [fm^{-1}]	k_1 [fm^{-2}]	k_2 [fm^{-1}]	k_3 [fm^{-2}]
CDBonn SRC	0.60	1.01	2.21	2.33	0.43
CDBonn SRC+P	0.41	1.03	0.56	2.81	1.00
Av18 SRC	0.09	1.01	0.64	1.98	0.005
Av18 SRC+P	0.17	1.10	0.35	2.18	0.05
N3LO SRC	0.43	1.13	0.83	2.59	0.41
N3LO SRC+P	0.60	1.11	0.69	2.79	0.53

and 1.98 fm^{-1} for CDBonn, Av18 and N3LO, respectively. Because of the larger maxima, gap closures occur at larger Fermi momenta, with two interactions (CDBonn and N3LO) closing the gap at $k_F = 2.8$ fm^{-1}, and the remaining one, Av18, at 2.2 fm^{-1}.

All in all, our prediction for triplet gaps are also reasonably robust, and independent of the NN force. Triplet gaps are always at the level of 10′s of keV, peaking at Fermi momenta in the region $1.7 - 2$ fm^{-1} and closing earlier than the BCS predictions. To compare with previous literature in similar conditions, we consider the results of Dong *et al.* in Ref. [62]. They use the Av18 interaction and parametrize SRC in terms of $\mathcal{Z}-$ factors. The maximum triplet gap in that calculation is 0.045 MeV at $k_F \approx 1.6$ fm^{-1}, in very good agreement to our SRC result (0.04 MeV at 1.79 fm^{-1}). We note that none of the gaps considered in the recent astrophysically motivated compilation of Ref. [83] resemble our predictions. However, the maximum gaps that we produce compare well with the inferred value of triplet critical temperatures of Ref. [36], $T_c = 5 \times 10^8$ K $\Rightarrow \Delta_{\rm max}^{^3PF_2} \approx 0.08$ MeV.

The agreement between the different NN interactions is not trivial, as we have discussed in the singlet case. We have already illustrated the very different momentum-space structure of the triplet components of the NN forces in Fig.(3.17). The BCS results (dashed line) begin at zero, as expected from non-S-wave pairing, peak close to the Fermi surface, and

subsequently decay. While CDBonn and Av18 show an inflection point at $k \approx 4$ fm^{-1} and decay slowly with momentum, N3LO decays to zero even at lower values of momentum. The corresponding SRC gaps show qualitatively similar behaviors and peaks, but are generally an order of magnitude smaller. There are differences in the density dependence, too. In any case, this figure illustrates the fact that, unlike the singlet case, triplet pairing gaps are more sensitive to the short-range (or, equivalently, high-momentum) components of the NN force.

Chapter 4

First and higher order self-energy for elastic scattering

4.1 Introduction

In the Green's function language, a well-constructed self-energy describes important physics from SRC in nuclear matter or nuclei to elastic nucleon nucleus cross sections. One of the ways of constructing the self-energy in the nucleon-nucleus scattering analysis is the dispersive optical models (DOM) [41]. The optical potential that describes nucleon-nucleus elastic scattering properties can be parametrized and includes an imaginary part as required by experimental data. Recently, nonlocality has been added to the fitting procedure leading to a much better description of the charge density of ^{40}Ca in Ref [42] when also properties of the ground state are simultaneously described. Instead of using phenomenological optical potentials, the very same processes can be explored starting from a purely microscopic interaction. *Ab-initio* calculations of the self-energy take the bare NN interactions as an intrinsic building block, follow the Feynman-like diagrams order by order and make relevant

approximations [30]. More ambitiously, one may apply the self-consistent Green's function (SCGF) method to polish the initial inputs, which usually comes from mean-field calculations. In the *ab-initio* case, the idea of folding the $\mathcal{T}-$matrix with the nuclear density ρ to build the optical potential has been in the literature for decades [43, 44], and is known as the $\mathcal{T} \times \rho$ method. By using a mean-field density matrix, it successfully describes experimental scattering data for nuclei in the energy range 80-400 MeV although it fails with polarization data. However, the method requires avoiding the deuteron pole in the energy dependence of the $\mathcal{T}-$matrix by fixing the energy at the beam energy corresponding to NN scattering [43], which is not optimal considering that the $\mathcal{T}-$matrix has a strong energy dependence. We will discuss a different way to avoid the deuteron pole automatically by using the more realistic DOM spectral density in Sec. 4.4. Another relatively older semi-microscopic method–the nuclear matter approach of Jeukenne, Lejeune and Mahaux (JLM) [87, 88] has also been quite successful since the 1970s. The JLM model uses a local density approximation (LDA) without any dispersion correction and it also needs different parameterizations for neutron and proton projectiles [89], in that sense the DOM including nonlocality is a more accurate method as shown in Ref. [42]. A comparison between the DOM and the microscopic self-energy can then be made to provide insight into the underlying physics.

In this chapter, we will provide a first step in such a SCGF calculation, constructing the first order HF term plus the higher order ladder diagram contribution to the self-energy. The HF term is built from the bare interaction and a given density matrix, which is taken from the DOM input. The ladder self-energy term is the combination of the ladder vertex function (the *pp* part is also known as the $\mathcal{T}-$matrix) and the spectral functions again from the DOM. To reproduce reasonable results in high energy nucleon scattering, more than 20 partial wave channels should be summed, which makes the numerical treatment complicated. In order to avoid this difficulty, the vector basis is employed, more specifically, in the momentum representation. Taking advantage of the rotational symmetry of the microscopic interaction, the

procedure can be simplified. Nevertheless, the rotational symmetry treatment itself requires a lot of attention, which is presented in the Sec. 4.2. It is particularly worthwhile when it comes to the actual numerical implementation and the future self-consistent treatment in which a fully *ab-initio* optical potential is constructed.

4.2 Rotational symmetry

In the most general way, a one-body operator $\mathcal{O}$, which does not affect total spin or total angular momentum, given in a partial wave representation can be transformed back to a vector-basis representation. The matrix elements are:

$$\mathcal{O}_{\boldsymbol{k}'\boldsymbol{k}}^{m_s' \; m_s} = \langle \boldsymbol{k}' \; m_s' | \mathcal{O} | \boldsymbol{k} \; m_s \rangle. \tag{4.1}$$

Note that although the operator conserves the total spin, it still can change (flip) the spin projections. We can express the states in terms of the coupled partial wave basis by:

$$|\boldsymbol{k} \; m_s\rangle = \sum_{j m_j \ell m_\ell} (\ell \; m_\ell s \; m_s | j \; m_j) Y_{\ell m_\ell}^*(\Omega) | k \; (\ell s) \; j \; m_j \rangle. \tag{4.2}$$

Substituting Eq.(4.2) into Eq.(4.1), the matrix elements can be written as :

$$\mathcal{O}_{\boldsymbol{k}'\boldsymbol{k}}^{m_s' \; m_s} = e^{-i m_s' \; \phi'} \sum_{m_j} \mathcal{O}_{\underline{k}' \; \underline{k}}^{m_s' \; m_s}(m_j) e^{i m_j (\phi' - \phi)} \; e^{i m_s \phi}, \tag{4.3}$$

where the explicit azimuth angles labeled by ϕ and ϕ' only appear in the form of phases when the total angular momentum $\boldsymbol{j}$ is parallel to the $z-$axis. The additional angular dependence is implicit in the notation: $\underline{k} = (k, \; X_k) = (k, \; \cos(\theta_k))$. Therefore, we only need to worry about $\mathcal{O}_{\underline{k}' \; \underline{k}}^{m_s' \; m_s}(m_j)$ for now. The transformation from the partial wave basis to vector basis

yields:

$$\mathcal{O}^{m_s' \; m_s}_{\underline{k}' \; \underline{k}}(m_j) = \frac{(-1)^{2m_j - m_s - m_s'}}{4\pi} \sum_{\ell j} (\ell \; m_j - m_s \; s \; m_s | j \; m_j) \tag{4.4}$$
$$\times (\ell \; m_j - m_s' \; s \; m_s' | j \; m_j)(2\ell + 1)$$
$$\times \sqrt{\frac{(\ell - m_j + m_s')!}{(\ell + m_j - m_s')!}} \sqrt{\frac{(\ell - m_j + m_s)!}{(\ell + m_j - m_s)!}}$$
$$\times P_{\ell \; m_j - m_s'}(X_k') P_{\ell \; m_j - m_s}(X_k)$$
$$\times \mathcal{O}^{(\ell s) j}_{k' k}.$$

Note that any one particle operator that commutes with the total spin and total angular momentum can be written in the form in Eq.(4.3). Now consider the rotation invariance of the operator $\mathcal{O}$,

$$\langle \boldsymbol{q} m_s' | \mathcal{O} | \boldsymbol{k} m_s \rangle = \langle \boldsymbol{q} m_s' | \mathcal{R} \mathcal{O} \mathcal{R}^\dagger | \boldsymbol{k} m_s \rangle, \tag{4.5}$$

where $\boldsymbol{k} = (k, \; 0, \; 0)$ is chosen to be parallel to the $z-$axis and $\boldsymbol{q} = (q, \; \theta_q, \; \phi_q)$. If a rotation about the $z-$axis is performed by $\mathcal{R}(-\phi_q \hat{\mathbf{z}})$, a phase is generated as follows:

$$\langle \boldsymbol{q} m_s' | \mathcal{O} | \boldsymbol{k} m_s \rangle = e^{i(m_s - m_s')\phi_q} \langle \boldsymbol{q}' m_s' | \mathcal{O} | \boldsymbol{k} m_s \rangle. \tag{4.6}$$

From this point of view the only dependence on the azimuth angle is a phase, the matrix elements of the operator $\mathcal{O}$ depend only on the magnitudes of the momenta $\boldsymbol{k}$ and $\boldsymbol{q}$, and the angle between them. In the case of our Hartree-Fock calculation, Eq.(4.6) is satisfied by the Hartree-Fock self-energy and also by the density matrix operator. Therefore, we should try to exploit these symmetries to simplify the calculation.

4.2.1 HF contribution

The correlated HF self-energy contribution (see Fig.(4.1)) to the one-particle propagator depends on the density matrix n, as follows:

$$\langle \boldsymbol{k}_1\sigma_1|\Sigma^{\rm HF}|\tilde{\boldsymbol{k}}_1\tilde{\sigma}_1\rangle = \sum_{\sigma_2\tilde{\sigma}_2}\int \mathrm{d}\boldsymbol{k}_2\mathrm{d}\tilde{\boldsymbol{k}}_2\langle \boldsymbol{k}_1\sigma_1\ \boldsymbol{k}_2\sigma_2|V|\tilde{\boldsymbol{k}}_1\tilde{\sigma}_1\ \tilde{\boldsymbol{k}}_2\tilde{\sigma}_2\rangle\langle \boldsymbol{k}_2\sigma_2|n|\tilde{\boldsymbol{k}}_2\tilde{\sigma}_2\rangle, \tag{4.7}$$

where V is the microscopic nucleon-nucleon interaction depending on the initial and final individual momenta and spins. It represents a 6-dimensional integration that would be a numerically challenging calculation. The HF self-energy and the density matrix are one body operators that do not change total spin or total angular momentum, they both satisfy Eq.(4.3).

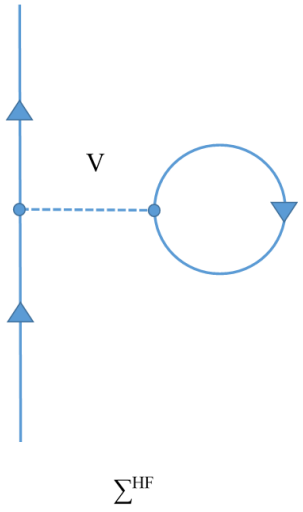

Figure 4.1: Illustration of the HF self-energy insertion.

4.2.2 Density Matrix elements in k-space

We need to explore possible simplifications or reductions of the matrix elements of the density matrix since they are part of the 6-dimensional integration to obtain the HF contribution

to the optical potential. The rotation invariance of the density matrix can be expressed as:

$$\begin{aligned}\langle \boldsymbol{q}\ {}^1/_2\ m_s'|n|\boldsymbol{k}\ {}^1/_2\ m_s\rangle &= \langle \boldsymbol{q}\ {}^1/_2\ m_s'|\hat{\mathcal{R}}^\dagger\hat{\mathcal{R}}n\hat{\mathcal{R}}^\dagger\hat{\mathcal{R}}|\boldsymbol{k}\ {}^1/_2\ m_s\rangle \\ &= {}_R\langle \boldsymbol{q}\ {}^1/_2\ m_s'|n|\boldsymbol{k}\ {}^1/_2\ m_s\rangle_R. \end{aligned} \tag{4.8}$$

To eliminate the dependence on the azimuth angles, 3 rotations are needed, the first two to put $\boldsymbol{k}$ along the $z-$axis, the third to put the momentum $\boldsymbol{q}$ in the $z''-x''$ plane. Before the rotation, the momentum components are $\boldsymbol{k}=(k,\theta,\phi)$ and $\boldsymbol{q}=(q,\theta_q,\phi_q)$. For the first two rotations to find a coordinate system in which $\boldsymbol{k}$ is along the $z-$axis, the matrix form of the rotations $\mathcal{A}$ can be expressed as:

$$\mathcal{A}=\begin{pmatrix}\cos\theta & 0 & -\sin\theta\\ 0 & 1 & 0\\ \sin\theta & 0 & \cos\theta\end{pmatrix}\begin{pmatrix}\cos\phi & \sin\phi & 0\\ -\sin\phi & \cos\phi & 0\\ 0 & 0 & 1\end{pmatrix} \tag{4.9}$$

Then the Cartesian components of $\boldsymbol{q}$ get transformed to:

$$\boldsymbol{q}''=\mathcal{A}\boldsymbol{q}, \tag{4.10}$$

which defines the angles θ_q'' and ϕ_q'', explicitly:

$$\theta_q''=\tan^{-1}\left(\frac{\sqrt{q_x''^2+q_y''^2}}{q_z''}\right),$$

and

$$\phi_q''=\tan^{-1}\left(\frac{q_y''}{q_x''}\right).$$

Concerning the angle ϕ_q'', it is the magnitude of the last rotation to ensure that both momenta are in the $z''-x''$ plane. One way of calculating this magnitude from the original angles is given by:

$$\phi_q'' = \tan^{-1}\left(\frac{\tan\phi + \tan\phi_q}{\tan\theta_q + \tan\theta_q\tan\phi - \sec\phi_q\tan\theta\sec\phi}\tan\theta_q\sec\theta\right). \tag{4.11}$$

Since these are rotation transformations, the magnitudes of the momenta and the angle between them remain unchanged and are defined by the given vectors already. On the other hand, the spin components change under rotations, in general, we need to keep track of the effect of the rotations on the spin projections simultaneously.

4.2.3 Effect of the rotation on the states

The full rotation transformation mentioned above is given by:

$$\hat{\mathcal{R}} = \hat{\mathcal{R}}^z_{-\phi_q''}\hat{\mathcal{R}}^y_{-\theta}\hat{\mathcal{R}}^z_{-\phi}.$$

Returning back to Eq.(4.8) we have:

$$\begin{aligned}
\langle \boldsymbol{q}\ {}^1\!/_2\ m_s'|n|\boldsymbol{k}\ {}^1\!/_2\ m_s\rangle &= \langle \boldsymbol{q}\ {}^1\!/_2\ m_s'|e^{-iS_z\phi}e^{-iS_y\theta}e^{-iS_z\phi_q''}ne^{iS_z\phi_q''}e^{iS_y\theta}e^{iS_z\phi}|\boldsymbol{k}\ {}^1\!/_2\ m_s\rangle \\
&= e^{i(m_s-m_s')\phi}\langle \boldsymbol{q}\ {}^1\!/_2\ m_s'|e^{-iS_y\theta}e^{-iS_z\phi_q''}ne^{iS_z\phi_q''}e^{iS_y\theta}|\boldsymbol{k}\ {}^1\!/_2\ m_s\rangle \\
&= e^{i(m_s-m_s')\phi}\sum_{\kappa\eta}e^{i(\eta-\kappa)\phi_q''}d^{1/2}_{m_s'\ \kappa}(\theta)d^{1/2}_{\eta\ m_s}(-\theta)\langle \boldsymbol{q}''\ {}^1\!/_2\ \kappa|n|\boldsymbol{k}''\ {}^1\!/_2\ \eta\rangle.
\end{aligned} \tag{4.12}$$

Here the spin 1/2 rotation matrix $d^{1/2}$ is given by:

$$d^{1/2}_{\mu\kappa}(\beta) = \begin{pmatrix} \cos(\beta/2) & -\sin(\beta/2) \\ \sin(\beta/2) & \cos(\beta/2) \end{pmatrix}. \tag{4.13}$$

To keep track of the conventions, the μ represents the column index while the κ is the row index.

For any given pair of one-particle states, $|\boldsymbol{q}\ {}^1/_2\ m_s'\rangle$, $|\boldsymbol{k}\ {}^1/_2\ m_s\rangle$, with momenta pointing in any arbitrary direction, one can calculate the matrix elements of the density matrix, by knowing the matrix elements $\langle \boldsymbol{q}''\ {}^1/_2\ \kappa|n|\boldsymbol{k}''\ {}^1/_2\ \eta\rangle$, which depend only on the magnitude of the momenta and the angle between them, say α. In terms of the components of the original coordinate system we have:

$$\cos\alpha = \sin(\theta)\sin(\theta_q)\cos(\phi-\phi_q) + \cos(\theta)\cos(\theta_q). \tag{4.14}$$

Additionally, the density matrix that we have is in a partial wave representation, we want to work in a vector basis representation, which implies the need to write the vector basis representation of the density matrix in terms of its matrix elements in partial waves.

4.2.4 Nucleon-Nucleon interaction in vector-basis

Due to the spherical symmetry of the 2-body scattering process between nucleons, the projection of the total angular momentum M_J is a good quantum number. The microscopic potential can be written as a Fourier series of the form:

$$\langle \boldsymbol{k} S M_s|V|\boldsymbol{k}' S M_S'\rangle = \sum_{M_J} V_{\underline{k},\underline{k}'}^{M_s M_S'}(\ M_J) e^{iM_J\Delta\phi}, \tag{4.15}$$

where $M_J = 0,\ \pm1,\ \pm2,\ldots,\ \underline{k} = (\ k,\ \theta_k)$ and $\underline{k}' = (\ k',\ \theta_k')$ and $\Delta\phi = \phi - \phi'$.

The nucleon-nucleon interaction is usually given in a partial-wave representation, as it is obtained from fitting phase shifts extracted from experimental data. The relationship between partial waves and vector-basis representation is obtained by writing the states in terms of

the partial waves basis:

$$|\boldsymbol{k}' S M_S' T\rangle = \sum_{\substack{JM_J \\ LM_L}} (LM_L SM_S|JM_J) Y^*_{LM_L}(\Omega_{k'}) |k\{LS\}JM_J T\rangle. \tag{4.16}$$

Note the difference from the one particle states shown in Eq.(4.2). The total momentum $\boldsymbol{K}$ must still be considered as $\boldsymbol{k}$ and $\boldsymbol{k'}$ refer to relative momenta. Inserting directly the matrix elements of the interactions assuming the form expressed in Eq.(4.15), the coefficients of the expansion are found by explicitly writing the spherical harmonics in terms of their definition:

$$\begin{aligned} V^{M_s M_s'}_{\underline{k},\underline{k}'}(\ M_J) = & \frac{(-1)^{(M_s+M_s')}}{4\pi} \sum_{J\ L\ L'} (L\ M_J - M_S\ S\ M_S|JM_J) \\ & \times (L'\ M_J - M_S'\ S\ M_S'|JM_J)\sqrt{(2L+1)(2L'+1)} \\ & \times \sqrt{\frac{(L-M_J+M_S)!}{(L+M_J-M_S)!}\frac{(L'-M_J+M_S')!}{(L'+M_J-M_S')!}} \\ & \times P_L^{M_J-M_S}(\cos(\theta_k)) P_{L'}^{M_J-M_S'}(\cos(\theta_k')) \\ & \times V_{kk'}^{LL'\ JST}, \end{aligned} \tag{4.17}$$

here $J = |M_J|,\ |M_J|+1,\ |M_J|+2,\ \ldots$, which in turn puts lower limits on L and L'. $V^{M_s M_s'}_{\underline{k},\underline{k}'}(\ M_J)$ also has the symmetry:

$$V^{M_s M_s'}_{\underline{k},\underline{k}'}(\ -M_J) = (-1)^{(M_s+M_s')} V^{-M_s-M_s'}_{\underline{k},\underline{k}'}(\ M_J).$$

Therefore, we find:

$$\langle \boldsymbol{k} S M_s|V|\boldsymbol{k}' S M_S'\rangle = V^{M_s M_s'}_{\underline{k},\underline{k}'}(0) + \sum_{M_J=1}^{\infty} \left(V^{M_s M_s'}_{\underline{k},\underline{k}'}(\ M_J) e^{iM_J\Delta\phi} + V^{M_s M_s'}_{\underline{k},\underline{k}'}(\ -M_J) e^{-iM_J\Delta\phi} \right). \tag{4.18}$$

The matrix elements of V are given in terms of relative momenta and total spin, however

the interaction appears in the uncoupled bases in the Hartree-Fock self-energy. To use the interaction in the uncoupled basis in terms of the individual quantum numbers and momenta we carry out the necessary transformations and find:

$$\langle \boldsymbol{k}_1\sigma_1\, \boldsymbol{k}_2\sigma_2|V|\tilde{\boldsymbol{k}}_1\tilde{\sigma}_1\, \tilde{\boldsymbol{k}}_2\tilde{\sigma}_2\rangle = \sum_{SM_SM'_S} (s_1m_1s_2m_2|SM_S)(\tilde{s}_1\tilde{m}_1\tilde{s}_2\tilde{m}_2|SM'_S)\langle \boldsymbol{k}SM_s|V|\boldsymbol{k}'SM'_S\rangle\delta_{\boldsymbol{KK}'}, \tag{4.19}$$

the relative momentum and total momentum are given by:

$$\boldsymbol{k} = \frac{\boldsymbol{k}_1 - \boldsymbol{k}_2}{2},\ \boldsymbol{k}' = \frac{\tilde{\boldsymbol{k}}_1 - \tilde{\boldsymbol{k}}_2}{2} \tag{4.20}$$

and

$$\boldsymbol{K} = \boldsymbol{k}_1 + \boldsymbol{k}_2. \tag{4.21}$$

The Kronecker delta in Eq.(4.19) results from the conservation of total momentum of the bare NN interaction.

Finally, we can perform rotations on the relative momentum space to reduce the computing time of the full HF integral. We take advantage of the invariance of the NN interaction under spin rotations. The process is almost identical to the one discussed above for the density matrix, however here the total spin is either 0 or 1. For $S = 1$, we have:

$$\langle \boldsymbol{k}SM_s|V|\boldsymbol{k}'SM'_S\rangle = e^{i(M'_s-M_s)\phi'_k}\sum_{\eta_s\eta'_s} e^{i(\eta'_s-\eta_s)\phi''_k} d^1_{M_s\eta_s}(\theta'_k) d^1_{\eta'_sM'_s}(-\theta'_k)\langle \boldsymbol{k}''S\eta_s|V|\boldsymbol{k}'''S\eta'_S\rangle, \tag{4.22}$$

where the $S = 1$ rotation matrix d^1 is given by:

$$d^1_{\mu\kappa}(\beta) = \begin{pmatrix} \frac{1+\cos(\beta)}{2} & -\frac{\sin(\beta)}{\sqrt{2}} & \frac{1-\cos(\beta)}{2} \\ \frac{\sin(\beta)}{\sqrt{2}} & \cos(\beta) & -\frac{\sin(\beta)}{\sqrt{2}} \\ \frac{1-\cos(\beta)}{2} & \frac{\sin(\beta)}{\sqrt{2}} & \frac{1+\cos(\beta)}{2} \end{pmatrix}. \tag{4.23}$$

The conventions are again that μ is the column index while the κ is the row index. Therefore, the matrix elements $\langle \boldsymbol{k} S M_s | V | \boldsymbol{k}' S M_S' \rangle$ can be calculated in terms of only 3 variables, the magnitude of the momenta $\boldsymbol{k}$ and $\boldsymbol{k}'$, and the angle between them.

4.3 Simplify the HF integration

With the above preparation, Eq.(4.7) can be written as:

$$\begin{aligned}\langle \boldsymbol{k}_1 \sigma_1 | \Sigma^{\mathrm{HF}} | \tilde{\boldsymbol{k}}_1 \tilde{\sigma}_1 \rangle = \sum_{\sigma_2 \ \tilde{\sigma}_2} \sum_{S M_S M_S'} \int \mathrm{d}\boldsymbol{k}_2 \mathrm{d}\tilde{\boldsymbol{k}}_2 (s_1 \ m_1 \ s_2 \ m_2 | S M_S)(\tilde{s}_1 \ \tilde{m}_1 \ \tilde{s}_2 \ \tilde{m}_2 | S M_S') \\ \times \langle \boldsymbol{k} S M_s | V | \boldsymbol{k}' S M_S' \rangle \delta_{\boldsymbol{K}\boldsymbol{K}'} \langle \boldsymbol{k}_2 \sigma_2 | n | \tilde{\boldsymbol{k}}_2 \tilde{\sigma}_2 \rangle,\end{aligned} \tag{4.24}$$

where the matrix elements of the interaction are in terms of relative and total momentum respectively, given in Eq.(4.20) and Eq.(4.21). The Kronecker delta $\delta_{\boldsymbol{K}\boldsymbol{K}'}$ in Eq.(4.24) therefore cancels out one integration variable leading to

$$\boldsymbol{K} = \boldsymbol{k}_1 + \boldsymbol{k}_2 = \boldsymbol{K}' = \tilde{\boldsymbol{k}}_1 + \tilde{\boldsymbol{k}}_2, \tag{4.25}$$

and therefore:

$$\tilde{\boldsymbol{k}}_2 = \boldsymbol{k}_2 + (\boldsymbol{k}_1 - \tilde{\boldsymbol{k}}_1). \tag{4.26}$$

The momenta associated to the external legs of the self energy are given by:

$$\begin{aligned}\tilde{\boldsymbol{k}}_1 &= (\tilde{k}_1 \ 0 \ 0), \\ \boldsymbol{k}_1 &= (k_1 \ \theta_1 \ 0).\end{aligned} \tag{4.27}$$

Rewriting Eq.(4.20) slightly yields:

$$\boldsymbol{k}_2 = \boldsymbol{k}_1 - 2\boldsymbol{k} \quad \text{and} \quad \tilde{\boldsymbol{k}}_2 = \tilde{\boldsymbol{k}}_1 - 2\boldsymbol{k}'. \tag{4.28}$$

The $\boldsymbol{k}'$ will be replaced by the other variables as follows:

$$\boldsymbol{k}' = \boldsymbol{k} - (\boldsymbol{k}_1 - \tilde{\boldsymbol{k}}_1). \tag{4.29}$$

For simplicity, the integration variables in Eq.(4.24) will change from individual to the relative momentum variables using:

$$\mathrm{d}\boldsymbol{k}_2 = -8\mathrm{d}\boldsymbol{k}. \tag{4.30}$$

The minus sign here will be taken care of implicitly by rearrange the integration space.

The total spin projection summation can be performed explicitly, since they are restricted on the basis of addition of angular momentum, and yields:

$$\begin{aligned}\langle \boldsymbol{k}_1\sigma_1|\Sigma^{\mathrm{HF}}|\tilde{\boldsymbol{k}}_1\tilde{\sigma}_1\rangle = &\sum_{\substack{m_2\tilde{m}_2\\ S}} (1/2\ m_1\ 1/2\ m_2|S\ m_1+m_2)(1/2\ \tilde{m}_1\ 1/2\ \tilde{m}_2|S\ \tilde{m}_1+\tilde{m}_2)\\ &\times 8\int \mathrm{d}\boldsymbol{k} V^{(m_1+m_2)\ \ (\tilde{m}_1+\tilde{m}_2)}_{\boldsymbol{k}\ \ \boldsymbol{k}-(\boldsymbol{k}_1-\tilde{\boldsymbol{k}}_1)} \langle (\boldsymbol{k}_1-2\boldsymbol{k})\ m_2|n|(\tilde{\boldsymbol{k}}_1-2\boldsymbol{k}')\ \tilde{m}_2\rangle.\end{aligned} \tag{4.31}$$

For completeness let us write the full Hartree-Fock term including the rotations performed on the density matrices:

$$\begin{aligned}\langle \boldsymbol{k}_1\sigma_1|\Sigma^{\mathrm{HF}}|\tilde{\boldsymbol{k}}_1\tilde{\sigma}_1\rangle = &\sum_{\substack{m_2\tilde{m}_2\\ S}} (1/2\ m_1\ 1/2\ m_2|S\ m_1+m_2)(1/2\ \tilde{m}_1\ 1/2\ \tilde{m}_2|S\ \tilde{m}_1+\tilde{m}_2)\\ &\times 8\int \mathrm{d}\boldsymbol{k}\ V^{(m_1+m_2)\ \ (\tilde{m}_1+\tilde{m}_2)}_{\boldsymbol{k}\ \ \boldsymbol{k}-(\boldsymbol{k}_1-\tilde{\boldsymbol{k}}_1)} e^{i(\tilde{m}_2-m_2)\tilde{\phi}_2}\\ &\times \sum_{\kappa\eta} e^{i(\eta-\kappa)\phi_2''} d^{1/2}_{m_2\ \kappa}(\tilde{\theta}_2) d^{1/2}_{\eta\ \tilde{m}_2}(-\tilde{\theta}_2) \langle (\boldsymbol{k}_1-2\boldsymbol{k})''\ \kappa|n|(\tilde{\boldsymbol{k}}_1-2\boldsymbol{k}')''\eta\rangle,\end{aligned} \tag{4.32}$$

where the two-body interaction part is given by Eq.(4.22). The double primed momenta are the momenta rotated as described before. Hence, one only needs to calculate the magnitudes of $(\boldsymbol{k}_1 - 2\boldsymbol{k})$, $(\tilde{\boldsymbol{k}}_1 - 2\boldsymbol{k}')$ and the angle between them, since the rotations do not change these quantities.

The summation over the total spin has two contributions $S = 0$ and $S = 1$ and they can be considered separately. In the former, $M_S = 0$ and $M'_S = 0$ therefore the integrals reduce to:

$$\begin{aligned}\langle \boldsymbol{k}_1\sigma_1|\Sigma^{\rm HF}_{S=0}|\tilde{\boldsymbol{k}}_1\tilde{\sigma}_1\rangle = &({}^1\!/_2\ m_1\ {}^1\!/_2\ -m_1|00)({}^1\!/_2\ \tilde{m}_1\ {}^1\!/_2\ -\tilde{m}_1|00)\\ &\times 8\int \mathrm{d}\boldsymbol{k} V^{00}_{\boldsymbol{k}\ \boldsymbol{k}-(\boldsymbol{k}_1-\tilde{\boldsymbol{k}}_1)} e^{i(m_1-\tilde{m}_1)\tilde{\phi}_2}\\ &\times \sum_{\kappa\eta} e^{i(\eta-\kappa)\phi''_2} d^{1/2}_{-m_1\ \kappa}(\tilde{\theta}_2) d^{1/2}_{\eta\ -\tilde{m}_1}(-\tilde{\theta}_2)\langle (\boldsymbol{k}_1-2\boldsymbol{k})''\ \kappa|n|(\tilde{\boldsymbol{k}}_1-2\boldsymbol{k}')''\ \eta\rangle\end{aligned} \tag{4.33}$$

For the contribution from $S = 1$, we have:

$$M_S\ \&\ M'_S = \begin{cases} 1 \\ 0 \\ -1 \end{cases} \tag{4.34}$$

so that for the triplet contribution, we obtain

$$\begin{aligned}\langle \boldsymbol{k}_1\sigma_1|\Sigma^{\rm HF}_{S=1}|\tilde{\boldsymbol{k}}_1\tilde{\sigma}_1\rangle = &\sum_{\substack{m_2\tilde{m}_2\\ S}} (1/2\ m_1\ 1/2\ m_2|S\ m_1+m_2)(1/2\ \tilde{m}_1\ 1/2\ \tilde{m}_2|S\ \tilde{m}_1+\tilde{m}_2)\\ &\times 8\int \mathrm{d}\boldsymbol{k} V^{(m_1+m_2)\ (\tilde{m}_1+\tilde{m}_2)}_{\mathbf{k}\ \mathbf{k}-(\mathbf{k_1}-\tilde{\mathbf{k}}_\mathbf{1})} e^{i(\tilde{m}_2-m_2)\tilde{\phi}_2}\\ &\times \sum_{\kappa\eta} e^{i(\eta-\kappa)\phi''_2} d^{1/2}_{m_2\ \kappa}(\tilde{\theta}_2) d^{1/2}_{\eta\ \tilde{m}_2}(-\tilde{\theta}_2)\langle (\boldsymbol{k}_1-2\boldsymbol{k})''\ \kappa|n|(\tilde{\boldsymbol{k}}_1-2\boldsymbol{k}')''\ \eta\rangle.\end{aligned} \tag{4.35}$$

The total HF term then reads:

$$\langle \boldsymbol{k}_1\sigma_1|\Sigma^{\rm HF}|\tilde{\boldsymbol{k}}_1\tilde{\sigma}_1\rangle = \langle \boldsymbol{k}_1\sigma_1|\Sigma^{\rm HF}_{S=0}|\tilde{\boldsymbol{k}}_1\tilde{\sigma}_1\rangle + \langle \boldsymbol{k}_1\sigma_1|\Sigma^{\rm HF}_{S=1}|\tilde{\boldsymbol{k}}_1\tilde{\sigma}_1\rangle \tag{4.36}$$

4.3.1 Including isospin dependence

If the differences between neutrons and protons need to be investigated for $N \neq Z$, an additional parameter the isospin should be treated properly. More practically, the isospin symmetry for $N = Z$ nucleus can also be employed to test the numerical program. Equation (4.24) when updated to include isospin dependence, yields:

$$\begin{aligned}\langle \boldsymbol{k}_1\sigma_1^s\sigma_1^t|\Sigma^{\rm HF}|\tilde{\boldsymbol{k}}_1\tilde{\sigma}_1^s\tilde{\sigma}_1^t\rangle = &\sum_{\substack{\sigma_2^s\sigma_2^t\\ \tilde{\sigma}_2^s\tilde{\sigma}_2^t}}\sum_{\substack{SM_SM_S'\\ TM_TM_T'}}\int \mathrm{d}\boldsymbol{k}_2\mathrm{d}\tilde{\boldsymbol{k}}_2\\ &\times (s_1\ m_1^s\ s_2\ m_2^s|SM_S)(\tilde{s}_1\ \tilde{m}_1^s\ \tilde{s}_2\ \tilde{m}_2^s|SM_S')\\ &\times (t_1\ m_1^t\ t_2\ m_2^t|TM_T)(\tilde{t}_1\ \tilde{m}_1^t\ \tilde{t}_2\ \tilde{m}_2^t|TM_T')\\ &\times \langle \boldsymbol{k}SM_STM_T|V|\boldsymbol{k}'SM_S'TM_T'\rangle\delta_{\boldsymbol{K}\boldsymbol{K}'}\\ &\times \langle \boldsymbol{k}_2\sigma_2^s\sigma_2^t|n|\tilde{\boldsymbol{k}}_2\tilde{\sigma}_2^s\tilde{\sigma}_2^t\rangle.\end{aligned} \tag{4.37}$$

The corresponding version for Eq.(4.32) reads:

$$\begin{aligned}\langle \boldsymbol{k}_1\sigma_1^s|\Sigma^{\rm HF}_{\sigma_1^t}|\tilde{\boldsymbol{k}}_1\tilde{\sigma}_1^s\rangle = &\sum_{\substack{m_2^s\tilde{m}_2^s\\ S}}\sum_{\substack{m_2^t\\ T}}(1/2\ m_1^s\ 1/2\ m_2^s|S\ m_1^s+m_2^s)(1/2\ \tilde{m}_1^s\ 1/2\ \tilde{m}_2^s|S\ \tilde{m}_1^s+\tilde{m}_2^s)\\ &\times (1/2\ m_1^t\ 1/2\ m_2^t|T\ m_1^t+m_2^t)(1/2\ m_1^t\ 1/2\ m_2^t|T\ m_1^t+m_2^t)\\ &\times 8\int \mathrm{d}\boldsymbol{k}\ V^{(m_1^s+m_2^s)\ (\tilde{m}_1^s+\tilde{m}_2^s)\ (m_1^t+m_2^t)}_{\boldsymbol{k}\ \boldsymbol{k}-(\boldsymbol{k}_1-\tilde{\boldsymbol{k}}_1)}e^{i(\tilde{m}_2-m_2)\tilde{\phi}_2}\\ &\times \sum_{\kappa\eta}e^{i(\eta-\kappa)\phi_2''}d^{1/2}_{m_2^s\ \kappa}(\tilde{\theta}_2)d^{1/2}_{\eta\ \tilde{m}_2^s}(-\tilde{\theta}_2)\langle(\boldsymbol{k}_1-2\boldsymbol{k})''\ \kappa|n_{\sigma_2^t}|(\tilde{\boldsymbol{k}}_1-2\boldsymbol{k}')''\eta\rangle.\end{aligned} \tag{4.38}$$

4.3.2 Results and discussions for HF self-energy

A symmetry analysis will help to validate the numerical procedure. We know the HF self-energy $\langle \boldsymbol{k}_1 \sigma_1^s | \Sigma^{\rm HF}_{\sigma_1^t} | \tilde{\boldsymbol{k}}_1 \tilde{\sigma}_1^s \rangle$ for ^{40}Ca is a purely real object, and it is not sensitive to isospin projection unless the density matrix is very different for neutrons and protons. The spin projection dependence has the following symmetry:

$$\langle \boldsymbol{k}_1 \ m_{s1} | \Sigma^{\rm HF}_{\sigma_1^t} | \tilde{\boldsymbol{k}}_1 \ \tilde{m}_{s1} \rangle = (-1)^{(1+m_{s1}+\tilde{m}_{s1})} \langle \boldsymbol{k}_1 \ \ -m_{s1} | \Sigma^{\rm HF}_{\sigma_1^t} | \tilde{\boldsymbol{k}}_1 \ \ -\tilde{m}_{s1} \rangle. \tag{4.39}$$

After all the symmetry properties are fulfilled numerically, a comparison with harmonic oscillator (HO) calculation is made in order to further validate the numerical procedure. We employ a density matrix and a HF results from a calculation with a HO basis using the bare interaction N3LO [4] for a specific nucleus, for example ^{16}O, ^{40}Ca, etc. The HO density matrix is first transformed to the vector $\boldsymbol{k}$ basis to employ in Eq.(4.38), then folded with the interaction matrix also in the vector $\boldsymbol{k}$ basis to generate the HF self-energy, a comparison is then made to the HF results from HO calculation as shown in Fig.(4.2). Diagonal matrix elements for spin projection "up-up" $\langle k \ m_{s1} = 1/2 | \Sigma^{\rm HF}_{pp} | k \ \tilde{m}_{s1} = 1/2 \rangle$ at angle $\theta = 15^\circ$ is plotted for the momentum range 0-5 fm^{-1}. Note for simplicity and as a convention issue, the angle is always assigned to the left $\boldsymbol{k}$ throughout the chapter unless further specified, while the right $\boldsymbol{k}$ is along the z-axis. The agreement is quite good considering the HO calculation introduces a cutoff of their interaction matrix.

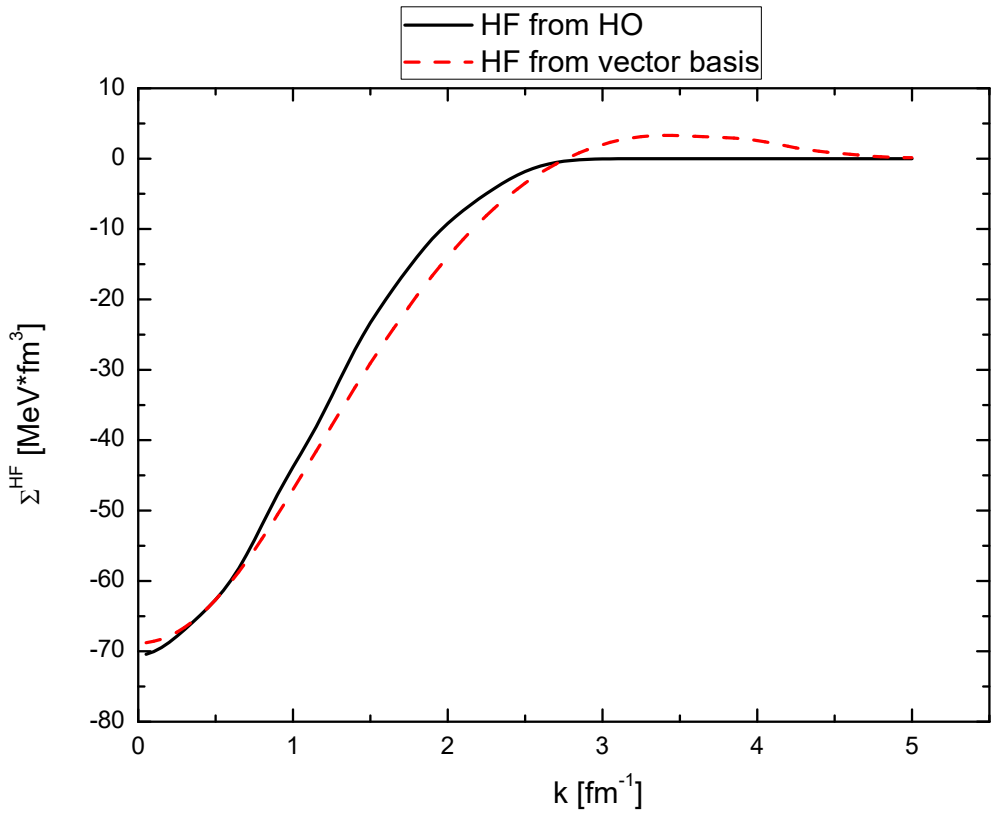

Figure 4.2: Diagonal matrix elements for spin projection "up-up" $\langle k\ m_{s1} = 1/2|\Sigma^{\rm HF}_{pp}|k\ \tilde{m}_{s1} = 1/2\rangle$ at angle $\theta = 15°$ is plotted for the momentum range 0-5 fm^{-1}. Solid black curve: HO calculation, dashed red curve: vector basis calculation.

Several plots are given to illustrate the properties of the HF self-energy. The diagonal matrix elements for spin projection "down-up" $\langle k\ m_{s1} = -1/2|\Sigma^{\rm HF}_{pp}|k\ \tilde{m}_{s1} = 1/2\rangle$ at angle $\theta = 15°$ is plotted for the momentum range 0-3 fm^{-1} as shown in Fig.(4.5). It is a much smaller term compare to $\langle k\ m_{s1} = 1/2|\Sigma^{\rm HF}_{pp}|k\ \tilde{m}_{s1} = 1/2\rangle$. The angle dependence is illustrated in Fig.(4.3). The matrix elements for $\langle k\ \theta\ m_{s1} = 1/2|\Sigma^{\rm HF}_{pp}|k\ \tilde{m}_{s1} = 1/2\rangle$ at $k = 1.0$ fm^{-1} is plotted for the angle range 0-180°.

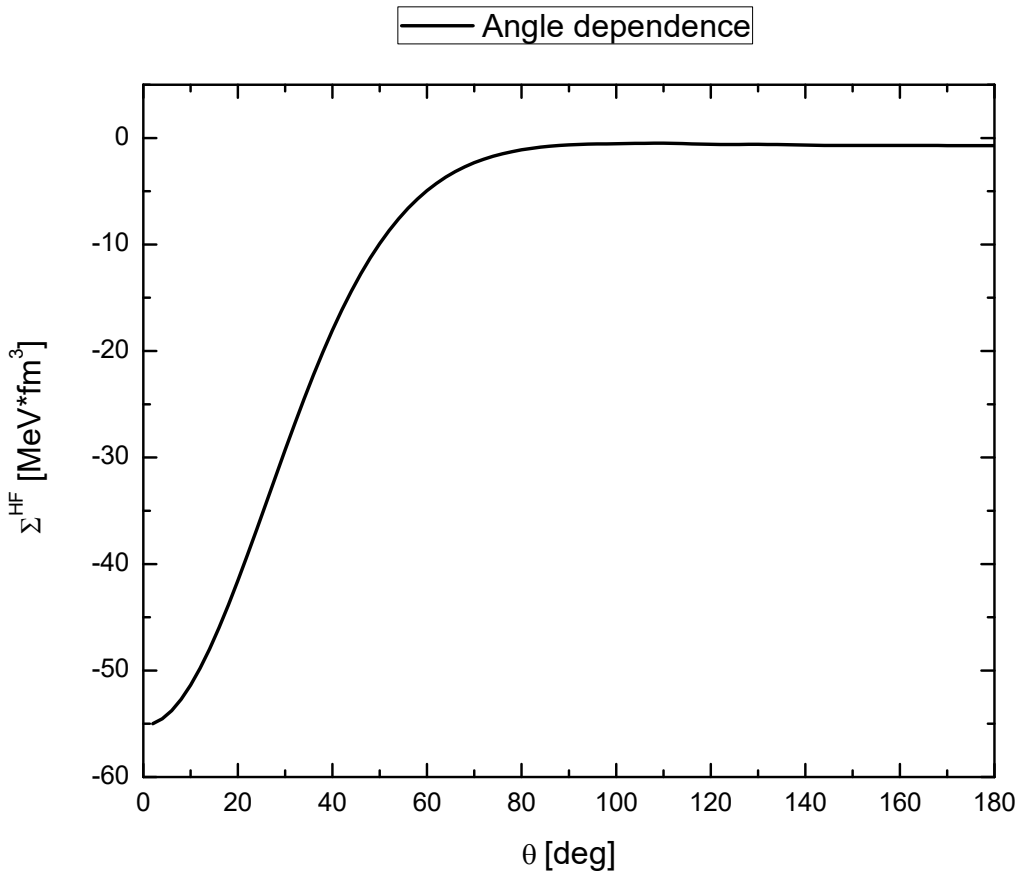

Figure 4.3: The matrix elements for $\langle k\ \theta\ m_{s1} = 1/2|\Sigma^{\rm HF}_{pp}|k\ \tilde{m}_{s1} = 1/2\rangle$ at $k = 1.0$ fm^{-1} is plotted for the angle range 0-180°.

In order to see the influence to the HF self-energy induce by a different density matrix, the DOM density matrix is also used in the calculation for comparison. As the DOM can generate a spectral function which has an energy dependence, we delay the detailed derivation and formulation until next section but only show the results in Fig.(4.4) and Fig.(4.5). As can be seen, the deviation of the HF self-energy from HO density matrix for spin projection "up-up" is small while for "down-up" is quite big reflecting most likely the restricted HO model space.

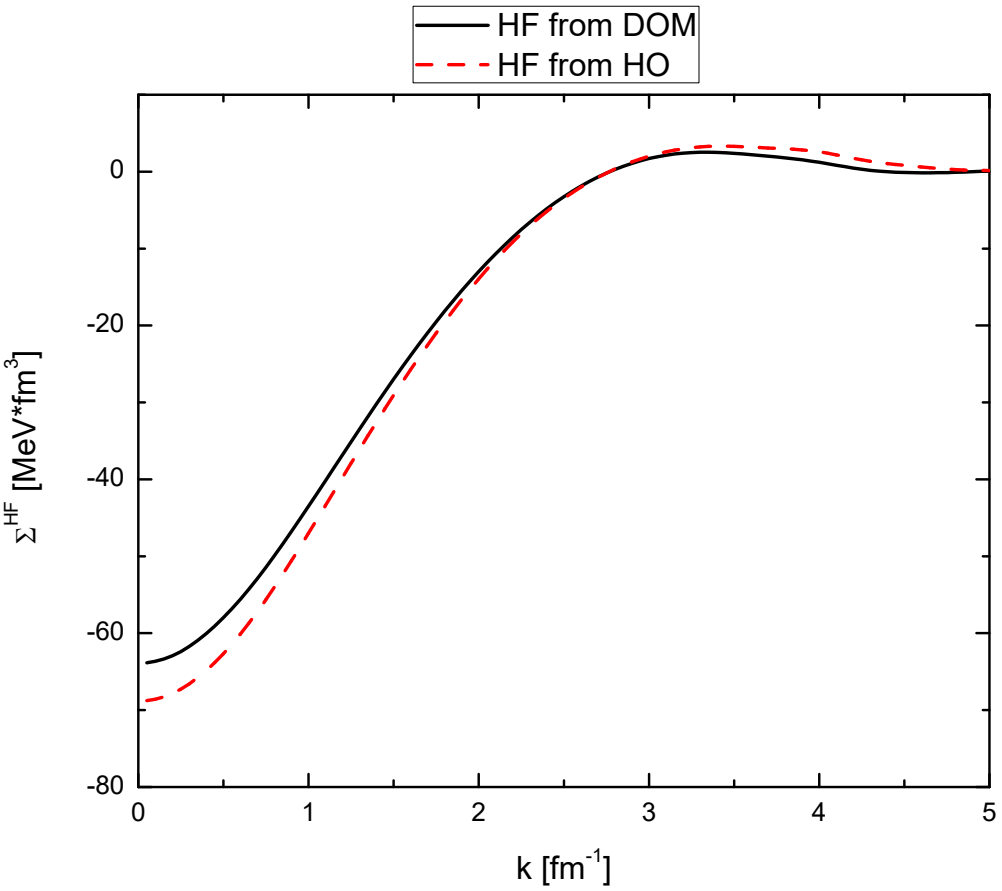

Figure 4.4: Diagonal matrix elements for $\langle k\ m_{s1} = 1/2|\Sigma^{\rm HF}_{pp}|k\ \tilde{m}_{s1} = 1/2\rangle$ at angle $\theta = 15°$ is plotted for the momentum range 0-5 fm^{-1}. Solid black curve: HF self-energy from DOM density matrix, dashed red curve: HF self-energy from HF density matrix restricted in HO basis.

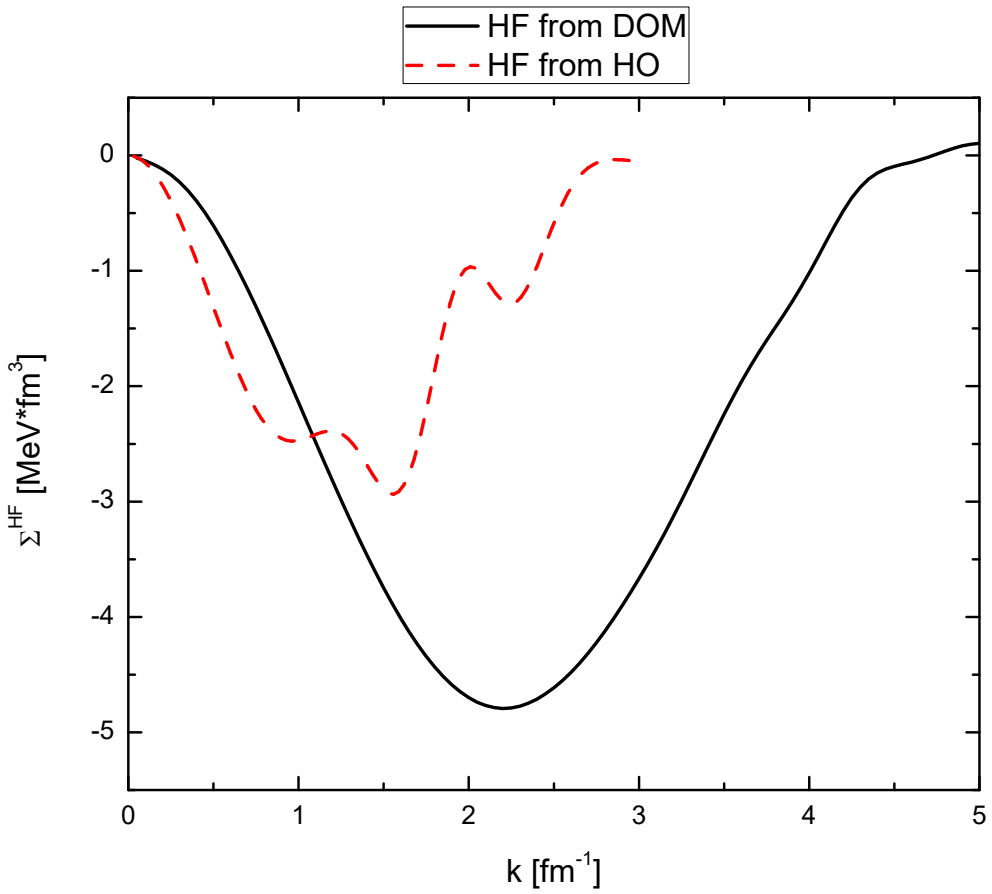

Figure 4.5: Diagonal matrix elements for $\langle k\ m_{s1} = -1/2|\Sigma^{\rm HF}_{pp}|k\ \tilde{m}_{s1} = 1/2\rangle$ at angle $\theta = 15°$ is plotted for the momentum range 0-5 fm^{-1}. Solid black curve: HF self-energy from DOM density matrix, dashed red curve: HF self-energy from HF density matrix restricted in HO basis.

4.4 Ladder self-energy

The next diagram contribution beyond the HF term is shown in the Fig.(4.6). The corresponding diagonal self-energy expressed in terms of the vertex function can be written down

directly following diagram rules [21], which generates:

$$\begin{aligned}\Sigma_{\Delta\Gamma}(\boldsymbol{k};E) = -i^2\frac{1}{2}\int\frac{\mathrm{d}E_1}{2\pi}\int\frac{\mathrm{d}E_2}{2\pi}\int\frac{\mathrm{d}^3q}{(2\pi)^3}\int\frac{\mathrm{d}^3k'}{(2\pi)^3}\frac{1}{\nu}\sum_{m_\alpha m_\beta m_\gamma m_\delta}\\ \times\langle\boldsymbol{k}m_\alpha(\boldsymbol{k}'-\boldsymbol{q}/2)m_\beta|V|(\boldsymbol{k}-\boldsymbol{q})m_\gamma(\boldsymbol{k}'+\boldsymbol{q}/2)m_\delta\rangle\\ \times G((\boldsymbol{k}-\boldsymbol{q});E-E_1)G((\boldsymbol{k}'+\boldsymbol{q}/2);E_1+E_2)G((\boldsymbol{k}'-\boldsymbol{q}/2);E_2)\\ \times\langle(\boldsymbol{k}-\boldsymbol{q})m_\gamma(\boldsymbol{k}'+\boldsymbol{q}/2)m_\delta|\Gamma(E,E_1,E_2)|\boldsymbol{k}m_\alpha(\boldsymbol{k}'-\boldsymbol{q}/2)m_\beta\rangle.\end{aligned} \tag{4.40}$$

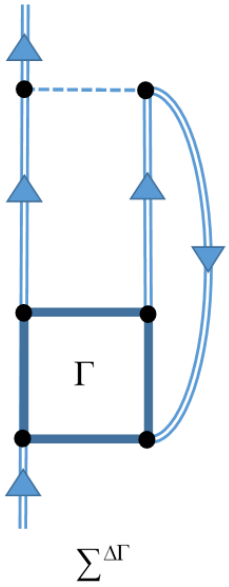

Figure 4.6: Illustration of higher order self-energy, double line means full propagator.

Replacing the vertex function Γ with bare interaction V reveal the second order diagram. The relevant summation of ladder diagrams for the vertex function is given by

$$\begin{aligned}&\langle\boldsymbol{k}m_\alpha m_{\alpha'}|\Gamma_{pphh}(\boldsymbol{K},E)|\boldsymbol{k}'m_\beta m_{\beta'}\rangle\\ &=\langle\boldsymbol{k}m_\alpha m_{\alpha'}|V|\boldsymbol{k}'m_\beta m_{\beta'}\rangle+\langle\boldsymbol{k}m_\alpha m_{\alpha'}|\Delta\Gamma_{pphh}(\boldsymbol{K},E)|\boldsymbol{k}'m_\beta m_{\beta'}\rangle\\ &=\langle\boldsymbol{k}m_\alpha m_{\alpha'}|V|\boldsymbol{k}'m_\beta m_{\beta'}\rangle+\frac{1}{2}\sum_{m_\gamma m_{\gamma'}}\int\frac{\mathrm{d}^3q}{(2\pi)^3}\langle\boldsymbol{k}m_\alpha m_{\alpha'}|V|\boldsymbol{k}'m_\gamma m_{\gamma'}\rangle\\ &\times G^f_{pphh}(\boldsymbol{K},\boldsymbol{q};E)\langle\boldsymbol{q}m_\gamma m_{\gamma'}|\Gamma_{pphh}(\boldsymbol{K},E)|\boldsymbol{k}'m_\beta m_{\beta'}\rangle\end{aligned} \tag{4.41}$$

where:

$$\begin{aligned}\boldsymbol{k} &= \frac{\boldsymbol{k}_1 - \boldsymbol{k}_2}{2},\\ \boldsymbol{k}' &= \frac{\tilde{\boldsymbol{k}}_1 - \tilde{\boldsymbol{k}}_2}{2},\\ \boldsymbol{K} &= \boldsymbol{k}_1 + \boldsymbol{k}_2 = \tilde{\boldsymbol{k}}_1 + \tilde{\boldsymbol{k}}_2.\end{aligned} \tag{4.42}$$

Now consider the second term in the right hand side of Eq.(4.41), where $\Delta\Gamma_{pphh} \equiv \Gamma_{pphh} - V = VG^f_{pphh}\Gamma_{pphh}$. Then inserting the Lehmann representation of G^f_{pphh}, we can write $\Delta\Gamma_{pphh}$ in the form of dispersion relation in vector basis as following:

$$\begin{aligned}\langle \boldsymbol{k}\sigma_1\sigma_2|\Delta\Gamma_{pphh}(\boldsymbol{K},E)|\boldsymbol{k}'\tilde{\sigma}_1\tilde{\sigma}_2\rangle &= -\frac{1}{\pi}\int_{2\epsilon_F}^{+\infty} \mathrm{d}E' \frac{\mathrm{Im}\langle \boldsymbol{k}\sigma_1\sigma_2|\Delta\Gamma_{pphh}(\boldsymbol{K},E')|\boldsymbol{k}'\tilde{\sigma}_1\tilde{\sigma}_2\rangle}{E - E' + i\eta}\\ &+ \frac{1}{\pi}\int_{-\infty}^{2\epsilon_F} \mathrm{d}E' \frac{\mathrm{Im}\langle \boldsymbol{k}\sigma_1\sigma_2|\Delta\Gamma_{pphh}(\boldsymbol{K},E')|\boldsymbol{k}'\tilde{\sigma}_1\tilde{\sigma}_2\rangle}{E - E' - i\eta}\\ &\equiv \langle \boldsymbol{k}\sigma_1\sigma_2|\Delta\Gamma_{\downarrow}(\boldsymbol{K},E)|\boldsymbol{k}'\tilde{\sigma}_1\tilde{\sigma}_2\rangle + \langle \boldsymbol{k}\sigma_1\sigma_2|\Delta\Gamma_{\uparrow}(\boldsymbol{K},E)|\boldsymbol{k}'\tilde{\sigma}_1\tilde{\sigma}_2\rangle.\end{aligned} \tag{4.43}$$

For simplicity σ here denote both spin and isospin. The arrows $\downarrow$ and $\uparrow$ indicate the corresponding parts of $\Delta\Gamma(\boldsymbol{K},E)$ has an energy pole in the lower and upper half plane. The higher order vertex function $\Delta\Gamma_{pphh}$ becomes the new building block of the self-energy, therefore Eq.(4.40) can be updated to:

$$\begin{aligned}\Sigma_{\Delta\Gamma}(\boldsymbol{k}_1\sigma_1, \tilde{\boldsymbol{k}}_1\tilde{\sigma}_1; E) = -\frac{i}{\nu}\sum_{\sigma_2\tilde{\sigma}_2}\int \mathrm{d}^3\boldsymbol{k}_2\mathrm{d}^3\tilde{\boldsymbol{k}}_2 \int \frac{\mathrm{d}E'}{2\pi} G(\boldsymbol{k}_2\sigma_2, \tilde{\boldsymbol{k}}_2\tilde{\sigma}_2; E')\\ \times \langle \boldsymbol{k}\sigma_1\sigma_2|\Delta\Gamma_{pphh}(\boldsymbol{K}, E+E')|\boldsymbol{k}'\tilde{\sigma}_1\tilde{\sigma}_2\rangle.\end{aligned} \tag{4.44}$$

The degeneracy factor is denoted by ν and should be included when the spin and isospin dependence is properly treated. Total momentum conservation as shown in Eq.(4.42) will cancel one of the two $\boldsymbol{k}_2$ integrals, resulting in only a 4D integration.

The propagator G can be expressed in terms of the spectral functions as follows:

$$G(\boldsymbol{k}_2\sigma_2, \tilde{\boldsymbol{k}}_2\tilde{\sigma}_2; E) = \int_{\epsilon_F}^{+\infty} \mathrm{d}E' \frac{S_p(\boldsymbol{k}_2\sigma_2, \tilde{\boldsymbol{k}}_2\tilde{\sigma}_2; E')}{E - E' + i\eta} + \int_{-\infty}^{\epsilon_F} \mathrm{d}E' \frac{S_h(\boldsymbol{k}_2\sigma_2, \tilde{\boldsymbol{k}}_2\tilde{\boldsymbol{\sigma}}_2; E')}{E - E' - i\eta}. \tag{4.45}$$

Inserting the above expression into Eq.(4.44) yields:

$$\begin{aligned}
\Sigma_{\Delta\Gamma}(\boldsymbol{k}_1\sigma_1, \tilde{\boldsymbol{k}}_1\tilde{\sigma}_1; E) = & \sum_{\sigma_2\tilde{\sigma}_2} \int \mathrm{d}^3\boldsymbol{k}_2 \mathrm{d}^3\tilde{\boldsymbol{k}}_2 \int_{-\infty}^{\epsilon_F} \mathrm{d}E' \langle \boldsymbol{k}\sigma_1\sigma_2 | \Delta\Gamma_{\downarrow}(\boldsymbol{K}, E + E') | \boldsymbol{k}'\tilde{\sigma}_1\tilde{\sigma}_2 \rangle \\
& \times S_h(\boldsymbol{k}_2\sigma_2, \tilde{\boldsymbol{k}}_2\tilde{\sigma}_2; E') \\
& - \sum_{\sigma_2\tilde{\sigma}_2} \int \mathrm{d}^3\boldsymbol{k}_2 \mathrm{d}^3\tilde{\boldsymbol{k}}_2 \int_{\epsilon_F}^{+\infty} \mathrm{d}E' \langle \boldsymbol{k}\sigma_1\sigma_2 | \Delta\Gamma_{\uparrow}(\boldsymbol{K}, E + E') | \boldsymbol{k}'\tilde{\sigma}_1\tilde{\sigma}_2 \rangle \\
& \times S_p(\boldsymbol{k}_2\sigma_2, \tilde{\boldsymbol{k}}_2\tilde{\sigma}_2; E') \\
& \equiv \Delta\Sigma_{\downarrow}(\boldsymbol{k}_1\sigma_1, \tilde{\boldsymbol{k}}_1\tilde{\sigma}_1; E) + \Delta\Sigma_{\uparrow}(\boldsymbol{k}_1\sigma_1, \tilde{\boldsymbol{k}}_1\tilde{\sigma}_1; E).
\end{aligned} \tag{4.46}$$

The self-energy therefore consists of three terms:

$$\Sigma(\boldsymbol{k}_1\sigma_1, \tilde{\boldsymbol{k}}_1\tilde{\sigma}_1; E) = \Sigma_{HF}(\boldsymbol{k}_1\sigma_1, \tilde{\boldsymbol{k}}_1\tilde{\sigma}_1) + \Delta\Sigma_{\downarrow}(\boldsymbol{k}_1\sigma_1, \tilde{\boldsymbol{k}}_1\tilde{\sigma}_1; E) + \Delta\Sigma_{\uparrow}(\boldsymbol{k}_1\sigma_1, \tilde{\boldsymbol{k}}_1\tilde{\sigma}_1; E). \tag{4.47}$$

The first HF term which is energy independent has been calculated in the previous section. The second term will be considered in the following. The third term should be straightforward when low-energy and bound-state information is treated at a later stage.

4.4.1 $\mathcal{T}-$matrix and $\mathcal{R}-$matrix

The ladder vertex function Γ shown in Eq.(4.41) can be solved in the partial wave basis by matrix inversion. We relabel the vertex function Γ as the $\mathcal{T}-$matrix which fulfills the

following Dyson like equation:

$$\langle k|\mathcal{T}(\omega)|k'\rangle = \langle k|V|k'\rangle + \int \mathrm{d}k''k''^2\langle k|V|k''\rangle \frac{1}{\omega - \frac{\hbar^2 k''^2}{2m} + i\eta}\langle k''|\mathcal{T}|k'\rangle, \tag{4.48}$$

where angular momentum labels are suppressed for simplicity. Note that the difference between the contributions from Γ and $\Delta\Gamma$, the HF self-energy, is included automatically in the $\mathcal{T}\times\rho$ calculation. Solving the above equation with the real part of the propagator only generates the $\mathcal{R}-$matrix as follows:

$$\langle k|R(\omega)|k'\rangle = \langle k|V|k'\rangle + \mathcal{P}\int dk''k''^2\langle k|V|k''\rangle \frac{1}{\omega - \frac{\hbar^2 k''^2}{2m}}\langle k''|R(\omega)|k'\rangle. \tag{4.49}$$

The next step, to incorporate the imaginary part of the propagator is to construct the $\mathcal{T}-$matrix by the following equation:

$$\langle k|T(\omega)|k'\rangle = \langle k|R(\omega)|k'\rangle + \int dk''k''^2\langle k|R(\omega)|k''\rangle(-i\pi\delta(\omega - \frac{\hbar^2 k''^2}{2m}))\langle k''|T(\omega)|k'\rangle. \tag{4.50}$$

Properly treating the coefficient of the δ function yields:

$$\langle k|T(\omega)|k'\rangle = \langle k|R(\omega)|k'\rangle - \int dk''k''^2\langle k|R(\omega)|k''\rangle i\pi\frac{1}{\frac{\hbar^2 k''}{m}}\delta(k''-k_0))\langle k''|T(\omega)|k'\rangle, \tag{4.51}$$

where k_0 is the momentum correspond to the energy ω. The delta function will eliminate the integration, resulting in a simpler form as matrix multiplication:

$$\langle k|T(\omega)|k'\rangle = \langle k|R(\omega)|k'\rangle - i\frac{\pi k_0 m}{\hbar^2}\langle k|R(\omega)|k_0\rangle\langle k_0|T(\omega)|k'\rangle. \tag{4.52}$$

The special component $\langle k_0|T(\omega)|k'\rangle$ can be calculated by setting the left k to be k_0, which yields:

$$\langle k_0|T(\omega)|k'\rangle = \langle k_0|R(\omega)|k'\rangle - i\frac{\pi k_0 m}{\hbar^2}\langle k_0|R(\omega)|k_0\rangle\langle k_0|T(\omega)|k'\rangle. \tag{4.53}$$

Solving the above linear equation, one can construct $\langle k_0|\mathcal{T}|k'\rangle$ for the partial wave basis.

In the vector basis, the single particle spins s couple to the total spin S. Additionally, the angle dependence θ should be introduced. Some modifications of Eq.(4.48) are then necessary. The $\mathcal{T}-$matrix now is an object very much like the bare two-body interaction but has an energy dependence as shown in the following:

$$\begin{aligned}\langle k\theta M_S|\mathcal{T}(\omega)|k'\theta' M'_S\rangle &= \langle k\theta M_S|V|k'\theta' M'_S\rangle \\ &+ \sum_{M''_S}\int dk'' dcos\theta'' k''^2 \langle k\theta M_S|V|k''\theta'' M''_S\rangle \frac{1}{\omega - \frac{\hbar^2 k''^2}{2m} + i\eta} \\ &\times \langle k''\theta'' M''_S|\mathcal{T}(\omega)|k'\theta' M'_S\rangle.\end{aligned} \tag{4.54}$$

Similar modification should apply to construct $\mathcal{R}-$matrix in vector basis. Note that Haftel and Tabakin method [90] has been employed implicitly to avoid the poles in the $\mathcal{R}-$matrix:

$$\begin{aligned}\langle k\theta M_S|R(\omega)|k'\theta' M'_S\rangle &= \langle k\theta M_S|V|k'\theta' M'_S\rangle \\ &+ \mathcal{P}\sum_{M''_S}\int dk'' dcos\theta'' k''^2 \langle k\theta M_S|V|k''\theta'' M''_S\rangle \frac{1}{\omega - \frac{\hbar^2 k''^2}{2m}} \\ &\times \langle k''\theta'' M''_S|R(\omega)|k'\theta' M'_S\rangle.\end{aligned} \tag{4.55}$$

Using the method discussed for the partial wave basis, the $\mathcal{T}-$matrix in the vector basis can

be constructed by the following two steps:

$$\begin{aligned}\langle k\theta M_S|\mathcal{T}(\omega)|k'\theta' M'_S\rangle &= \langle k\theta M_S|R(\omega)|k'\theta' M'_S\rangle \\ &- i\frac{\pi k_0 m}{\hbar^2}\sum_{M''_S}\int dcos\theta''\langle k\theta M_S|R(\omega)|k_0\theta'' M''_S\rangle \\ &\times \langle k_0\theta'' M''_S|\mathcal{T}(\omega)|k'\theta' M'_S\rangle,\end{aligned} \tag{4.56}$$

$$\begin{aligned}\langle k_o\theta M_S|\mathcal{T}(\omega)|k'\theta' M'_S\rangle &= \langle k_0\theta M_S|R(\omega)|k'\theta' M'_S\rangle \\ &- i\frac{\pi k_0 m}{\hbar^2}\sum_{M''_S}\int dcos\theta''\langle k_0\theta M_S|R(\omega)|k_0\theta'' M''_S\rangle \\ &\times \langle k_0\theta'' M''_S|\mathcal{T}(\omega)|k'\theta' M'_S\rangle.\end{aligned} \tag{4.57}$$

Solving the above equation requires a matrix inversion of dimension $n_\theta \times n_\theta$, where n_θ is the number of the mesh points for the angle θ. The object $\langle k_o\theta M_S|\mathcal{T}(\omega)|k'\theta' M'_S\rangle$ is a $n_\theta \times (n_\theta * n_k)$ matrix for total spin $S = 0$ case, while a $3n_\theta \times 3(n_\theta * n_k)$ matrix for total spin $S = 1$ case. To construct the matrix $\langle k\theta M_S|\mathcal{T}(\omega)|k'\theta' M'_S\rangle$ which is in the scale of $3(n_\theta * n_k) \times 3(n_\theta * n_k)$, only matrix multiplication is needed.

4.4.2 Inputs from the DOM

If SCGF methods are employed, the resulting self-energy will not depend on the input spectral functions, which is required in the formalism we discuss above. In order to test the usefulness of the self-energy generated by Eq.(4.46) without a full SCGF implementation, a realistic input of spectral functions will provide a useful procedure. A good candidate is available in terms of the DOM spectral functions. We will apply one more simplification and avoid the 4D integration to limit computer resources. We model the spectral functions obtained from the DOM by delta functions which preserve the information indicating the location of the peak and also the spectral strength. The advantage is that the delta functions

eliminate one of the integrations and also avoid the deuteron pole of the $\mathcal{T}-$ matrix. The latter pole will in any case disappear when a self-consistent treatment is implemented. In the partial wave basis, the spectral function matrix is simply a combination of delta functions and wave-functions.

$$S^n_{lj}(k,k';E) = N^n_{lj}\delta(E - \frac{\epsilon^n_{lj}}{N^n_{lj}})\phi^n_{lj}(k)\phi^n_{lj}(k'), \tag{4.58}$$

where the ϵ^n_{lj} indicates the position of the *sp* partial wave energy peak and N^n_{lj} indicates the corresponding particle number strength. The equation for calculating the ladder self-energy is then almost identical to the HF case, which simplifies the numerical procedure considerably as shown below:

$$\begin{aligned}\Delta\Sigma^{m_1^t}_{\downarrow}(\boldsymbol{k}_1 m_1^s, \tilde{\boldsymbol{k}}_1 \tilde{m}_1^s; E) = &\sum_{m_2^s \tilde{m}_2^s m_2^t} \sum_{SM_S M'_S} \int \mathrm{d}^3\boldsymbol{k}_2 \mathrm{d}^3\tilde{\boldsymbol{k}}_2 \int_{-\infty}^{\epsilon_F} \mathrm{d}E' \\ &\times (s_1 m_1^s s_2 m_2^s | SM_S)(\tilde{s}_1 \tilde{m}_1^s \tilde{s}_2 \tilde{m}_2^s | SM'_S) \\ &\times (t_1 m_1^t t_2 m_2^t | TM_T)(t_1 m_1^t t_2 m_2^t | TM_T) \\ &\times \langle \boldsymbol{k} M_S | \Delta\Gamma^{STM_T}_{\downarrow}(\boldsymbol{K}, E+E') | \boldsymbol{k}' M'_S \rangle S_h^{m_2^t}(\boldsymbol{k}_2 m_2^s, \tilde{\boldsymbol{k}}_2 \tilde{m}_2^s; E'). \end{aligned} \tag{4.59}$$

For reference, the key parameters of the spectral functions used in the calculation are listed in the table 4.1. Note that the energies ϵ_{nlj} are obtained from the energy-weighted strength and therefore spin-orbit partners have larger energy separations. We checked that the resulting point densities represent a good approximation to the complete DOM results.

	Proton		Neutron	
n l j	ε_{nlj} [MeV]	N_{nlj}	ε_{nlj} [MeV]	N_{nlj}
0 $s_{1/2}$	-49.3961	0.928813	-56.7369	0.925109
1 $s_{1/2}$	-4.95884	0.87049	-5.70575	0.863744
0 $p_{1/2}$	-29.314	0.905144	-36.2132	0.904116
0 $p_{3/2}$	-32.2869	0.915634	-39.2087	0.913116
0 $d_{3/2}$	-5.31948	0.852831	-5.9818	0.848605
0 $d_{5/2}$	-16.1159	0.875426	-22.946	0.900197
0 $f_{5/2}$	-2.40131	0.0351818	-2.70812	0.0356789
0 $f_{7/2}$	-2.98448	0.0465509	-3.27588	0.0456802
0 $g_{7/2}$	-0.330306	0.00469718	-0.606152	0.00763109
0 $g_{9/2}$	-1.15944	0.0164019	-1.58873	0.0201579
0 $h_{9/2}$	-0.0559671	0.00079904	-0.0783799	0.000992228
0 $h_{11/2}$	-0.0871634	0.00125027	-0.142465	0.0018065

Table 4.1: The parameters for spectral functions in partial wave basis. Where ϵ_{nlj} indicates the pick for corresponding partial wave strength, and N_{nlj} is the occupation number.

Conservation of total momentum $\boldsymbol{K}$ eliminates one of the two $\boldsymbol{k}_2$ integrals. The spectral density in the vector basis can be constructed from partial wave summation. Rotation invariance allows constructing the $\mathcal{T}-$matrix as discussed in Sec.(4.2). More explicitly:

$$\begin{aligned}\Delta\Sigma_{\downarrow}^{m_1^t}(\boldsymbol{k}_1 m_1^s, \tilde{\boldsymbol{k}}_1 \tilde{m}_1^s; E) = 8 \times & \sum_{m_2^s \tilde{m}_2^s m_2^t} \sum_{S M_S M_S'} \int \mathrm{d}^3\boldsymbol{k} \\ & \times (s_1 m_1^s s_2 m_2^s | S M_S)(\tilde{s}_1 \tilde{m}_1^s \tilde{s}_2 \tilde{m}_2^s | S M_S') \\ & \times (t_1 m_1^t t_2 m_2^t | T M_T)(t_1 m_1^t t_2 m_2^t | T M_T) \\ \times \sum_{nlj} C_{nlj} N_{lj}^n \langle \boldsymbol{k} M_S | \Delta\Gamma_{\downarrow}^{S T M_T}(\boldsymbol{K}, E + \frac{\epsilon_{lj}^n}{N_{lj}^n}) | \boldsymbol{k}' M_S' \rangle & \phi_{lj}^{n m_2^t}(|\boldsymbol{k}_2|) \phi_{lj}^{n m_2^t}(|\tilde{\boldsymbol{k}}_2|), \quad (4.60)\end{aligned}$$

where C_{nlj} are the coefficients for the transformation of the spectral functions from the partial wave basis to vector basis.

Explicitly:

$$\begin{aligned} C_{nlj} = & \frac{(-1)^{2m_j - m_s - m_s'}}{4\pi} \sum_{\ell j} (\ell\ m_j - m_s\ s\ m_s | j\ m_j) \\ & \times (\ell\ m_j - m_s'\ s\ m_s' | j\ m_j)(2\ell + 1) \\ & \times \sqrt{\frac{(\ell - m_j + m_s')!}{(\ell + m_j - m_s')!}} \sqrt{\frac{(\ell - m_j + m_s)!}{(\ell + m_j - m_s)!}} \\ & \times P_{\ell\ m_j - m_s'}(X_k') P_{\ell\ m_j - m_s}(X_k). \end{aligned} \tag{4.61}$$

4.4.3 Results and discussion for Ladder self-energy

With the above preparation, the ladder self-energy can be calculated step by step and then put into the scattering calculation to generate cross sections. However, it is a function of seven parameters, three momentum variables k_1, θ_1, $\tilde{k}_1$; two spin projection variables m_1^s, $\tilde{m}_1^s$; one isospin projection variable m_1^t; and very important one energy variable E. To generate one matrix element for a set of the seven parameters, a single core processor takes a substantial amount of CPU time. Constructing the whole ladder self-energy can only be done at supercomputers. Instead, we find a workaround to test the new object. Only a few data points are generated for a chosen angle 15° and the energy is fixed to 100 MeV. As can be seen in Fig.(4.7), the real part of spin "up-up" diagonal matrix elements are plotted in the momentum range 0-4 fm^{-1}, similarly Fig.(4.8) for the imaginary part of spin "up-up", and Fig.(4.9) for the real part of spin "down-up" diagonal matrix elements. It is worth mentioning that the ladder self-energy has very similar symmetry properties as the

HF self-energy as shown in Eq.(4.39), explicitly:

$$\Delta\Sigma_{\downarrow}^{m_1^t}(\boldsymbol{k}_1 m_1^s, \tilde{\boldsymbol{k}}_1 \tilde{m}_1^s; E) = (-1)^{(1+m_1^s+\tilde{m}_1^s)} \Delta\Sigma_{\downarrow}^{m_1^t}(\boldsymbol{k}_1 - m_1^s, \tilde{\boldsymbol{k}}_1 - \tilde{m}_1^s; E). \tag{4.62}$$

The difference between proton and neutron ladder self-energy is less than 2% using the AV18 interaction. Once we collect those data, a fit to potentials similar to those that are used in the DOM can be made to calculate the cross sections.

The parametrization of the real part of the DOM potentials includes a Woods-Saxon-like nonlocal term together with the Coulomb and local spin-orbit contributions, which are energy independent and in $\boldsymbol{r}$ space are given by:

$$\text{Re } \Sigma(\boldsymbol{r}, \boldsymbol{r}') = \Sigma^{nonl}(\boldsymbol{r}, \boldsymbol{r}') + \delta(\boldsymbol{r} - \boldsymbol{r}')[V_C(r) + V^{so}(r)]. \tag{4.63}$$

For simplicity we only include the volume term for the nonlocal part in the fitting procedure, which has the form of Wood-Saxon form factors times a Gaussian, explicitly:

$$\Sigma^{nonl}(\boldsymbol{r}, \boldsymbol{r}') = -V^{vol} f(\tilde{r}, r^{vol}, a^{vol}) \times H(\boldsymbol{s}; \beta^{vol}), \tag{4.64}$$

where V^{vol}, r^{vol}, a^{vol} and β^{vol} are the four parameters for the volume term. Non-locality is represented by the Gaussian

$$H(\boldsymbol{s}; \beta) = \frac{exp(-\boldsymbol{s}^2/\beta^2)}{\pi^{3/2}\beta^3}. \tag{4.65}$$

where $\boldsymbol{s} = \boldsymbol{r} - \boldsymbol{r}'$. And the Woods-Saxon term is as usual:

$$f(\tilde{r}, r^{vol}, a^{vol}) = \left[1 + exp\left(\frac{\tilde{r} - r^{vol}A^{1/3}}{a^{vol}}\right)\right]^{-1}. \tag{4.66}$$

Where $\tilde{r} = (r + r')/2$ and A is the mass number.

The spin-orbit term has the following form:

$$V^{so}(r) = \left(\frac{\hbar}{m_\pi c}\right)^2 V^{so}\frac{1}{r}\frac{\mathrm{d}}{\mathrm{d}r}f(r, r^{so}, a^{so})\ell\cdot\sigma. \tag{4.67}$$

where $(\hbar/m_\pi c)^2 = 2.0$ fm^2 as in Ref. [91], and $f(r, r^{so}, a^{so})$ is the usual Woods-Saxon term as Eq.(4.66). Only three fitting parameters are needed for the spin-orbit term–V^{so}, r^{so} and a^{so}. As the ladder self-energy is in $\boldsymbol{k}$ space, an appropriate Fourier transform is required. We write out the spin-orbit formalism because it needs extra attention. A spin-orbit operator depends only on the magnitude of $\boldsymbol{r}$ can be written in momentum basis as follows:

$$\begin{aligned}\langle \boldsymbol{k}_1|V_{LS}(r)\boldsymbol{l}\cdot\sigma|\boldsymbol{k}_2\rangle &= \langle \boldsymbol{k}_1|V_{LS}\boldsymbol{r}\times\boldsymbol{p}|\boldsymbol{k}_2\rangle\cdot\sigma \\ &= i\boldsymbol{k}_1\times\boldsymbol{k}_2\cdot\sigma\ \frac{1}{2\pi^2}\frac{1}{q^2}\int \mathrm{d}r_1\ r_1(r_1 cos(qr_1) - \frac{sin(qr_1)}{q})V_{LS}(r_1),\end{aligned} \tag{4.68}$$

where $q = |\boldsymbol{q}| = |\boldsymbol{k}_1 - \boldsymbol{k}_2|$.

The imaginary part of the ladder self-energy is also fitted but with volume part only, as shown below:

$$\text{Im}\ \Sigma(\boldsymbol{r}, \boldsymbol{r}') = -V_{im}^{vol} f(\tilde{r}, r_{im}^{vol}, a_{im}^{vol}) \times H(\boldsymbol{s}; \beta_{im}^{vol}). \tag{4.69}$$

With this preparation, the fitted potentials are shown in Fig.(4.7), Fig.(4.8) and Fig.(4.9) for the real volume term, the imaginary volume term and the real spin-orbit term respectively. All the parameters are listed in the Tab.(4.2). The radius and diffuseness parameters are in reasonable agreement with the corresponding values of nonlocal DOM potentials. The nonlocality parameters also appear quite reasonable. The strength of the volume term also compares well with the HF value of the DOM potential (100 MeV for ^{40}Ca), taking into account that additional dispersive corrections and surface terms should be considered. The parameters for the local spin-orbit term exhibit a rather large diffuseness parameter. We

note that additional angles in the microscopic self-energy as well as the convergence with respect to the angular momentum projection should be considered in the future.

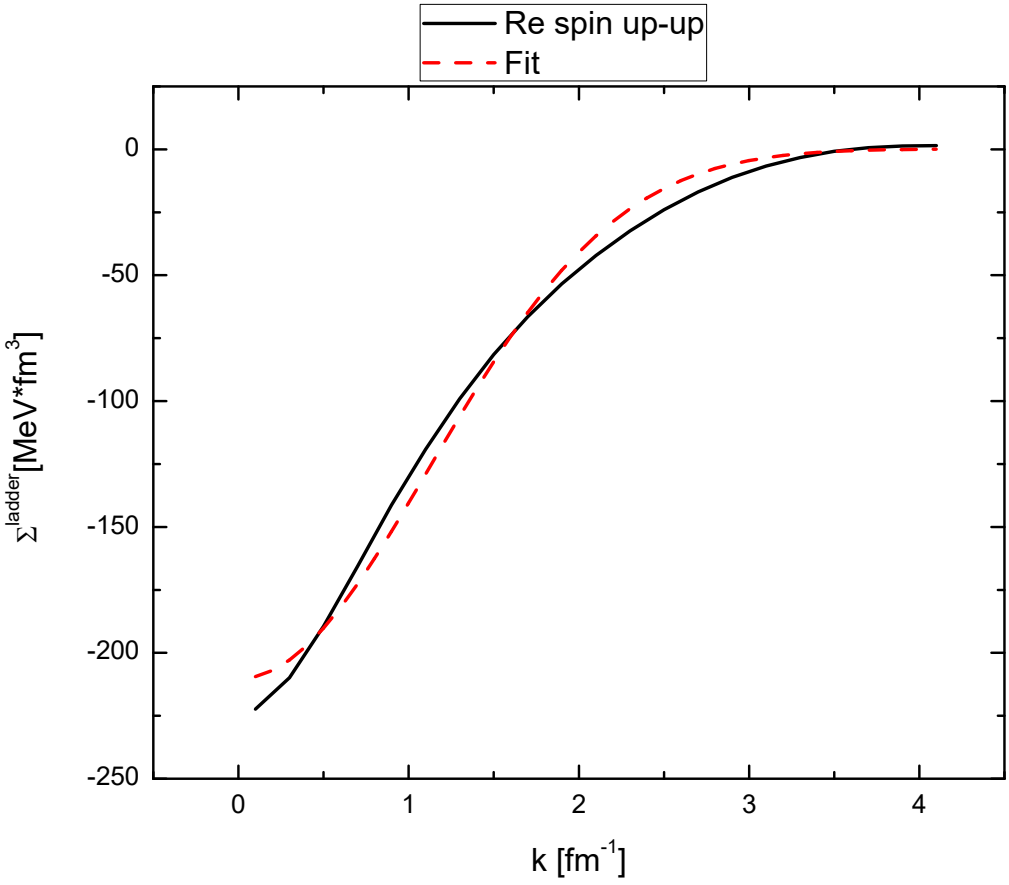

Figure 4.7: The diagonal matrix elements of the real part of spin "up-up" ladder self-energy are plotted in the momentum range 0-4 fm^{-1} as the solid black curve, the corresponding fitted potential is the dashed red curve.

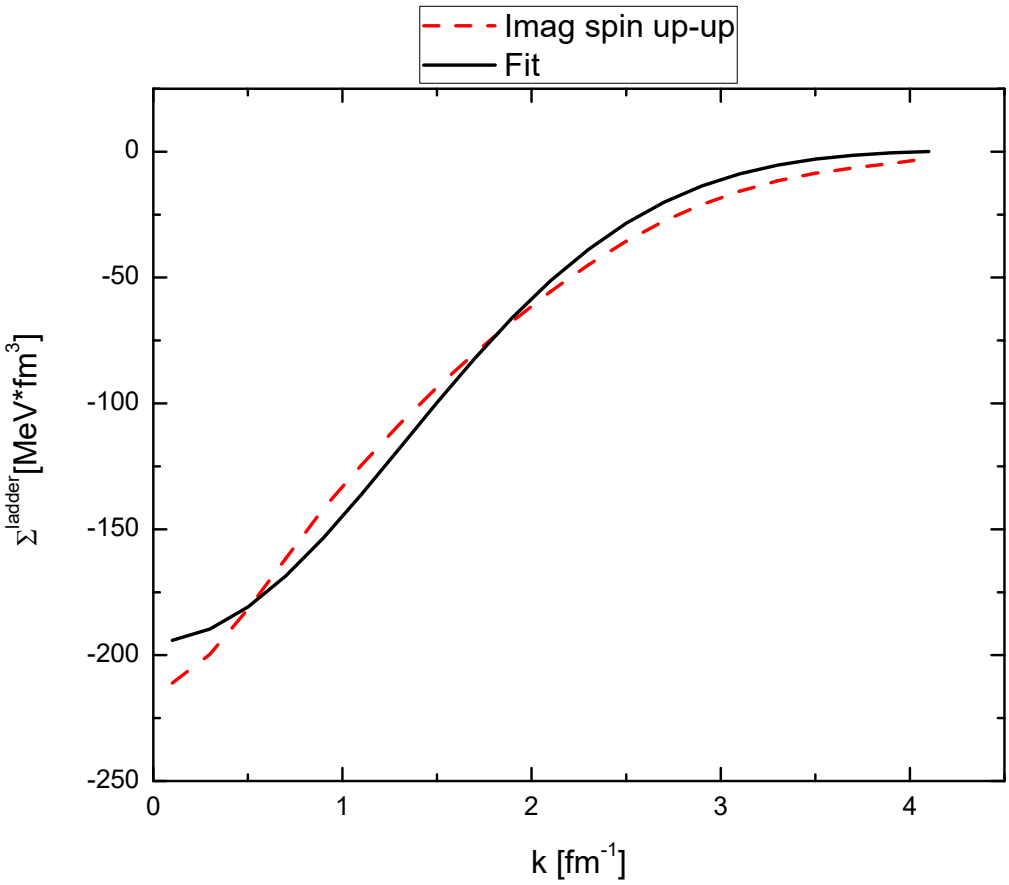

Figure 4.8: The diagonal matrix elements of the imaginary part of spin "up-up" ladder self-energy are plotted in the momentum range 0-4 fm^{-1} as the solid black curve, the corresponding fitted potential is the dashed red curve.

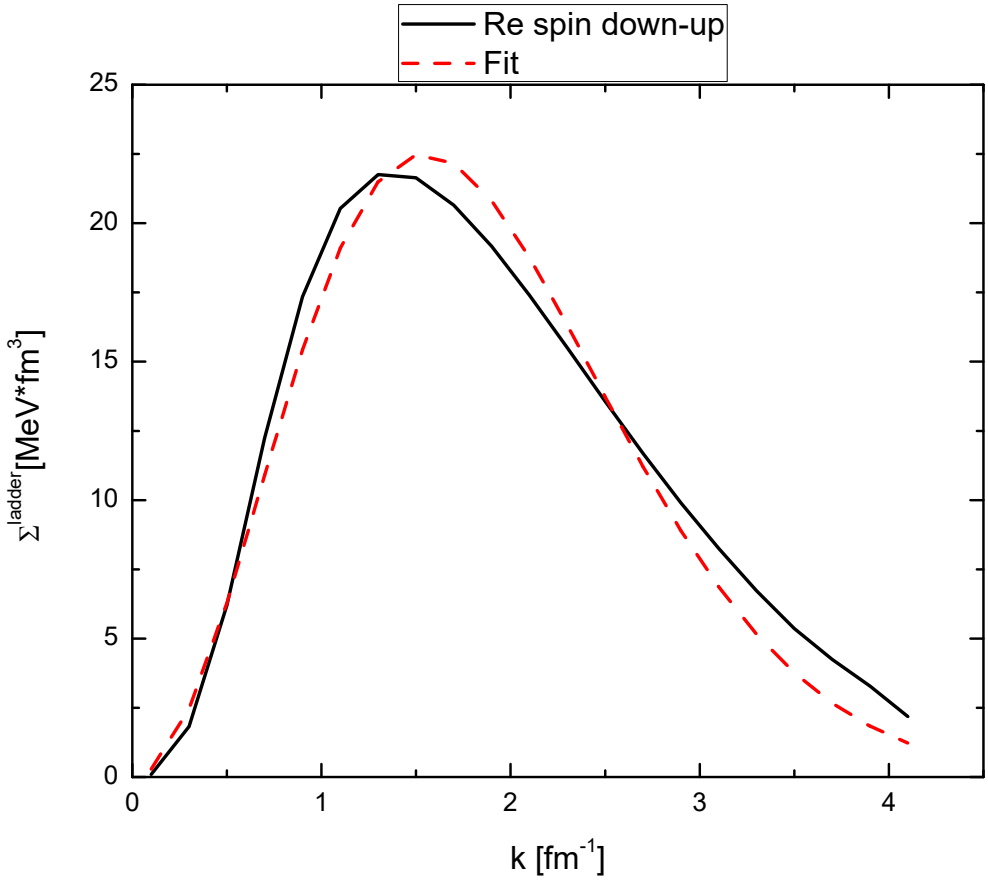

Figure 4.9: The diagonal matrix elements of the real part of spin "down-up" ladder self-energy are plotted in the momentum range 0-4 fm^{-1} as solid black curve, the corresponding fitted potential are in dashed red curve.

Volume term			
Real		Imaginary	
V^{vol} [MeV]	151.8	V^{vol} [MeV]	145.5
r^{vol} [fm]	1.18	r^{vol} [fm]	1.17
a^{vol} [fm]	0.64	a^{vol} [fm]	0.62
β^{vol} [fm]	0.96	β^{vol} [fm]	0.71
Spin-orbit term			
Real			
V^{so} [MeV]	24.7		
r^{so} [fm]	0.95		
a^{so} [fm]	1.71		

Table 4.2: Fitted parameters for volume term and spin-orbit term of the DOM-inspired potentials for ^{40}Ca corresponds to Eq.(4.64), Eq.(4.67) and Eq.(4.69).

Chapter 5

Conclusions and Outlook

In chapter 2, we employ a simple method based on a generalization of the Cooper problem to study the influence on the pairing properties when the finite total momentum and the nucleon asymmetry of the system are considered. We conclude that an optimized finite total momentum will enhance pairing for the asymmetric system, although a finite total momentum and asymmetry itself will suppress pairing. In principle, a systematic treatment of pairing requires thermodynamics under the BCS formalism, as discussed in Ref. [15], where finite temperature gaps are calculated for asymmetric nuclear matter. The phase competition and separation between the unpaired phase, the BCS phase, the BEC phase and the LOFF phase are also controlled by thermodynamics [17, 19, 45]. In order to generate realistic pairing gaps, one should extend the BCS formalism to include the finite total momentum $\boldsymbol{K}$, the isospin asymmetry factor α and the temperature T dependence.

In chapter 3, we have proposed a method that combines the self-consistent Green's functions framework for the treatment of SRC and Fermi liquid theory for the incorporation of LRC to the neutron matter pairing problem with NN interactions. This approach has two major ingredients. On the one hand, extrapolated normal ladder self-energies provide access to zero

temperature spectral functions and, in turn, these give rise to depleted energy denominators that quench the gap. On the other hand, the pairing interaction is treated beyond the static, bare level. Screening is provided by considering vertices represented by Landau parameters, that couple to spin and density oscillations, whose collectivity is also controlled by the same Landau parameters.

The effect of SRC is to remove strength from the Fermi surface, thus necessarily reducing the gap. Compared to a quasi-particle, BCS-like picture, the energy denominators in the gap equation are quenched by an approximately momentum and density independent factor. In general, this is very different from the corresponding $\mathcal{Z}$-factors associated to the ladder SCGF self-energy. This indicates that pairing calculations with $\mathcal{Z}$-factors do not consider the full effect of SRC in a consistent way.

We take three major conclusions from that chapter. First, the universal effect of SRC is to reduce the gap substantially with respect to its BCS value in the whole momentum range. In the singlet channel this translates into a decrease in the Fermi surface gap of about $10-15\%$. In the triplet channel, the gaps were small, below 1 MeV, at the BCS level. When SRC are considered, gaps reduce further to below 0.2 MeV throughout a wide density regime. Second, whereas for the singlet case the effect of SRC is of the same order of the screening provided by LRC, in the triplet case LRC have an anti-screening effect that modestly increases the SRC determined gap for all three NN interactions. Third, the density dependence of triplet gaps is substantially modified by SRC and LRC. We find gaps that open above 1.2 fm^{-1} and close below 2.6 fm^{-1} in all cases, with maxima that hardly reach 0.2 MeV. Small triplet gaps of a similar size are commensurate with the Cassiopea A rapid cooling scenario presented in Ref. [36].

We have performed calculations with three very different, but phase-shift equivalent, interactions. For the singlet channel, our conclusions are extremely robust and independent of

the NN force. Triplet gaps, in contrast, depend on the specifics of the interaction itself. CD-Bonn in general provides the largest and widest triplet gaps, whereas Av18 provides small and narrow pairing gaps. Cutoff effects artificially cut the triplet gaps of N3LO above 2.5 fm^{-1}. We want to stress, however, that the SRC and LRC effects are universal and independent of the nuclear force under consideration. Work on incorporating three-nucleon forces in a consistent way, following Ref. [92], is our first priority in the near future. In view of the impact of correlations on the BCS gaps on these three different interactions, we do not expect any qualitative differences with respect to the present results.

The extension of the approach to asymmetric nuclear systems is also important [18, 69]. There is a small admixture of protons inside neutron stars, and their pairing is relevant for neutron star matter. In-medium SRC effects should be similar for proton pairing, and the suppression in the proton channel might have consequences for neutron star cooling. Pairing at finite momentum is also a relevant physical phenomenon, particularly since it can lead to different pairing phases [17]. The interplay of correlation and finite momentum effects will necessarily lead to a change in the phase diagram with respect to BCS calculations.

These calculations represent a first controlled step towards a full treatment of superfluidity within the Green's function formalism. At the SRC level, our treatment does not allow for the superfluid phase to feed back into the determination of the normal propagators. While feedback effects will be small, the reformulation of the problem in a Gorkov context would avoid the need of extrapolations from finite temperature. Such a self-consistent treatment of the ladder approximation in the pairing phase has never been implemented to our knowledge. At the LRC level, consistency at the Landau parameter level could provide small, quantitative differences in our results. Furthermore, the full spin dependence of the effective interaction, beyond the traditional Landau parameters [74], could have an effect on pairing gaps. Finally, the inclusion of polarization effects beyond the low-momentum transfer limit

is an interesting, if computationally expensive, possibility.

In chapter 4, the optical potential beyond the mean-field approximation has been constructed as the first step towards the SCGF treatment for the nucleon-nucleus scattering problem that includes SRC. A comparison of the resulting real and imaginary part of the self-energy at 100 MeV with the corresponding dispersive-optical-model potentials shows reasonable agreement. In general, a calculation with the full optical potential at any relevant energy can be performed without much further effort but requires more computational resources. The results are quite reasonable considering it is the first step with additional approximations. We note that, this method is capable of incorporating isospin asymmetric systems as well.

Appendices

Appendix A

Pauli operators with two Fermi spheres

The angle-averaged asymmetric Pauli operators Q_{pp}^{As} (see Eq.2.30) and Q_{hh}^{As} are shown in Tab. A.1 and A.2. By calculating the step functions in Eq.(2.30) for each configuration of K_F^N and K_F^P corresponding to rows, the right two columns indicates the possible phase space and their strength.

Table A.1: The dependence of the angle-averaged asymmetric Pauli operators Q_{pp}^{As} and Q_{hh}^{As} on K_F^N and K_F^P. The final results are in the right two columns while each row indicates a specific range for K_F^N and K_F^P.

Total wave vector(K)				$\overline{Q_{hh}}(K,q)$	$\overline{Q_{pp}}(K,q)$
$\frac{K}{2}<K_F^P<K_F^N$	$0<q<K_F^P-\frac{K}{2}$			1	0
	$if\ \frac{K}{2}<\frac{1}{2}(K_F^N-K_F^P)$	$K_F^P-\frac{K}{2}<q<K_F^P+\frac{K}{2}<K_F^N-\frac{K}{2}$		$\frac{1}{2}(1-\frac{\frac{K^2}{4}+q^2-K_F^{P2}}{Kq})$	0
		$K_F^P+\frac{K}{2}<q<K_F^N-\frac{K}{2}$		0	0
		$K_F^N-\frac{K}{2}<q<K_F^N+\frac{K}{2}$		0	$\frac{1}{2}(1-\frac{K_F^{N2}-\frac{K^2}{4}-q^2}{Kq})$
		$K_F^N+\frac{K}{2}<q$		0	1
	$if\ \frac{K}{2}>\frac{1}{2}(K_F^N-K_F^P)$	$K_F^P-\frac{K}{2}<q<K_F^N-\frac{K}{2}<K_F^P+\frac{K}{2}$		$\frac{1}{2}(1-\frac{\frac{K^2}{4}+q^2-K_F^{P2}}{Kq})$	0
		$K_F^N-\frac{K}{2}<q<(\frac{K_F^{N2}+K_F^{P2}}{2}-\frac{K^2}{4})^{\frac{1}{2}}<K_F^P+\frac{K}{2}$		$\frac{K_F^{N2}+K_F^{P2}-2(\frac{K^2}{4}+q^2)}{2Kq}$	0
		$(\frac{K_F^{N2}+K_F^{P2}}{2}-\frac{K^2}{4})^{\frac{1}{2}}<q<K_F^P+\frac{K}{2}$		0	$-\frac{K_F^{N2}+K_F^{P2}-2(\frac{K^2}{4}+q^2)}{2Kq}$
		$K_F^P+\frac{K}{2}<q<K_F^N+\frac{K}{2}$		0	$\frac{1}{2}(1-\frac{K_F^{N2}-\frac{K^2}{4}-q^2}{Kq})$
		$K_F^N+\frac{K}{2}<q$		0	1
$K_F^P<\frac{K}{2}<K_F^N$	$if\ \frac{K}{2}<\frac{1}{2}(K_F^N+K_F^P)$	$0<q<\frac{K}{2}-K_F^P<K_F^N-\frac{K}{2}$		0	0
		$if\ \frac{K}{2}<\frac{1}{2}(K_F^N-K_F^P)$	$\frac{K}{2}-K_F^P<q<\frac{K}{2}+K_F^P<K_F^N-\frac{K}{2}$	$\frac{1}{2}(1-\frac{\frac{K^2}{4}+q^2-K_F^{P2}}{Kq})$	0
			$\frac{K}{2}+K_F^P<q<K_F^N-\frac{K}{2}$	0	0
			$K_F^N-\frac{K}{2}<q<K_F^N+\frac{K}{2}$	0	$\frac{1}{2}(1-\frac{K_F^{N2}-\frac{K^2}{4}-q^2}{Kq})$
			$K_F^N+\frac{K}{2}<q$	0	1
		$if\ \frac{K}{2}>\frac{1}{2}(K_F^N-K_F^P)$	$\frac{K}{2}-K_F^P<q<K_F^N-\frac{K}{2}<\frac{K}{2}+K_F^P$	$\frac{1}{2}(1-\frac{\frac{K^2}{4}+q^2-K_F^{P2}}{Kq})$	0
			$K_F^N-\frac{K}{2}<q<(\frac{K_F^{N2}+K_F^{P2}}{2}-\frac{K^2}{4})^{\frac{1}{2}}<K_F^P+\frac{K}{2}$	$\frac{K_F^{N2}+K_F^{P2}-2(\frac{K^2}{4}+q^2)}{2Kq}$	0
			$(\frac{K_F^{N2}+K_F^{P2}}{2}-\frac{K^2}{4})^{\frac{1}{2}}<q<K_F^P+\frac{K}{2}$	0	$-\frac{K_F^{N2}+K_F^{P2}-2(\frac{K^2}{4}+q^2)}{2Kq}$
			$K_F^P+\frac{K}{2}<q<K_F^N+\frac{K}{2}$	0	$\frac{1}{2}(1-\frac{K_F^{N2}-\frac{K^2}{4}-q^2}{Kq})$
			$K_F^N+\frac{K}{2}<q$	0	1
	$if\ \frac{K}{2}>\frac{1}{2}(K_F^N+K_F^P)$	$0<q<K_F^N-\frac{K}{2}<\frac{K}{2}-K_F^P$		0	0

Table A.2: Continuation of table A.1.

		$K_F^N - \frac{K}{2} < q < K_F^N + \frac{K}{2}$	0	$\frac{1}{2}(1 - \frac{K_F^{N2} - \frac{K^2}{4} - q^2}{Kq})$
		$K_F^N + \frac{K}{2} < q$	0	1
$K_F^P < K_F^N < \frac{K}{2}$	$0 < q < \frac{K}{2} - K_F^N < \frac{K}{2} - K_F^P$		0	1
	$\frac{K}{2} - K_F^N < q < \frac{K}{2} - K_F^P$		0	$\frac{1}{2}(1 - \frac{K_F^{N2} - \frac{K^2}{4} - q^2}{Kq})$
	$\frac{K}{2} - K_F^P < q < \frac{K}{2} + K_F^P$		0	$-\frac{K_F^{N2} + K_F^{P2} - 2(\frac{K^2}{4} + q^2)}{2Kq}$
	$\frac{K}{2} + K_F^P < q < \frac{K}{2} + K_F^N$		0	$\frac{1}{2}(1 - \frac{K_F^{N2} - \frac{K^2}{4} - q^2}{Kq})$
	$\frac{K}{2} + K_F^N < q$		0	1

Appendix B

Numerical treatment of the temperature extrapolation

For a given density, ladder self-energy calculations are typically performed for a set of $N_T \approx 3$ to 10 temperatures. The degeneracy parameter, $\zeta = \frac{T}{\epsilon_F}$, with ϵ_F the non-interacting Fermi energy, is a proxy for temperature in Fermi gases and is a natural dimensionless extrapolation parameter, in accordance to the Sommerfeld expansion [93]. At each ζ, the real and imaginary parts of the self energy are stored as arrays in energy and momentum space. Typically, $\approx$ 4000 to 11000 energies are needed, whereas we work with a fix set of 70 points in the momentum mesh. The self-energy is fit by a polynomial function of ζ, $\Sigma(k,\omega;\zeta) = \sum_{l=0}^{L} a_l(k,\omega)\zeta^{2l}$, in a window of ζ values. For a given density, we take an upper limit of $\zeta \approx 1$ and a lower limit of $\zeta \gtrsim 0.07$ (as long as the pairing instability does not set in). This ensures that the finite temperature data is neither thermally dominated ($\zeta \gg 1$) nor insensitive to thermal effects ($\zeta \ll 1$). Fig.(B.1) provides an illustration of the density and temperature mesh that we have used for the extrapolations with AV18.

The zero-temperature self-energy is the independent coefficient of the polynomial fit, $a_0(k,\omega)$,

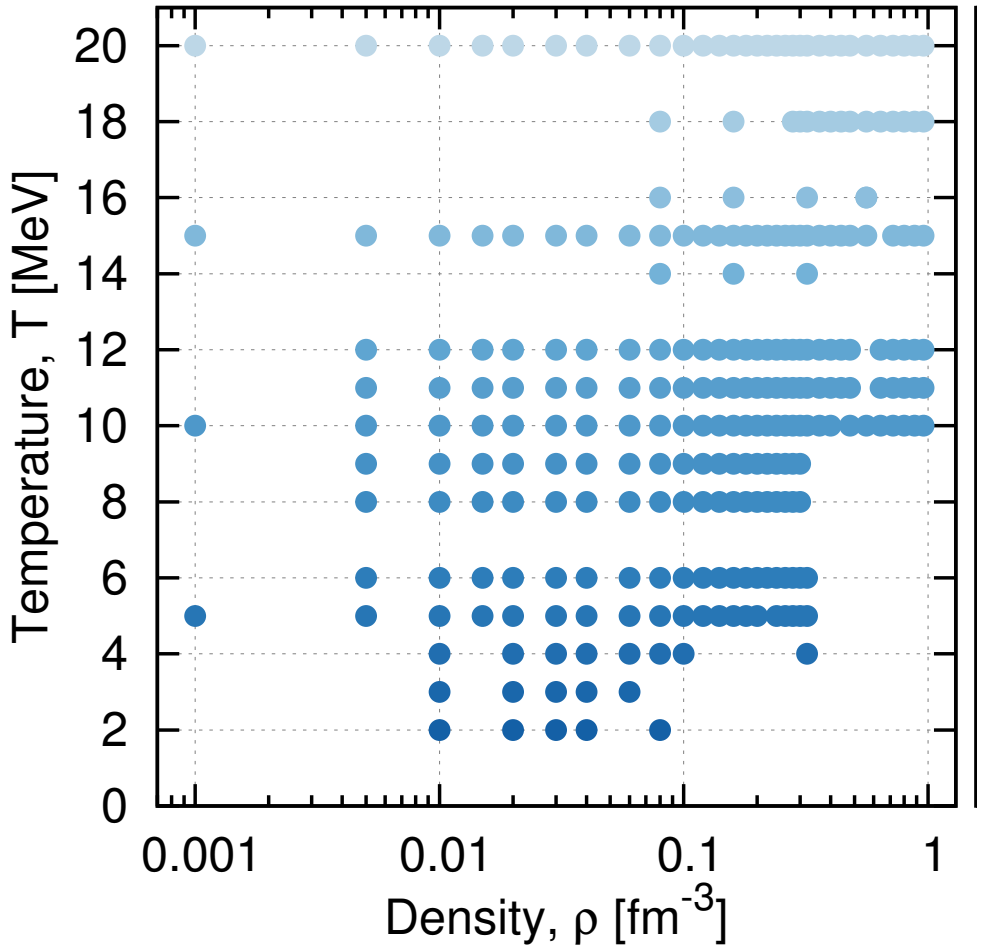

Figure B.1: Each point in this plot corresponds to a density and temperature where ladder self-energies have been computed. Finite temperature points are used to extrapolate to zero temperature.

although in principle the fit can also be used to compute self-energies at arbitrary temperatures. For practical purposes, the interpolation involves only even powers, $2l$. Close to the Fermi surface, the temperature dependence of the self-energy is indeed expected to be quadratic [63]. However, numerically computed self-energies, particularly close to $\omega = \mu$, need not be soft, continuous functions of degeneracy, due to numerical noise. Consequently, a single fit might extrapolate quantities in an unphysical way. For this reason, we perform not only one, but a series of fits with different values of L, the maximum power of the poly-

nomial. Generally, we go from $L = 1$ (corresponding to a T^2 dependence) to about $L = 4$, depending on the total number of temperatures available. All polynomial fits are performed using a χ^2 minimisation procedure, which helps in evening out any numerical noise.

In the implementation, we extrapolate separately the imaginary and the real parts of the self-energy. Pairing is sensitive to the properties of Σ close to the Fermi energy. This is where the temperature dependence is more difficult to capture with fits. For a given polynomial order, L, we therefore allow for two different options. We either take the extrapolated $\mathrm{Im}\Sigma$ at face value ($\mathrm{Im}\Sigma \leq 0$ is imposed throughout, though) or we allow for a second option, where we match $\mathrm{Im}\Sigma$ to the analytic function:

$$\mathrm{Im}\Sigma(k, \omega \approx \mu; T = 0) \approx a_k(\omega - \mu)^2 e^{-b_k(\omega-\mu)} \tag{B.1}$$

in the vicinity of the Fermi energy. This has the correct quadratic dependence in energy of a normal Fermi liquid [94]. The exponential factor allows for a certain degree of asymmetry below and above the Fermi surface, which we find to be essential in order to match the numerical self-energies. This function is matched to the self-energy in a given range of energies, which is different for every momentum, k.

With access to the $T = 0$ self-energies and spectral functions, one can compute several zero temperature properties. For instance, the energy per particle, $\frac{E}{A}$, is obtained from the Koltun sum-rule at zero temperature [21]. Alternatively, the finite temperature SCGF calculations yield a set of energies which can independently be extrapolated to zero temperature using a polynomial fit. For simplicity, we take the same L in this fit and in that of the associated self-energy.

A good extrapolation procedure for the self-energy should ensure consistency between the micro- and the macroscopic results. In the example above, we would like the Koltun sum-rule

at zero temperature to yield the same energy per particle than the extrapolated value from finite temperature data. We therefore construct a quality measure that quantifies the distance between extrapolations of micro- and macroscopic evaluations for some relevant data. The measure is built from a weighted sum of the relative differences between microscopic and macroscopic determinations of density, chemical potentials, energies, kinetic energies and Z-factors. The latter is determined independently from the discontinuity of the momentum distribution at the Fermi surface and from the on-shell derivatives of self-energies. The polynomial with L that minimises the quality measure, whether matched or not according to Eq. (B.1), is used in the extrapolation. This guarantees that the associated self-energy is consistent with both the microscopic and the macroscopic pseudo-data. The extrapolation procedure is automated, in an effort to avoid any biases in the calculation.

Below T_c and as the temperature approaches zero asymptotically, the normal spectral function becomes an increasingly sharp function of energy close to the Fermi surface. It is important to keep track of these narrow structures in the calculation of $n(k)$. For a given momentum, k, the missing strength due to uncaptured narrow peaks can be estimated from the energy spectral function sum-rule [21]. Deviations from 1 indicate missing strength contributions, which we use to correct the momentum distribution. We include a quasi-particle term that is weighted to account for the missing strength. We have tested this procedure against an independent determination of the momentum distribution, based on the derivatives of the zero-temperature self-energy [28], and we have found quantitative agreement.

Missing strength corrections are also relevant for the double convolution energy denominator of Eq. (3.31). We use the sum-rule of the lowest-order two-particle propagator,

$$\int \frac{\mathrm{d}\Omega}{2\pi} \mathcal{G}^0_{II}(k, k' = k, \Omega) = 1 - 2n(k)\,, \tag{B.2}$$

to estimate the missing strength ς_k at a given momentum. The origin of this missing strength

lies in the finite meshes in the calculation, and the difficulty of keeping track of narrow structures in energy space. The missing strength correction in our ladder calculations is of the order of less than one percent away from the Fermi surface. ς_k is generally largest (50 % or above) for momenta which are within $2-3\,\%$ of the Fermi surface. Hence, the energy denominator only needs corrections in the close vicinity of the Fermi surface. We implement this correction by means of the replacement,

$$\frac{1}{2\chi_c(k)} \to \frac{1}{2\chi(k)} + \frac{\varsigma_k}{2(\varepsilon_k - \mu)}\,. \tag{B.3}$$

The resulting energy denominators are continuous, soft functions of momentum as a function of momentum (see Panel (b) in Fig. 3.8) and in a wide range of densities (see panels (d)-(f) in Fig. 3.9).

Bibliography

[1] R. D. Mattuck. *A guide to Feynman diagrams in the many-body problem*. McGraw-Hill New York, 2nd edition, 1976.

[2] R. B. Wiringa, V. G. J. Stoks and R. Schiavilla. *Phys. Rev. C*, 51:38, 1995.

[3] R. Machleidt, F. Sammarruca and Y. Song. *Phys. Rev. C*, 53:R1483, 1996.

[4] D. R. Entem and R. Machleidt. *Phys. Rev. C*, 68:041001, 2003.

[5] H. K. Onnes. *Commun. Phys. Lab. Univ. Leiden*, 12:120, 1911.

[6] J. Bardeen, L. N. Cooper and J. R. Schrieffer. *Phys. Rev.*, 108:1175, 1957.

[7] J. F. Allen and A. D. Misener. *Nature*, 142:643, 1938.

[8] D. D. Osheroff, R. C. Richardson and D. M. Lee. *Phys. Rev. Lett.*, 28:885, 1972.

[9] S. N. Bose. *Zeitschrift für Physik*, 26:178, 1924.

[10] M. H. Anderson, J. R. Ensher, M. R. Matthews, C. E. Wieman and E. A. Cornell. *Science*, 269:198, 1995.

[11] A. I. Larkin, Y. N. Ovchinnikov and Z. Eksp. *Teor.Fiz.47, 1136 (1964).Sov.Phys.JETP*, 20:762, 1965.

[12] P. Fulde and R. A. Ferrell. *Phys. Rev.*, 135:A550, 1964.

[13] M. G. Alford, A. Schmitt, K. Rajagopal and T. Schäfer. *Rev. Mod. Phys.*, 80:1455, 2008.

[14] S. Frauendorf and A. O. Macchiavelli. *Prog. Part. Nucl. Phys.*, 78:24, 2014.

[15] A. Sedrakian and U. Lombardo. *Phys. Rev. Lett.*, 84:602, 2000.

[16] H. Müther and A. Sedrakian. *Phys. Rev. C*, 67:015802, 2003.

[17] M. Stein, A. Sedrakian, X. G. Huang and J. W. Clark. *Phys. Rev. C*, 90:065804, 2014.

[18] U. Lombardo, P. Nozières, P. Schuck, H. J. Schulze and A. Sedrakian. *Phys. Rev. C*, 64:064314, 2001.

[19] S. Mao, X. G. Huang and P. F. Zhuang. *Phys. Rev. C*, 79:034304, 2009.

[20] X. G. Huang, X. W. Hao and P. F. Zhuang. *International Journal of Modern Physics E*, 16:2307, 2007.

[21] W. H. Dickhoff and D. Van Neck. *Many-Body Theory Exposed!* World Scientific, New Jersey, 2nd edition, 2008.

[22] A. Bohr, B. R. Mottelson and D. Pines. *Phys. Rev.*, 110:936, 1958.

[23] A. Gezerlis, G. F. Bertsch and Y. L. Luo. *Phys. Rev. Lett.*, 106:252502, 2011.

[24] L. Lapikás. *Nucl. Phys. A*, 553:297, 1993.

[25] O. Benhar, I. Sick and D. Day. *Rev. Mod. Phys.*, 80:189, 2008.

[26] J. Arrington, D. W. Higinbotham, G. Rosner and M. Sargsian. *Prog. Part. Nucl. Phys.*, 67:898, 2012.

[27] D. Rohe. *Phys. Rev. Lett.*, 93:182501, 2004.

[28] A. Rios, W. H. Dickhoff and A. Polls. *Phys. Rev. C*, 79:064308, 2009.

[29] A. Rios, A. Polls and W. H. Dickhoff. *Phys. Rev. C*, 89:044303, 2014.

[30] W. H. Dickhoff and C. Barbieri. *Prog. Part. Nucl. Phys.*, 52:377, 2004.

[31] L. G. Cao, U. Lombardo and P. Schuck. *Phys. Rev. C*, 74:064301, 2006.

[32] C. Shen, U. Lombardo, P. Schuck, W. Zuo and N. Sandulescu. *Phys. Rev. C*, 67:061302, 2003.

[33] P. W. Anderson and N. Itoh. *Nature*, 256:25, 1975.

[34] A. B. Migdal. *Nuclear Physics*, 13:655, 1959.

[35] D. J. Dean and M. Hjorth-Jensen. *Rev. Mod. Phys.*, 75:607, 2003.

[36] D. Page, M. Prakash, J. Lattimer and A. W. Steiner. *Phys. Rev. Lett.*, 106:081101, 2011.

[37] D. Pines and M. A. Alpar. *Nature*, 316:27, 1985.

[38] B. Haskell and A. Melatos. *Int. J. Mod. Phys. D*, 24:1530008, 2015.

[39] D. G. Yakovlev and C. J. Pethick. *Annu. Rev. Astron. Astrophys.*, 42:169, 2004.

[40] L. B. Leinson. *Phys. Rev. C*, 81:025501, 2010.

[41] C. Mahaux and R. Sartor. *Adv. Nucl. Phys.*, 20:1, 1991.

[42] M. H. Mahzoon, R. J. Charity, W. H. Dickhoff, H. Dussan and S. J. Waldecker. *Phys. Rev. Lett.*, 112:162503, 2014.

[43] C. Elster, S. P. Weppner and C. R. Chinn. *Phys. Rev. C*, 56:2080, 1997.

[44] S. P. Weppner, C. Elster and D. Hüber. *Phys. Rev. C*, 57:1378, 1998.

[45] X. G. Huang. *Phys. Rev. C*, 81:034007, 2010.

[46] H. Lehmann. *Nuovo Cim.*, 11:342, 1954.

[47] R. V. Reid. *Annals of Physics*, 50:411, 1968.

[48] B. E. Vonderfecht, C. C. Gearhart, W. H. Dickhoff, A. Polls and A. Ramos. *Phys. Lett. B*, 253:1, 1991.

[49] B. E. Vonderfecht. PhD thesis, Washington University, 1991.

[50] H. Müther and W. H. Dickhoff. *Phys. Rev. C*, 72:054313, 2005.

[51] S. Reddy, M. Prakash and J. M. Lattimer. *Phys. Lett. B*, 58:41, 1997.

[52] A. Sedrakian. *Prog. Part. Nucl. Phys.*, 58:168, 2007.

[53] B. Link, R. I. Epstein and K. A. Van Riper. *Nature*, 359:616, 1992.

[54] N. Andersson, K. Glampedakis, W. C. G. Ho and C. M. Espinoza. *Phys. Rev. Lett.*, 109:241103, 2012.

[55] N. Chamel. *Phys. Rev. Lett.*, 110:011101, 2013.

[56] J. M. Dong, U. Lombardo, H. F. Zhang and W. Zuo. arXiv:1502.05673, 2015.

[57] J. Wambach, T. L. Ainsworth and D. Pines. *Nucl. Phys. A*, 555:128, 1993.

[58] A. B. Migdal. *Theory of Finite Fermi Systems*. Interscience, New York, 1967.

[59] D. Pines. *The many-body problem: a lecture note and reprint volume*. Frontiers in physics. W. A. Benjamin, 1962.

[60] R. Haussmann, W. Rantner, S. Cerrito and W. Zwerger. *Phys. Rev. A*, 75:023610, 2007.

[61] H. J. Schulze, A. Polls and A. Ramos. *Phys. Rev. C*, 63:044310, 2001.

[62] J. M. Dong, U. Lombardo and W. Zuo. *Phys. Rev. C*, 87:062801, 2013.

[63] A. A. Abrikosov, L. P. Gorkov and I. Y. Dzyaloshinskii. *Quantum Field Theoretical Methods in Statistical Physics*. Pergamon Press, 2nd edition, 1965.

[64] T. Frick. PhD thesis, University of Tübingen, 2004.

[65] A. Rios. PhD thesis, University of Barcelona, 2007.

[66] V. Somà and P. Bożek. *Phys. Rev. C*, 78:054003, 2008.

[67] J. Thouless. *Ann. Phys.*, 10:553, 1960.

[68] L. P. Kadanoff and P. C. Martin. *Phys. Rev.*, 124:670, 1961.

[69] T. Alm, B. Friman, G. Röpke and H. Schulz. *Nucl. Phys. A*, 551:45, 1993.

[70] P. Bożek. *Nucl. Phys. A*, 657:187, 1999.

[71] T. Frick and H. Müther. *Phys. Rev. C*, 68:034310, 2003.

[72] P. Bożek. *Phys. Rev. C*, 62:054316, 2000.

[73] A. Schwenk, B. Friman and G. E. Brown. *Nucl. Phys. A*, 713:191, 2003.

[74] A. Schwenk and B. Friman. *Phys. Rev. Lett.*, 92:082501, 2004.

[75] A. Sedrakian, J. W. Clark and M. G. Alford. volume 8. World Scientific, 2006.

[76] C. Shen, U. Lombardo and P. Schuck. *Phys. Rev. C*, 71:054301, 2005.

[77] W. H. Dickhoff and H. Müther. *Nucl. Phys. A*, 473:394, 1987.

[78] S. Babu and G. E. Brown. *Annals of Physics*, 78:1, 1973.

[79] B. L. Friman and A. K. Dhar. *Physics Letters B*, 85:1, 1979.

[80] W. H. Dickhoff, A. Faessler, J. Meyer-Ter-Vehn and H. Müther. *Nuclear Physics A*, 368:445, 1981.

[81] S. S. Pankratov, M. Baldo and E. E. Saperstein. *Phys. Rev. C*, 91:015802, 2015.

[82] A. Sedrakian. *Phys. Rev. C*, 68:065805, 2003.

[83] W. C. G. Ho, K. G. Elshamouty, C. O. Heinke and A. Y. Potekhin. *Phys. Rev. C*, 91:015806, 2015.

[84] J. Margueron, H. Sagawa and K. Hagino. *Phys. Rev. C*, 77:054309, 2008.

[85] F. V. De Blasio, M. Hjorth-Jensen, Ø. Elgarøy, L. Engvik, G. Lazzari, M. Baldo and H. J. Schulze. *Phys. Rev. C*, 56:2332, 1997.

[86] S. Maurizio, J. W. Holt and P. Finelli. *Phys. Rev. C*, 90:044003, 2014.

[87] J. P. Jeukenne, A. Lejeune and C. Mahaux. *Phys. Rev. C*, 10:1391, 1974.

[88] J. P. Jeukenne, A. Lejeune and C. Mahaux. *Phys. Rev. C*, 16:80, 1977.

[89] E. Bauge, J.P. Delaroche and M. Girod. *Nuclear Physics A*, 654:829c, 1999.

[90] M. I. Haftel and F. Tabakin. *Phys. Rev. C*, 3:921, 1971.

[91] J. M. Mueller, R. J. Charity, R. Shane, L. G. Sobotka, S. J. Waldecker, W. H. Dickhoff, A. S. Crowell, J. H. Esterline, B. Fallin, C. R. Howell, C. Westerfeldt, M. Youngs, B. J. Crowe and R. S. Pedroni. *Phys. Rev. C*, 83:064605, 2011.

[92] A. Carbone, A. Rios and A. Polls. *Phys. Rev. C*, 90:054322, 2014.

[93] N. W. Ashcroft and N. D. Mermin. *Solid State Physics*. Brooks Cole, 1976.

[94] J. M. Luttinger. *Phys. Rev.*, 121:942, 1961.